## Title

The Designs, Syntheses and Medical Applications of Mesoporous Silica Nanoparticle Based Drug Delivery Systems



## Author

Li, Zongxi

## Publication Date

2012

Peer reviewed|Thesis/dissertation

UNIVERSITY OF CALIFORNIA

Los Angeles

# The Designs, Syntheses and Medical Applications of Mesoporous Silica Nanoparticle Based Drug Delivery Systems

A dissertation submitted in partial satisfaction of the

requirements for the degree Doctor of Philosophy

in Chemistry

by

Zongxi Li

2012

ABSTRACT OF THE DISSERTATION

The Designs, Syntheses and Medical Applications of Mesoporous Silica Nanoparticle Based Drug Delivery Systems

by

Zongxi Li

Doctor of Philosophy in Chemistry

University of California, Los Angeles, 2012

Professor Jeffrey I. Zink, Chair

The work covered in this thesis focuses on the development of mesoporous silica nanoparticle-based platforms for the controlled delivery of therapeutic agents. The first part of the thesis discusses the physical chemical properties of mesoporous silica nanoparticles, including the studies on their uptake and release capacities and the physical states of the encapsulated cargo molecules using spectroscopic methods. The second part of the thesis describes the organic functionalizations of the mesoporous silica nanoparticles with novel cyclodextrin-based nanogate systems, achieving pH and redox responsive controlled release mechanisms, as well as cargo size selectivity for the release

from a dual-loaded system. In the third part of this thesis, several examples of the biomedical applications of the mesoporous silica nanoparticle based drug delivery systems are shown. This includes the *in vitro* delivery of small interference RNA to shutdown endogenous and exogenous gene expressions in cells using the polyethyleneimine coated nanoparticles, the *in vivo* delivery of anti-cancer therapeutic to achieve tumor suppression effects on mice models, and the *in vivo* delivery of anti-microbial therapeutic to achieve animal protection from anthrax lethal toxins. A combination of all these areas of research demonstrate the advancement of the mesoporous silica nanoparticle based drug delivery system towards utilization within living organisms, and realization of medicine on the nanoscale.

The dissertation of Zongxi Li is approved.

Paula L. Diaconescu

Fuyuhiko Tamanoi

Jeffrey I. Zink, Committee Chair

University of California, Los Angeles

2012

This dissertation is dedicated to Yue Zong and Mingxiang Li, my dearest parents

## TABLE OF CONTENTS

## LIST OF FIGURES AND TABLES

## ACKNOWLEDGEMENTS

There are so many people I owe my thanks to in completing my doctoral degree. First I would like to acknowledge my advisor, Professor Jeffrey I. Zink. He is an amazing scientist who does significant research and at the same time, is a great mentor who cares about the learning and future of his students. I want to thank him for allowing me the opportunity to do research in his group, for teaching me the skills in experimental designs and following through, publishing findings and proposing new ideas, leading a group as well as being part of a collaborative team, and most importantly, for allowing me to follow my own dreams. I also would like to thank Professor Paula L. Diaconescu and Professor Fuyuhiko Tamanoi to serve on my dissertation committee.

Next I would like to thank my dear colleagues and friends in the Zink group, with whom I shared five years of happy memories. I would like to thank Dr. Sarah Angelos and Dr. Monty Liong for training me upon joining the group and with whom I worked closely on a number of research projects. I was lucky to be able to learn from these two level-headed and hardworking people. Their dedication and work ethics have great impact on me in my graduate school years, and will keep guiding me into my future. I would like to thank Dr. Daniel Ferris, Dr. Bryana Henderson, Juyao Dong, Angela Hwang, Min Xue and Sui Yang for their hard work on our collaborative projects. Our research would not have been possible without the generous contributions made by these people. I would like to thank Dr. Sanaz Kabehie, Dr. Yaroslav Klichko, Dr. Rachel Stephenson, Dr. Phil Rutkowski, Dr. Ryan Hoekstra, Dr. Marcelle Dibrell, Dr. Yuen Lau and Dr. Travis Pecorelli who graduated before me and set up great examples for us

younger generations. The amount of work they put in as senior members to address group businesses and maintain group equipments was essential in keeping our research lab running. I also would like to thank Courtney Thomas, Tania Guardado, Melissa Russel, Derrick Tarn, Matt Kiesz and Janie Chen for being good friends over the years, who will take over the tasks of maintaining our group and continue to put out exciting works after I graduate.

I would like to acknowledge our generous collaborators outside the Zink group, without whom none of my work would have been possible. First I would like to thank Dr. Fraser Stoddart and his postdocs Dr. Yanli Zhao and Dr. Cheng Wang for providing their expertise on organic synthesis. Dr. Stoddart's work ethics had a great impact on me. I also learned a lot of paper writing and presentation skills from working with his group. Then I would like to acknowledge Dr. Fuyuhiko Tamonoi, his postdoc Dr. Jie Lu and graduate student Christopher Hom for their kind collaboration on a number of projects. Dr. Tamanoi has always been very supportive for me throughout my graduate school years. Dr. Jie Lu, as our main go-to person whenever we need to do cell studies, has helped us put out many high quality work. I respect him for being a highly efficient and hardworking scientist and have the pleasure of working with him. Another group we had extensive collaboration with is Dr. Andre Nel's research group in the UCLA medical school. I learned a lot about biological research and nanotoxicology from working with him and his group members Dr. Huan Meng, Dr. Tian Xia and Dr. Zhaoxia Ji. As a member of the Center of Environmental Implications of Nanotechnology (CEIN) directed by Dr. Nel, I also got the chance to interact with scientists in the microbiology field, in

educational outreach programs and many helpful administrative staff members. Yet another group of people I would like to thank is Dr. Ken Bradley and his postdoc Dr. Eugene Gillespie for their work on the anthrax drug delivery project. We would not be able to make all the progress without their willingness to work with the dangerous anthrax toxins. I also want to acknowledge Dr. Jean-Olivier Durand and his graduate student Jeff Likoko for working on the loading capacity project during Jeff's stay in our laboaratory.

Last but not least, I would like to thank my family and friends outside of school. My parents are the biggest driving force throughout my life. I am so lucky to be their daughter and to receive their endless love and support. I hope by getting this degree I make them proud and show that I will carry on their optimism and kindness into all things in my life. I would like to thank Jie Luo, Yinjin Pan, JuanJuan Du, Xiaoming Zhu Min Xue and Yuewei Sheng for being my close friends and for being there for me through good things and bad. We arrived in the United States at the same time. They are the brothers and sisters I never had. These people are the most precious treasures in my life, and my endless source of energy. I cannot say enough thank you to them.

## VITA

| | |
|---|---|
| 1988 | Born, Beijing, China |
| 2007 | B.S. Chemistry<br>Peking University<br>Beijing, China |
| 2007-2009, 2012 | Teaching Assistant<br>Department of Chemistry and Biochemistry<br>University of California, Los Angeles<br>Los Angeles, California |
| 2009 | UCLA Distinguished Teaching Award |
| 2009 | Baur Award for Excellence in Research |
| 2009-2012 | Research Assistant<br>Zink Research Group |

## PUBLICATIONS

**(*Co-First Author)**

1. Cheng Wang*****, **Zongxi Li***, Justin W. Gaines, Yan-Li Zhao, Dennis Cao, O. Altan Bozdemir, Michael W. Ambrogio, Marco Frasconi, Youssry Y. Botros, Jeffrey I. Zink, J. Fraser Stoddart. "Controlled Release of Two Cargos in Succession from Mesoporous Silica Nanoparticles." *Angew. Chem., Int. Ed.*, **2012**, DOI: 10.1002/anie.201107960.

2. **Zongxi Li**, Jonathan C. Barnes, Aleksandr Bosoy, J. Fraser Stoddart, Jeffrey I. Zink. "Mesoporous Silica Nanoparticles in Biomedical Applications." *Chem. Soc. Rev.* **2012**, *41*, 2590-2605.

3. **Zongxi Li**, Jeff Nyalosaso Likoko, Angela A. Hwang, Daniel P. Ferris, Sui Yang, Gaelle Derrien, Clarence Charnay, Jean-Olivier Durand, Jeffrey I. Zink. "Uptake and Release Capacities of Nanovalve-gated Stimulated Release Systems based on Mesoporous Silica Nanoparticles." *J. Phys. Chem. C* **2011**, *115*, 19496-19506.

4. Jie Lu, **Zongxi Li**, Jeffrey I. Zink, Fuyuhiko Tamanoi. "In vivo tumor suppression efficacy of mesoporous silica nanoparticles-based drug delivery system: enhanced efficacy by folate modification." *Nanomedicine* **2011**, *8*(2), 212-220.

5. Huan Meng, Sui Yang, **Zongxi Li**, Tian Xia, Justin Chen, Zhaoxia Ji, Haiyuan Zhang, Xiang Wang, Sijie Lin, Connie Huang, Z. Hong Zhou, Jeffrey I. Zink, Andre E. Nel. "Aspect Ratio Determines the Quantity of Mesoporous Silica Nanoparticle Uptake by a Small GTPase-Dependent Macropinocytosis Mechanism." *ACS Nano*. **2011**, *5*(6), 4434-4447.

6. Yan-Li Zhao, **Zongxi Li**, Sanaz Kabehie, Youssry Y. Botros, J. Fraser Stoddart, Jeffrey I. Zink. "pH Operated Nanopistons on the Surfaces of Mesoporous Silica Nanoparticles." *J. Am. Chem. Soc*. **2010**, *132*, 13016-13025.

7. Jie Lu, Monty Liong, **Zongxi Li**, Jeffrey I. Zink, Fuyuhiko Tamanoi. "Biocompatibility, Biodistribution, and Drug-Delivery Efficiency of Mesoporous Silica Nanoparticles for Cancer Therapy in Animals." *Small* **2010**, *6*(16), 1794-1805.

8. Huan Meng, Monty Liong, Tian Xia, **Zongxi Li**, Zhaoxia Ji, Jeffrey I. Zink, Andre E. Nel. "Engineered Design of Mesoporous Silica Nanoparticles to Deliver Doxorubicin and P-Glycoprotein siRNA to Overcome Drug Resistance in a Cancer Cell Line." *ACS Nano* **2010**, *4*(8), 4539-4550.

9. Christopher Hom, Jie Lu, Monty Liong, Hanzhi Luo, **Zongxi Li**, Jeffrey I. Zink, Fuyuhiko Tamanoi. "Mesoporous silica Nanoparticles Facilitate Delivery of siRNA to Shutdown Signaling Pathways in Mammalian Cells." *Small* **2010**, *6*(11), 1185-1190.

10. Travis A. Pecorelli, Marcelle M. Dibrell, **Zongxi Li**, Courtney R. Thomas, Jeffrey I. Zink. "Multifunctional Inorganic Nanoparticles for imaging, targeting, and drug delivery." *Proceedings of SPIE* **2010**, *7576*, 74760K0-12.

## PATENTS

1. EGA: A Small Molecule Inhibitor of Microbial Virulence Factors That Require Acidic Endosomes. PCT Int. Appl. *In Preparation*.

2. Tuning Aspect Ratio of Mesoporous Silica Nanoparticle Determines The Quantity of Cell Uptake. PCT Int. Appl. 61/466,581.

3. Mesoporous Silica Nanoparticle Based siRNA/Drug Delivery System. PCT Int. Appl. 61/363,945.

# Chapter 1

## Mesoporous Silica Nanoparticles (MSNs) as Drug Delivery Vehicles

## 1.1. Introduction

### 1.1.1. The "Magic Bullet" in Theranostic Nanomedicine and Mechanized Mesoporous Silica Nanoparticles (MSNs)

Various types of multifunctional theranostic nanomedicines for cancer chemotherapies, which can travel within the blood stream and deliver a concentrated drug payload to the diseased tissues (Figure 1.1) have been developed in the past few decades.[1,2] Several advantages in using these nanometer-sized delivery platforms include the ability to control the drug release rate and therefore fine tune the pharmacokinetics of the drug, the accumulation of these nanomedicines at the pathological region of interest without damaging normal cells in surrounding healthy tissues, and the possibility of achieving controlled-release of the drug upon activation by one or more possible stimuli, such as light, temperature, pH, and so on. Additionally, an ideal nanomedicine would possess the means - either extrinsically, or intrinsically - to track the progress of the accumulation in the tumor tissue of, as well as the release of, the therapeutic agent through the use of radionuclides[3] or contrast agents.[4] If these criteria are met, then the idea of a personalized "concurrent therapy" can be realized through the use of various types of multifunctional theranostic nanomedicines.

Mechanized mesoporous silica nanoparticles (i.e. MSNs functionalized with nanomachines) offer a wide range of functionalities and are highly robust and modular as they can be chemically modified to fit the circumstances of almost any desired setting. Possessing a high surface area-to-volume ratio allows for increased surface functionalization, while still maintaining great porosity, which allows the inorganic

platform to house appreciable amounts of cargo without destabilization of the silica framework.[5-9] This introduction will focus on the synthesis and properties of MSNs, as well as on the supramolecular chemistry behind the controlled release of cargo using nanoscale switches with the ultimate goal of demonstrating the utility of this platform in theranostic nanomedicine.

### 1.1.2. Synthesis and Properties of the Mesoporous Silica Nanoparticles

A base-catalyzed sol-gel process has been employed to produce silica nanoparticles with sizes suitable for biomedical applications. The sol-gel process utilizes the organosilane precursors (TMOS, TEOS, etc.), which, by means of hydrolysis and condensation reactions,

$$\text{Hydrolysis:} \quad OH^- + Si(OR)_4 \rightarrow Si(OR)_3OH + RO^-$$

$$\text{Condensation:} \quad SiO^- + Si(OH)_4 \rightarrow Si\text{-}O\text{-}Si + OH^-$$

lead to the formation of a new phase (sol). The small colloidal particles within the sol then condense into the gel phase.[10] For example, the Stöber process has been widely applied for the preparation of monodispersed silica nanoparticles between 50 and 2000 nm size, using the ammonia-catalyzed hydrolysis of tetraethylorthosilicate (TEOS) in a water-alcohol solution.[11]

Using micelles formed by a cationic surfactant as the templating agent, the silicate source can be directed to condense around the micellar template into ordered silica structures. Mesoporous silica materials were first synthesized by two different research groups for catalytic applications.[12, 13] Although the materials made by the original procedures are mainly mesoporous silica sheets with disorganized morphologies, there

have been continuous efforts in making these materials into smaller size and homogeneous morphology in order to increase their biocompatibiliy. Grun et al. first prepared submicromter-scaled MCM-41 particles using a modified Stober synthesis.[14] Later on, MCM-41 silica particles of 100 nm were obtained by using a dilute surfactant solution.[15] Mesoporous silica nanoparticles below 50 nm have also been obtained using a double surfactant system or dialysis process.[16] Metal or metal oxide nanocrystals around 10 nm in diameter can be incorporated into the MSN during the particle synthesis to provide additional functionalities. This type of procedure has been used to embed gold, silver and iron oxide (including doped iron oxide) into the MSNs.[6, 17] The metal/metal oxide cores can provide a variety of additional functionalities to the MSNs, such as antimicrobial activity through dissolved metal ions, plasmonic effects or magnetic properties including MRI capabilities.

In a typical synthesis of the 100 nm MCM-41 type mesoporous silica nanoparticles, the silica source, tetraethylorthosilicate (TEOS), is added into a heated basic (pH 11) aqueous solution of the templating surfactant, cetyltrimethylammonium bromide (CTAB). 100 nm diameter nanoparticles are formed through base-catalyzed sol-gel condensation around the hexagonally packed micelle structures.[6, 9] After aging, the resulting nanoparticles are refluxed in acidic alcohol to decrease the interactions between the surfactant and the silica frame, and remove the templating agent from the mesopores. X-ray diffraction and electron microscopy confirm that the hexagonal arrays of pores remain intact after the surfactant removal process. The solvent extracted particles are

spherical in shape, roughly 100 nm in diameter, and contain 2D-hexagonally arranged pores 2-3 nm in diameter.

The ease of introducing various organic functional groups, either through covalent bonding or electrostatic interactions, provides high level of versatility and many mechanized features to the mesoporous silica materials. The covalent attachment of functional groups usually involves introducing organic structures in the form of silanes, which can be attached using co-condensation or post-synthetic grafting methods.[18] The co-condensation method allows the hydrolysis of the functional silanes while the particles are forming, therefore the guest molecules are incorporated into the resulting silica frameworks. In contrast, post-synthetic grafting introduces the functional groups mainly to the exposed silica surface after the MSNs are formed, which can be performed either before or after the surfactant removal.[18] Besides covalent attachment, functional moieties can also be introduced to the MSNs through electrostatic interactions. This usually makes use of the negative charges from the free $SiO^-$ groups on the particle's surface. For example, cationic polymers (such as polyethyleneimine) can be electrostatically adsorbed onto the silica nanoparticles to provide nucleic acid binding properties.[19-21]

Another crucial property that makes mesoporous silica materials promising for drug delivery applications is their ability to encapsulate different types of cargo molecules within their pore channels. This is important because the encapsulation may protect many therapeutic agents from enzymatic degradation. The particles are usually loaded by soaking them in a drug solution. The drug molecules are incorporated by the particles through adsorption. The interactions between the cargo molecules and the

particle usually include hydrogen bonding and electrostatic interactions. The uptake capacities of the MSNs are correlated with the specific surface areas of the materials.[22] The loading and release efficiencies of the particles are also affected by the electrostatic interactions between the cargo molecules and the silica surface.[23-25] When combined with the functional modifications on the MSNs, the payloads are only allowed to be released in a controllable fashion at the targeted diseased tissues, with no premature release during their circulation within the bloodstream. This can significantly reduce the adverse side effects of the drug and increases the overall therapeutic efficacy.

### 1.1.3. How to achieve controllable cargo delivery

Based on the above described properties of mesoporous silica nanoparticles, the obvious way to use them as a delivery system is to load the drugs by adsorbing them onto the particles and then release them by dissolution inside the target media. In this case, there is no control over the pore openings and the resulting system performs sustained release. The rate of the release would highly depend on the solubility of the drug in the surrounding solvent. If the drug molecules are highly water soluble, they would be released as soon as the particles are suspended in an aqueous biological media, which would not be advantageous over a solution dose of the same drug. If the drug molecules are hydrophobic, the particles do provide some control over the release of the drug. Once hydrophobic drugs are loaded into the MSNs, the release of the drugs in an aqueous media is minimal. Only when the particles come into contact with a hydrophobic environment, for instance upon addition of a surfactant, the hydrophobic cargo is then released. *In vitro* studies have shown that the interactions between particles and the cell

membrane phospholipids during the particle endocytosis can cause the release of the encapsulated hydrophobic drugs.[26]

MSNs-based controlled release systems have been developed by applying mechanical controls over the pore openings. First, polymers that are either adsorbed or covalently bonded to the surface of the MSNs have served as a mechanized controlled release system.[27] Under their "closed" condition, the polymer chains tightly wrap around the particle surface, each blocking multiple pore openings. Then the polymers are induced by certain stimuli to undergo swelling or coiling so that the pore openings are re-exposed and cargo is released through the unblocked pores. A second method to achieve controllable release is to form chemical bonds directly over the pore openings that can later be cleaved upon stimulation.[28] A third way to mechanically block the pores is to attach bulky groups such as Au or CdS nanocrystals over the pore openings.[5] These bulky groups serve as gatekeepers for the encapsulated cargo. Removal of the bulky blocking groups via chemical methods initiates cargo release.

When bulky groups are assembled by non-covalent interactions, they become nanomachines, such as "nanovalves" and "snap-top" machines.[6] These nanomachines usually contain a static stalk covalently attached to the particles surface and a bulky cyclic moving component which encircles the stalk via non-covalent interactions. The nanomachines are designed to undergo large amplitude motions upon stimuli. The blocking and un-blocking of the pore openings is achieved by such motions. It is worth noting that in such designs the attachment of nanomachines may not cover all the pore openings on the particle surface perfectly. Particles such as MCM-41 have pore channels

that are not inter-connected, which allows the washing procedures to remove cargo from any pores that have faulty machines. Yet another way to achieve controlled release is by derivatizing the pore interiors of the MSNs. One such example is the "nanoimpeller" machine that takes advantage of the rapid cis-trans isomerization of the azobenzene groups upon light activation.[29] Figure 1.2 is a schematic illustration of the above described pore controlling mechanisms.

These mechanized controlled release systems could have a variety of internal and external power supplies. The first type of stimulus is provided by chemicals. Systems can be designed to be responsive to external chemical additions, or to the internal chemical changes within organs and cells, such as pH change and cytoplasmic enzymes.[5, 6, 30] Since the addition of chemical stimulants is not always feasible for *in vitro* and *in vivo* experiments, the biological applications of chemical responsive controlled release systems are limited by the types of chemical changes existing in the cells and organisms. The second type of stimuli is electrical, using redox reactions to trigger the release. This can be accomplished by external means, like directly applying electrodes, or by internal means, e.g. using the internal reducing conditions inside cells.[31, 32] Light has been applied as another external power supply for controlled release systems.[28, 29] The *in vivo* application of light stimuli is limited by the tissue penetration ability of the stimulating light. External heating can be used to trigger the release of the mechanized MSNs. Heat can also be made an internal stimulus when it is generated by magnetic nanocrystals in an oscillating magnetic field.[17] All of the above-described power supplies trigger the operation of the mechanized MSNs either by causing structural changes to polymer

coatings, or by causing molecular or supramolecular motions of the "gatekeeper" groups, which in turns lead to the un-blocking of the pore openings.

### 1.1.4. Cellular Uptake and Biocompatibility of MSNs

Before MSNs can be effectively applied as drug delivery systems, their cellular uptake and cytotoxicity properties have to be investigated. The cellular uptake of the MSNs can be studied by attaching fluorescent dye molecules to the nanoparticles, enabling the visualization of the MSNs by fluorescence and confocol microscopy. Fluorescent dye molecules, such as fluorescein isothiocyanate (FITC) and Rhodamine B isothiocyanate (RITC), can be bonded to the surface of the particles by co-condensation.[26] Cellular uptake of the MSNs and their good biocompatibility was confirmed with both healthy and cancer cell lines.[26, 33, 34] No cytotoxicity is observed up to 100 μg/mL for non-modified 100 nm MSNs,[17, 21, 34-36] which is well above the effective particle concentrations required for most therapeutic treatments. Several research groups have demonstrated that cell uptake and cellular toxicity of the MSNs depend on the particle's size, shape, surface charge and functional groups.[5, 9] Cell staining experiments in conjunction with the fluorescently labeled MSNs allow the study of the cellular uptake mechanisms and the particle location inside the cells (Figure 1.3). Small MSNs (< 200-300 nm) are normally taken up by cells via endocytotic pathways, which could end up taking various routes such as the clathrin-dependent, caveolin-dependent, receptor-mediated or the clathrin and caveolin independent mechanism, depending on the shape, size and surface functionalization of the nanoparticles. The endocytic mechanisms for MSNs have been summarized in recent reviews.[5, 9] The endocytotic process consists of

the particle interacting with the cell surface, cell membrane invagination and pinching off. The nanoparticles upon uptake are located inside the endocytic vescicles which fuse with the early endosomes and then to the sorting endosomes. The remaining fraction of the early endosomes then matures into late endosomes before fusing with the acidic lysosomes. The MSNs end up inside these acidic (pH~4.5) organelles in cells. It has also been shown that nanoparticles with surface groups that can be protonated facilitate the "proton sponge effect", which leads to the endosomal escape of the uptaken particles.[19] This enables the membrane impermeable cargoes such as hydrophilic drugs, DNA and siRNA molecules to be released from the membrane-bounded endosomes and travel to their effective sites.

In the following chapters, my latest advancements in developing the mesoporous silica nanoparticle based drug delivery systems will be presented in three major aspects. Chapters 2 & 3 focus on the physical chemical properties of the mesoporous silica materials that make them suitable for drug loading purposes. Chapters 4 & 5 describe the organic functionalization of mesoporous silica nanoparticles with two novel nanomachines to achieve highly controllable stimuli-responsive cargo release from these particles. Finally, three different biomedical applications of the mesoporous silica nanoparticle based drug delivery systems will be shown in Chapters 6, 7 and 8, demonstrating their *in vitro* siRNA delivery, *in vivo* tumor shrinking and anti-anthrax therapeutic efficacies.

## 1.2. Figures and Tables

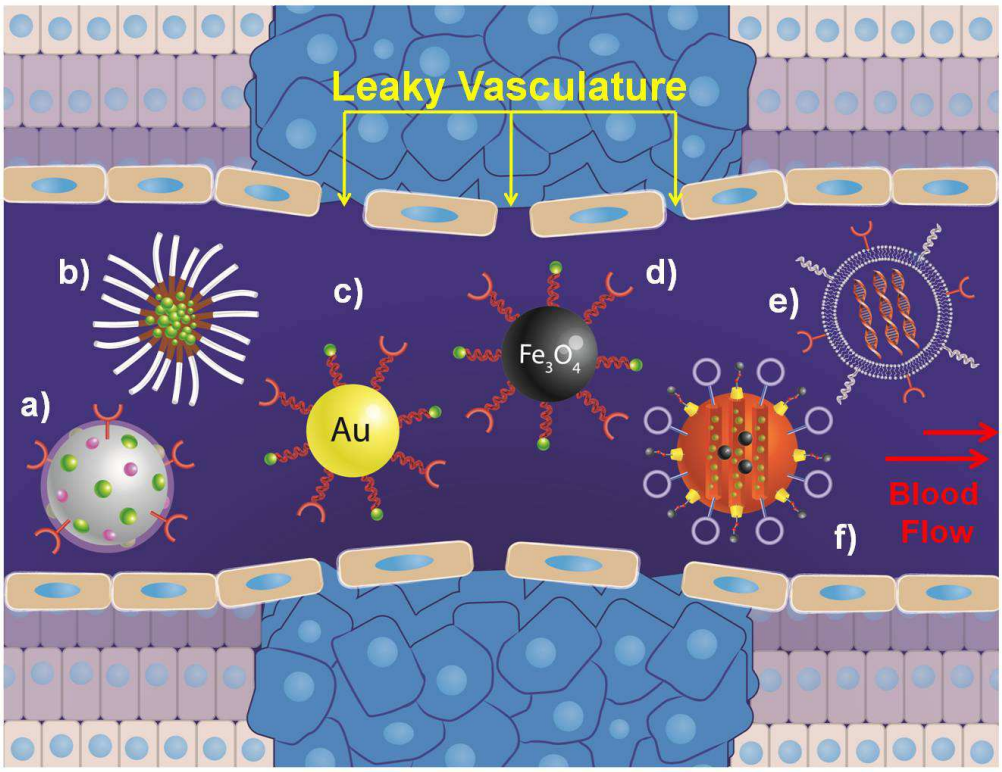


**Figure 1.1.** Various types of theranostic nanomedicines are depicted in "attack mode" over a site of tumor growth in this cartoon representation. Conjugated targeting ligands are shown as circles or semi-circles. Cargo, conjugated or housed internally, is shown as green spheres. Purple spheres represent imbedded contrast agents. A multifunctional **a)** polymeric nanogel, **b)** polymeric micelle, **c)** gold nanoparticle, **d)** iron oxide nanoparticle, **e)** siRNA ensconced in a liposome delivery vector, and **f)** a stimuli-responsive capped mesoporous silica nanoparticle are shown.

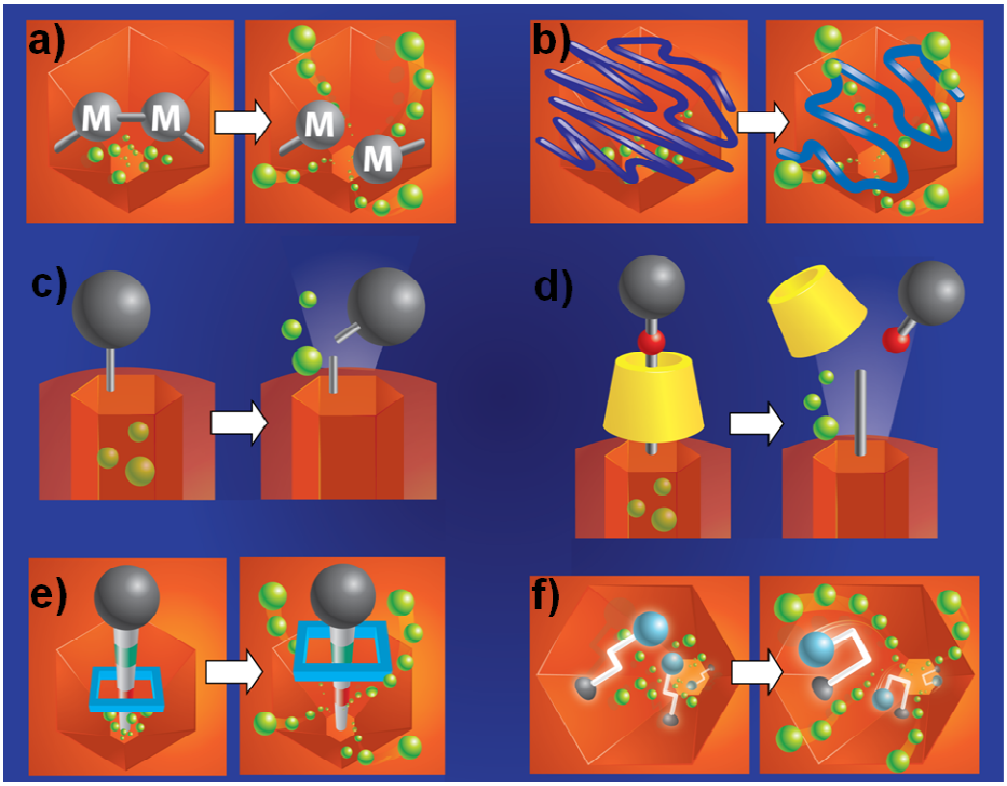


**Figure 1.2.** Pore opening control motifs designed for mesoporous silica nanoparticle-based stimuli responsive delivery systems, showing pore blocking and unblocking by a) the formation and breaking of covalent bonds between molecules (e.g. coumarin) attached within the pore channels; b) the shrinking and swelling of polymer chains coated on the particle surface; c) attachment and removal of bulky groups (e.g. Au, CdS nanocrystals) over the pore openings; d) threading and dethreading of a cyclic torus molecule in this "snap-top" design consisting of a [2]rotaxane with a bulky stopper; e) shuttling of a cyclic molecule between two recognizing sites along a molecular stalk towards and away from the pore opening in a supramolecular "nanovalve" design; f) azobenzene molecules tethered within the pore channels hinder the diffusion of the encapsulated cargo molecules, whereas the wagging motion resulting from the cis-trans photoisomerization of the azobenzene propels the cargo molecules out of the mesopores.

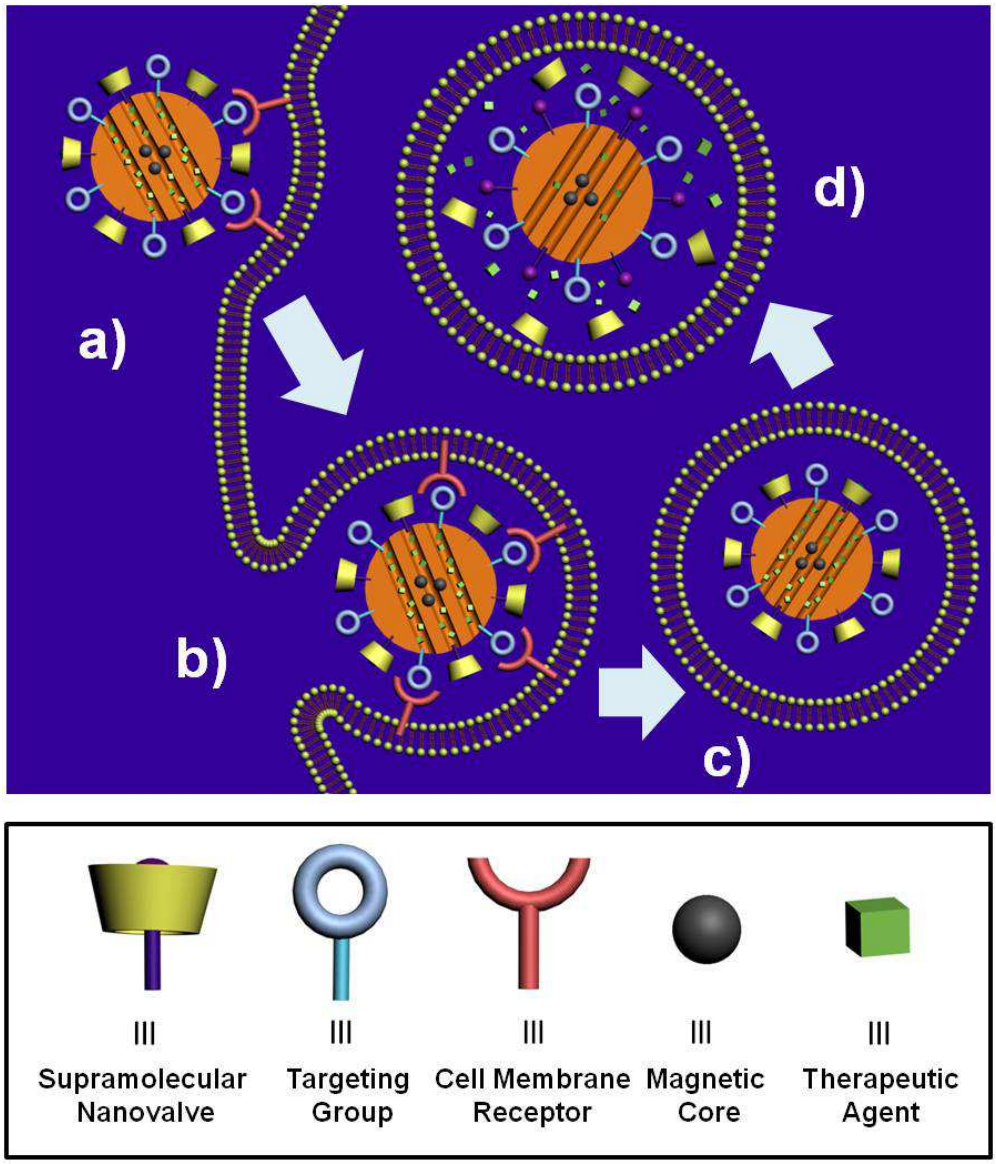


**Figure 1.3.** Illustration of the receptor-mediated endocytosis of multi-functional mesoporous silica nanoparticles and intracellular drug release. a) Cell surface receptors recognizing the targeting groups on the MSN surface; b) cell surface invagination and pinching during particle intake; c) internalized MSN within an early endosome; d) intracellular drug release from the MSNs.

## 1.3. References


1. K. Strebhardt and A. Ullrich, *Nat. Rev. Cancer*, **2008**, *8*, 473-480.
2. D. Peer, J. M. Karp, S. Hong, O. C. Farokhzad, R. Margalit and R. Langer, *Nat. Nanotechnol*., **2007**, *2*, 751-760.
3. W. T. Phillips, B. A. Goins and A. Bao, *Wiley Interdiscip. Rev. Nanomed. Nanobiotechnol.*, **2009**, *1*, 69-83.
4. M. de Smet, E. Heijman, S. Langereis, N. M. Hijnen and H. Grull, *J. Controlled Release*, **2011**, *150*, 102-110.
5. J. L. Vivero-Escoto, I. I. Slowing, B. G. Trewyn and V. S.-Y. Lin, *Small*, **2010**, *6*, 1952-1967.
6. K. K. Coti, M. E. Belowich, M. Liong, M. W. Ambrogio, Y. A. Lau, H. A. Khatib, J. I. Zink, N. M. Khashab and J. F. Stoddart, *Nanoscale*, **2009**, *1*, 16-39.
7. M. Liong, J. Lu, M. Kovochich, T. Xia, S. G. Ruehm, A. E. Nel, F. Tamanoi and J. I. Zink, *Acs Nano*, **2008**, *2*, 889-896.
8. M. Manzano and M. Vallet-Regi, *J. Mater. Chem.*, **2010**, *20*, 5593-5604.
9. S. H. Wu, Y. Hung and C. Y. Mou, *Chem. Commun.*, **2011**, doi:10.1039/c1031cc11760b.
10. C. J. Brinker and G. W. Scherer, Academic Press, Inc., San Diego, **1990**.
11. W. Stober, A. Fink And E. Bohn, *J. Colloid Interf. Sci.*, **1968**, *26*, 62-69.
12. T. Yanagisawa, T. Shimizu, K. Kuroda And C. Kato, *B. Chem. Soc. Jpn*, **1990**, *63*, 988-992.

13. C. T. Kresge, M. E. Leonowicz, W. J. Roth, J. C. Vartuli And J. S. Beck, *Nature*, **1992**, *359*, 710-712.

14. M. Grun, I. Lauer and K. K. Unger, *Adv. Mater.*, **1997**, *9*, 254-257.

15. Q. Cai, Z. S. Luo, W. Q. Pang, Y. W. Fan, X. H. Chen and F. Z. Cui, *Chem. Mater.*, **2001**, *13*, 258-263.

16. K. Suzuki, K. Ikari and H. Imai, *J. Am. Chem. Soc.*, **2004**, *126*, 462-463.

17. C. R. Thomas, D. P. Ferris, J. H. Lee, E. Choi, M. H. Cho, E. S. Kim, J. F. Stoddart, J. S. Shin, J. Cheon and J. I. Zink, *J. Am. Chem. Soc.*, **2010**, *132*, 10623-10625.

18. M. H. Lim and A. Stein, *Chem. Mater.*, **1999**, *11*, 3285-3295.

19. T. Xia, M. Kovochich, M. Liong, H. Meng, S. Kabehie, S. George, J. I. Zink and A. E. Nel, *Acs Nano*, **2009**, *3*, 3273-3286.

20. C. Hom, J. Lu, M. Liong, H. Luo, Z. Li, J. I. Zink and F. Tamanoi, *Small*, **2010**, *6*, 1185-1190.

21. H. Meng, M. Liong, T. Xia, Z. Li, Z. Ji, J. I. Zink and A. E. Nel, *Acs Nano*, **2010**, *4*, 4539-4550.

22. J. Andersson, J. Rosenholm, S. Areva and M. Linden, *Chem. Mater.*, **2004**, *16*, 4160-4167.

23. H. Meng, M. Xue, T. Xia, Y. Zhao, F. Tamanoi, J. F. Stoddart, J. I. Zink and A. E. Nel, *J. Am. Chem. Soc.*, **2010**, *132*, 12690-12697.

24. B. Munoz, A. Ramila, J. Perez-Pariente, I. Diaz and M. Vallet-Regi, *Chem. Mater.*, **2003**, *15*, 500-503.

25. T. H. Chung, S. H. Wu, M. Yao, C. W. Lu, Y. S. Lin, Y. Hung, C. Y. Mou, Y. C. Chen and D. M. Huang, *Biomaterials*, **2007**, *28*, 2959-2966.

26. J. Lu, M. Liong, J. I. Zink and F. Tamanoi, *Small*, **2007**, *3*, 1341-1346.

27. Q. Fu, G. V.-R. Rao, L. K. Ista, Y. Wu, B. P. Andrzejewski, L. A. Sklar, T. L. Ward and G. P. Lopez, *Adv. Mater.*, **2003**, *15*, 1262-1266.

28. N. K. Mal, M. Fujiwara, Y. Tanaka, T. Taguchi and M. Matsukata, *Chem. Mater.*, **2003**, *15*, 3385-3394.

29. S. Angelos, E. Choi, F. Vogtle, L. De Cola and J. I. Zink, *J. Phys. Chem. C*, **2007**, *111*, 6589-6592.

30. M. Manzano, M. Colilla and M. Vallet-Regi, *Expert Opin. Drug Del.*, **2009**, *6*, 1383-1400.

31. M. W. Ambrogio, T. A. Pecorelli, K. Patel, N. M. Khashab, A. Trabolsi, H. A. Khatib, Y. Y. Botros, J. I. Zink and J. F. Stoddarrt, *Org. Lett.*, **2010**, *12*, 3304-3307.

32. R. Mortera, J. Vivero-Escoto, I. Slowing, E. Garrone, B. Onida and V. Lin, *Chem. Commun.*, **2009**, 3219-3221.

33. D. R. Radu, C. Y. Lai, K. Jeftinija, E. W. Rowe, S. Jeftinija and V. S.-Y Lin, *J. Am. Chem. Soc.*, **2004**, *126*, 13216-13217.

34. S. P. Hudson, R. F. Padera, R. Langer and D. S. Kohane, *Biomaterials*, **2008**, *29*, 4045-4055.

35. J. Lu, E. Choi, F. Tamanoi and J. I. Zink, *Small*, **2008**, *4*, 421-426.

36. J. Lu, M. Liong, Z. Li, J. I. Zink and F. Tamanoi, *Small*, **2010**, *6*, 1794-1805.

Part I

# Physical Chemical Properties of Mesoporous Silica Nanoparticles

# Chapter 2

## Measurement of Uptake and Release Capacities of Mesoporous Silica Nanoparticles Enabled by Nanovalve Gates

## 2.1. Abstract

The uptake and release capacities of mesoporous silica particles are measured on nanovalve-gated stimulated release systems, using a water soluble biological stain, Hoechst 33342, as the cargo model. Five different types of mesoporous silica nanoparticles: 2D-hexagonal MCM-41, swollen pore MCM-41, rod-like MCM-41, hollow mesoporous nanoparticles and radial mesoporous nanoparticles are studied and compared. Solid silica nanoparticles are used as the control. Because of the presence of the nanovalves, the loaded and capped particles can be washed thoroughly without losing the content of the mesopores. The quantity of Hoechst 33342 molecules trapped within the nanoparticles and released upon opening the nanovalves are systematically studied for the first time. The loading conditions are optimized by varying the Hoechst concentration in the loading solutions. Surprisingly, increasing the Hoechst concentration in the loading solution does not always result in a larger amount of Hoechst being trapped and released. Among the five types of mesoporous silica nanoparticles, the radial mesoporous nanoparticles and the swollen pore MCM-41 particles show the highest and lowest release capacity, respectively. The uptake capacities are correlated with the specific surface area of the materials rather than their internal volume. The uptake and release behaviors are also affected by charge and spatial factors.

## 2.2. Introduction

Mesoporous silica nanoparticles with therapeutic agents integrated into their pore channels that can be released in a controllable fashion have received increasing attention as a drug delivery platform.[1-6] The effective pore capacity of the these mesoporous silica

nanoparticles is of great importance because it determines the maximum amount of therapeutic agents that can be kept within the nanoparticles and released at the targeted diseased tissues autonomously or upon external stimuli. Pore volumes of the materials can be measured by gas adsorption/desorption isotherms, but the pore capacity for large molecules released for biological studies in aqueous environment requires the measurement of the actual number of molecules loaded into and released out of the pores. However, without a gate keeper for the pore opening, the pore capacity of mesoporous silica materials cannot be accurately measured, since the outer surface of these loaded nanoparticles cannot be cleaned extensively before the release study. It has been difficult to quantitatively distinguish the amount of cargo actually loaded inside the pore channels from that absorbed on the outer surface of the materials.

The uptake and release properties of mesoporous silica materials have been studied using open-pore sustained release systems. Many particle features have been shown to affect the uptake and release properties of mesoporous silica materials, including the particle's shape,[7] specific surface area, pore size,[8-10] pore structure,[11] and surface functional groups.[7,12-17] These studies have been carried out with both hydrophobic and hydrophilic cargo molecules. The loading capacity measured for these open-pore systems involves the amount of cargo molecules loaded inside the mesopores as well as those on the outer surface of the silica materials.

In this study, we show for the first time how the measurement of mesoporous silica effective pore capacity is enabled using a nanovalve gated system. The nanoparticles are loaded with a water-soluble biological stain, Hoechst 33342, and

assembled with an acid-responsive supramolecular nanovalves using a previously described procedure.[18] Due to the presence of the nanovalve gate, the particles can be washed extensively after loading and capping to remove the cargo molecules adsorbed on the particle outer surface. To measure the amount of Hoechst 33342 molecules trapped inside the mesopores, the pH of the media was not only adjusted to open the nanovalve, but also brought below the isoelectric point of the silica for the maximal removal of the content.

Because of the control provided by the gatekeeper nanovalves, the details of the stages of uptake and release of the cargo dye can be differentiated. In a typical measurement, the particles are loaded in an aqueous Hoechst 33342 solution. The amount of Hoechst taken up by the particles (in the internal pores and on the external surface) is calculated from the concentration difference of the solution before and after loading. The "Uptake efficiency" is defined as the total amount of Hoechst taken up by the particles divided by the total dye amount in the original solution (expressed in percent). The amount of Hoechst not uptaken by the particles divided by the total dye amount in the original solution (expressed in percent) is defined as "Left in loading solution" (Figure 2.1a). The above stage is referred to as the uptaking stage.

The next stages determine the fate of the uptaken dye molecules. The loaded particles are capped with α-CD and then washed extensively with water. The total amount of Hoechst removed from the particles during capping and washing is measured from the collected washing solution, and is defined as "Lost in capping and washing" (Figure 2.1b). Then the gatekeeper valves are opened by acidifying the water and the amount of dye

molecules that are released into the solution is measured. The amount of Hoechst released divided by the total uptaken amount (in percent) is defined as the “Release efficiency”. Finally, the amount (in percent) of the dye permanently “Retained” on the particles after release is quantified (Figure 2.1b). These stages account for all of the dye take up by the particles.

The mass of dye measured in the uptake efficiency stage divided by the mass of the particle is defined as the “Uptake capacity” (expressed in wt %). The mass of dye measured in the release efficiency stage divided by the mass of the particle is defined as the “Release capacity” (in wt %). The uptake and release efficiency/capacity values are compared for different loading concentrations. The values for five types of bio-relevant mesoporous silica nanoparticles with different morphologies are measured using the method described above. Solid silica nanoparticles are used as a control. The effects of particle surface charges were also studied. All the uptake and release experiments were carried out in aqueous solutions, providing biologically relevant results.

## 2.3. Results and Discussion

### 2.3.1. Properties of the Silica Nanoparticles

The sizes and morphologies of the six types of silica nanoparticles were investigated by transmission electron microscope (TEM) as shown in Figure 2.2. The solid nanoparticles (SNPs), the 2D-hexagonal MCM-41 (MCM-41s) and the swollen pore MCM-41 (SMCM-41s) are spherical in shape, and have an average particle size of 100 nm. The SNPs have a smooth surface, and no obvious meso-porosity was observed. The MCM-41s exhibit uniformly sized 2D-hexagonally ordered cylindrical pores,

whereas the SMCM-41s have the same pore arrangement as MCM-41s, but bigger pore sizes.

X-ray diffraction patterns of all the samples are shown in Figure 2.3. The position of the main (100) peak was used to calculate the interplanar spacings $d_{100}$ for the materials. The $d_{100}$ values as well as the distances between pore centers a ($a = 2d/3^{1/2}$) are summarized in Table 2.1. As expected, the SNPs do not show a diffraction pattern, due to their lack of porosity. The MCM-41s show a diffraction pattern with a distance between pore centers of 4.7 nm. The SMCM-41s have a much longer distance of around 6.8 nm.

The $N_2$ adsorption-desorption isotherms for the three samples are shown in Figure 2.4, and the BET surface areas and pore volumes values are listed in Table 2.1. Except for the SNPs, all samples exhibit a pronounced step on their isotherm for relative pressure 0.2-0.7, due to the capillary condensation of nitrogen inside the primary mesopores. The condensation step on the isotherms is steep for MCM-41s and SMCM-41s, indicating a narrow pore size distribution for these three samples. The step for SMCM-41s takes place at a significantly higher relative pressure compared to those for MCM-41s and RMCM-41s, which is representative of a larger pore size.

The specific surface area values of the samples were calculated by the BET method. Primary mesopore sizes of the samples were calculated using three methods: the BJH method; geometrical considerations of an infinite hexagonal array of cylindrical pores (averaged pore diameter (APD) = $1.213d_{100}$ $(\rho V_p/(1+ \rho V_p))^{1/2}$); and the method based on the model of simple cylindrical pores using the BET surface area and primary

mesopore volume ($D_p = 4V_p/S_{BET}$). The specific surface area and pore size values for the three samples are summarized in Table 2.1.

### 2.3.2. Optimization of the Loading Conditions & Distribution of the Cargo Molecules

To optimize the loading conditions, the MCM-41 particles were loaded in five different concentrations of Hoechst 33342 solution, 1 mM, 10 mM, 20 mM, 30 mM and 40 mM. Loading was achieved by soaking 50 mg of the PhAMTES-modified MCM-41 particles in 1 mL of the Hoechst 33342 solution for 3 days at room temperature. The theoretical maximum uptake capacity is governed by the total amount of Hoechst molecules in the loading solution. The experimental uptake capacity was obtained as the difference between the amounts of Hoechst in the supernatant before and after soaking. The nanovalves on the Hoechst 33342-loaded samples were closed by capping with α-CD. The closed particles were washed extensively to remove the adsorbed dye molecules on the exterior surface. Finally the Hoechst-loaded, α-CD-capped, MCM-41 particles were suspended in an acidic solution (pH=1), and the amounts of Hoechst released from the samples were measured by UV-vis spectrophotometer.

The uptake and release capacity are defined respectively as the ratio (expressed in weight percent) of the weight of the Hoechst taken up or released by the particles to the total weight of the tested sample (Experimental Section 4.5.6). The percent uptake and release efficiency are defined respectively as the percentage of Hoechst taken up or released by the particles in the total Hoechst amount in the loading solution. The theoretical maximum uptake capacity is determined, and the experimental uptake and

release capacities for the MCM-41 samples loaded in five different loading concentrations are plotted in Figure 2.6. At 10 mM, the uptake of Hoechst has already reached its saturation amount of 10 wt% of the particles. No excess amount of dye could be taken up when the concentration of the solution in which the particles were loaded was increased beyond 10 mM.

On the other hand, the release capacity increased from 1.4 wt% at 1 mM to 5.4 wt% at 10 mM, but decreased as the loading concentration became higher. This surprising decrease at high concentrations is attributed to the interference with capping when the concentration of Hoechst in the solution is very high. The hydrophobic moieties on the Hoechst molecules compete with the PhAMTES groups on the particle surface to be encircled by the α-CD caps. At the loading concentration of 10 mM, the amount of Hoechst left in the bulk solution after uptake is negligible compared to the excess amount of α-CD added for capping, indicating that capping at 10 mM was unaffected. However, the surplus of Hoechst in the 40 mM loading solution was significant high enough to bind to most of the added α-CD, so there was not enough α-CD to cap the nanovalves. Thus a large amount of the loaded Hoechst molecules were washed out of the particles in the 40 mM case before the release experiment. As shown in Figure 2.6, the cargo to particle ratio of 1:7 by weight was the optimal loading condition to maximize the release capacity, at which 50% of the loaded Hoechst molecules can be released at pH 1.

### 2.3.3. The Uptake Capacity and Uptake Efficiency of the Silica Nanoparticles

The uptake capacity and uptake efficiency values for the SNPs, SMCM-41 and MCM-41 types of silica nanoparticles loaded in 1 mM and 10 mM Hoechst 33342

solutions are summarized in Table 2.2. At 1 mM loading concentrations, the SNPs had an uptake efficiency as low as 3%, due to their lack of porosity to accommodate the cargo molecules. The other samples reached 100 % uptake efficiency, meaning that all the Hoechst dye molecules in the loading solution were taken up by the nanoparticles after three days of loading. This demonstrated that during the loading process, the Hoechst solution does not simply diffuse into the pores of the materials, equilibrating the Hoechst concentration inside the pores and the bulk solution. Instead, the Hoechst molecules have a strong interaction with the inner pore wall surface, and the cargo molecules are concentrated inside the pores. The interaction is from hydrogen bonding and electrostatic attraction between the positively charged Hoechst 33342 molecule and the negatively charged silica surface as will be discussed later.

The uptake efficiency is affected by the spatial limitations of the particles. When loaded in the 10 mM Hoechst solutions, the different samples exhibited quite different uptake efficiencies. The samples did not reach 100% uptake efficiency as in the case of 1 mM loading concentration. This indicates that a saturation point has been reached. The uptake efficiency values have a direct relationship with the specific surface areas rather than with the pore volumes of the samples. For instance, the SMCM-41s have a larger pore volume than the MCM-41s, yet have a much smaller uptake efficiency. The correlation between the uptake efficiency and the surface area of the sample suggests that the loading process is adsorption-controlled due to the interaction between drug and wall.

The density of Hoechst on the particles' surface was calculated from the uptake efficiency. The percent coverage was calculated by comparing the amount of area

covered by all the adsorbed Hoechst molecules with the total surface area of the material using the equation: Percent coverage (%) = (Area of one Hoechst molecule×number of adsorbed Hoechst molecule/surface area of the material)×100%, where the area covered by one Hoechst 33342 molecule is estimated from ChemDraw to be 1.9 $nm^2$, and the number of adsorbed Hoechst molecules is calculated from the uptake capacity. According to the results listed in Table 2.3, the area covered by the cargo molecules is about 20% of the entire particle surface area. This illustrates the very high adsorbing capacity of the particle surface. Similar calculations were carried out for the MCM-41 sample loaded with 1 mM Hoechst, and the SMCM-41 sample loaded with 10 mM Hoechst. The Hoechst percent coverage values are 3% and 20% respectively. The populations of cargo molecules in a section of the primary mesopores are shown in Figure 2.7.

### 2.3.4. The Cargo Release Capacity and Release Efficiency of the Silica Nanoparticles

The Hoechst loaded samples were capped with α-CD and then washed extensively with water until no Hoechst could be detected in the washing supernatant. The washings remove residual Hoechst molecules on the outer surfaces that would otherwise cause overestimation of the release capacity of the Hoechst. The acid-responsive release of Hoechst 33342 from the six types of the nanovalve-capped silica nanoparticles was monitored in aqueous solution using time-resolved luminescence spectroscopy. A laser beam at 448 nm was directed through the solution above the samples to monitor the emission of any released Hoechst 33342 molecules in the solution. The samples were kept in pH 7 water for at least an hour to obtain a baseline before any triggered release.

The flat baselines observed in all cases indicate the leakages from the systems at neutral pH are negligible. It also proves the residual Hoechst from the loading solution was successfully removed by washing. Then the pH of the solution was adjusted to 1 using HCl to open the nanovalve and the emission intensity of Hoechst 33342 increased rapidly upon lowering the pH, indicating the α-CD caps have been removed, followed by the release of the cargo.

The cargo release capacity of the samples was measured by suspending the Hoechst loaded, nanovalve-capped particles in an acidic solution at pH 1 or 3 for 24 hours. The supernatant was then collected and the Hoechst concentration measured by UV-vis absorbance. The release capacity and release efficiency at pH 1 and 3 for the different silica nanoparticles loaded with 1 mM and 10 mM Hoehcst solution are given in Table 2.4. The amounts of Hoechst adsorbed during the loading process and the amount released upon lowering the pH for each of silica nanoparticles are shown in Figure 2.8.

The release capacity is affected by the spatial factors. The samples loaded in the 1 mM Hoechst solution had a release capacity close to their uptake capacity, meaning that most of the loaded Hoechst molecules are eventually released from the particles upon opening the nanovalve. However, the samples loaded in the 10 mM Hoechst solution had a release capacity of about 50% of the their uptake capacity, indicating that only half of the loaded Hoechst molecules can be released. Since the particles have the same surface conditions in both cases, the difference in their release behaviors is explained by the spatial hindrance during the release process. As shown in Figure 2.7, the 10 mM Hoechst loaded particles have a large population of cargo molecules within their primary

mesopores, and the cargo molecules are densely packed. The mobility of the Hoechst molecules is reduced in this rigid environment. It is also likely that several tightly adsorbed Hoechst molecules block the pathway within the pores when they are arranged very close to each other. In such cases, the cargo molecules located deeper the pores would not gain enough mobility to overcome the blockage, and therefore remained inside the pores. This is not a problem for the samples loaded in 1 mM Hoechst solution, since only 3% of the inner pore wall surface was covered by the cargo molecules. The adsorbed Hoechst molecules had much less spatial hindrance when they are being released.

The mobility of the cargo molecules is also affected by their electrostatic interaction with their surroundings, with the less tightly adsorbed molecules being more mobile and vice versa. The release capacity of the MCM-41 samples with three different surface charge conditions are shown in Figure 2.9. The MCM-41(0) and the MCM-41(-) had similar release efficiencies of about 50%. At low pH, the phosphonate groups are mostly protonated, and therefore perform similarly to the OH surface. However, the MCM-41(+) showed nearly 100% release efficiency. The amine surface groups are protonated in acidic conditions, which provide a repulsive force on the positively charged Hoechst molecules and enable them to move efficiently out of the pores. Further evidence of the charge effect is that the release capacities for all the systems are higher at pH 1 than pH 3. Since the nanovalves are completely open in both cases, the higher release capacity at pH 1 can be explained by the greater protonation of the particle surface (the isoelectric point of silica is pH 2) as well as the Hoechst molecules, causing repulsion between them, hence higher mobility of the cargo molecules.

At this point, it is interesting but difficult to compare the uptake capacity results obtained here with those reported in previous publications without control of the pore openings. The impacts of surface area and surface charge on the uptake capacity observed here is consistent with those in previous studies on MCM-41, MCM-48 and SBA type mesoporous silica materials.[28, 30, 33, 62, 64] Previous research on ibuprofen loaded MCM-41 has shown up to 30 wt% uptake capacity.[26, 28] However, ibuprofen is hydrophobic, and its interaction mechanism with the silica surface is different from that of positively charged Hoechst 33342. Ibuprofen has a more spherical shape and its size is about 1/3 that of a Hoechst molecule, enabling them to be more closely packed inside the pores. Because previous studies were performed on uncapped systems, distinguishing the molecules loaded into the pore interiors vs. the ones adsorbed on the exterior surface could not be achieved. In this paper, insights of the uptake and release properties of a nanovalve-gated system are obtained.

## 2.4. Conclusions

The uptake and release capacities were studied for the nanovalve-gated mesoporous silica nanoparticles. The trapped and releasable amounts of a hydrophilic cargo, Hoechst 33342, were measured for five types of mesoporous silica nanoparticles, with the solid silica nanoparticles as the control. The loading conditions were optimized using the MCM-41 sample. As the Hoechst concentration is increased in the loading solution, the uptake capacity of MCM-41 increases and then stabilizes at the point of saturation. On the other hand, the release capacity of MCM-41 at pH 1 first becomes higher with the increasing loading concentration, then decreases as the loading

concentration is increased further. This unexpected trend is explained by the binding between the Hoechst 33342 molecule and the α-CD cap at higher loading concentrations, which results in a lower capping efficiency. The uptake capacities were found to be correlated with the surface areas of the materials. The cargo release efficiency upon opening the nanovalves is affected by both the surface charge of the materials and the population of cargo molecules within the pores. Increasing the cargo populations inside the mesopores results in the spatial hindrance for the trapped molecules, thus a lower percentage of the trapped Hoechst 33342 can be released upon opening the nanovalves.

## 2.5. Experimental

*Materials:* All analytical and reagent grade materials were used as purchased: cetyltrimethylammonium bromide (CTAB) [≥98%, Sigma], tetradecyltrimethylammonium bromide (TTAB) [99%, Sigma-Aldrich], tetraethyl orthosilicate [98%, Aldrich], tetramethoxysilicate (TMOS) [≥99%, Sigma-Aldrich], mesitylene [≥99%, Sigma-Aldrich], dodecylamine (DDA) [≥98%, Aldrich], polyvinylpyrrolidone (PVP-10) [≥98%, Aldrich], 3-(trihydroxysilyl)propyl methylphosphnate, mono sodium salt [42 wt%, solution in water, Aldrich], N-(2-aminoethyl)3-aminopropyl trimethoxysilane [≥95%, Gelest], sodium hydroxide (NaOH) [certified ACS, Fisher], hydrochloric acid (HCl) [certified ACS plus, Fisher], ammonium hydroxide [GR ACS, EMD], methanol [99.9%, Fisher], ethanol [200 proof, Pharmaco-AAPER], toluene [≥99.5%, EMD], ethylene glycol [≥99.5%, Fluka], perfluorooctanoic acid [96%, Aldrich], N-phenylaminomethyl triethoxysilane (PhAMTES) [≥95%, Gelest],

Bisbenzimide H 33342 (Hoechst 33342) [≥98%, Aldrich], α-cyclodextrin (α-CD) [98%, Sigma].

*General Methods:* The transmission electron microscope (TEM) images of the silica nanoparticles were collected on a CM 120 (Philips Electron Optics, Eindhoven, The Netherland) instrument in the California NanoSystem Institute (CNSI). Microfilms for TEM imaging were made by placing a drop of the particle suspension in methanol onto a 200-mesh copper TEM grid (Ted Pella, Inc., Redding, CA) and dried at room temperature. Powder X-ray diffraction (XRD) patterns were collected using an X'Pert Pro diffractometer (Philips) equipped with Cu Kα radiation. $N_2$ adsorption-desorption isotherms were obtained at 77 K on a Quandrchrome Surface Area and Pore Size Analyzer. The stimulated release profiles were obtained using an Acton SpectraPro 2300i CCD and a CUBE 445-40C (Coherent Inc., Santa Clara, CA, USA) laser. UV-vis spectra were collected on a Cary 5000 UV-vis-NIP spectrophotometer. Zeta-potential values for the samples were measured by ZetaSizer Nano (Malvern Instruments Ltd., Worcestershire, UK).

*Preparation of the nanoparticle:* Solid nanoparticles of 80-100 nm diameters (SNPs) were synthesized using a modified Stober method.[44,45] A dilute solution of TEOS (8 mL / 20 mL ethanol) was added drop-wise to a stirring solution of ammonium hydroxide and ethanol (volume ratio 8:100), and left to stir overnight. The particles were collected by centrifugation, washed twice with ethanol, and dried using a rotatory evaporator.

The swollen pore MCM-41 mesoporous silica nanoparticles (SMCM-41s) were prepared using procedures similar to those previously published.[46] CTAB (0.5 g, 1.33 mmol) was dissolved in deionized water (240 mL). Then mesitylene (3 mL, 25 mmol) was added and the solution was heated to 80 °C. 2M NaOH (1.75 mL) water solution was added followed by the addition of TEOS (3 mL, 14 mmol). After 2 hours, the particles were collected by centrifugation and washed by ethanol. The products were solvent extracted in acidic methanol for more than 6 hours. The extracted particles were washed with methanol and dried under vacuum.

To prepare the 2D-hexagonal MCM-41 mesoporous silica nanoparticles (MCM-41s),[48] CTAB (250 mg, 0.67 mmol) was dissolved in deionized $H_2O$ (120 mL) with a 2M NaOH water solution (0.875 mL). The mixture was stirred and heated to 80 °C when TEOS (1.25 mL, 6 mmol) was slowly added into the solution. The TEOS was allowed to hydrolyze for 2 hours and the reaction was cooled down to room temperature. The products were collected by centrifugation and washed by methanol. To remove the templating surfactant molecules from the mesopores, 250 mg of the as-synthesized MCM-41s were suspended in acidic methanol. The mixture was refluxed under nitrogen for 12 hours. The solvent extracted particles were collected by centrifugation, washed by methanol and dried under vacuum.

To prepare the rod-like MCM-41 mesoporous silica nanoparticles (RMCM-41s) with aspect ratio 2.2,[66,67] CTAB (0.6 g, 1.6 mmol) was dissolved in deionized $H_2O$ (288 mL) with 2M NaOH water solution (2.1 mL). The solution was stirred and heated to 80 °C. Then perfluorooctanoic acid (20 mg, 0.05 μmol) was added as a co-templating

agent. After 30 min, TEOS (4 mL, 19 mmol) was slowly added into the solution, and the mixture was stirred for another 2 hours. The products were collected by centrifugation and washed by ethanol. To remove the templating surfactant molecules from the mesopores, the as-synthesized RMCM-41s were suspended in acidic ethanol, and refluxed under nitrogen for 12 hours. The solvent extracted particles were collected by centrifugation, washed by ethanol and dried under vacuum.

The preparation method of the hollow mesoporous nanoparticles (HNPs) has been published in our previous work.[18] To prepare the HNPs, PVP-10 (0.5 g) was dissolved in an ethanol/$H_2O$ mixture (2:8 v/v). In another flask, DDA (1.3 g, 7 mmol) was dissolved in ethanol (5 mL) under strong sonication. The solution was stirred and heated to 30 °C and the DDA solution was added. After 30 min of stirring, TEOS (5 mL, 24 mmol) was slowly added into the solution, and the mixture was stirred for 3 hours. The product were collected by centrifugation and washed by ethanol. To remove the DDA and PVP molecules from the particles, the as-synthesized HNPs were suspended in ethanol and refluxed under nitrogen for 12 hours. The solvent extracted particles were collected by centrifugation, washed by ethanol and dried under vacuum.

In a typical synthesis of the radial mesoporous nanoparticles (RNPs), TTAB (84 mg, 0.25 mmol) was dissolved in the mixture of deionized water and ethylene glycol as co-solvent (volume ratio 3:1). Then TMOS (0.24 mL, 1.56 mmol) was subsequently added to the solution at 60 °C under intensive stirring. The hydrolysis and polycondensation stages were carried out under basic conditions at pH of 12. The colloidal mixture was stirred overnight. Afterwards the resulting white precipitate was

recovered by centrifugation and dried in air at 50 °C. The template was eliminated from the RNPs by calcinating the sample in air at 450 °C for 8 hours at a heating rate of 2 °C·min$^{-1}$.

*Modification of the MCM-41 Outer and Inner Pore Wall Surface with Charged Groups:* The synthetic methods for the OH surface MCM-41s were described above. To modify the outer and inner pore wall surface with negatively charged groups, the solvent extracted MCM-41 (250 mg) were suspended in deionized $H_2O$. Then 3-(trihydroxysilyl)propyl methylphosphonate (120 μL, 0.5 mmol) was added, and the mixture was refluxed under nitrogen for 24 hours. The phosphonate modified MCM-41s were collected by centrifugation, washed with methanol and dried under vacuum.

To modify the outer and inner pore wall surface with positively charged groups, the solvent extracted MCM-41s (250 mg) were suspended in ethanol. Then N-(2-aminoethyl)3-aminopropyl trimethoxysilane (110 μL, 0.5 mmol) was added, and the mixture was refluxed under nitrogen for 24 hours. The amine modified MCM-41s were collected by centrifugation, washed with ethanol and dried under vacuum.

*Construction of the Acid-responsive Nanovalves:* The methods for the assembling the acid-responsive nanovalves have been described in our previous work.[18] Typically, the solvent extracted nanoparticles (100 mg) were suspended in dry toluene (10 mL). Then PhAMTES (30μL, 0.1 mmol) was added into the particle suspension under stirring. The mixture was stirred at room temperature under nitrogen for 24 hours. The product were

collected by centrifugation, washed extensively with methanol, and dried under vacuum. Hoechst 33342 molecules were loaded into the nanoparticles by soaking 50 mg of the PhAMTES-modified nanoparticles in 1 mL aqueous solution of Hoechst 33342 at room temperature for 3 days. Finally, the Hoechst 33342 loaded samples were capped with α-CD (0.1 g, 0.1 mmol) at room temperature for 24 hours. The final products were collected by centrifugation, washed with deionized water until no Hoechst 33342 can be detected in the washing supernatant. The particles were dried under vacuum prior to the stimulated release studies.

*Stimulated Release Studies:* To acquire the release profiles, 3 mg of the Hoechst 33342 loaded nanoparticles were placed in one corner of a glass cuvette. 3 mL of deionized water was carefully added into the cuvette to avoid agitating the particles. The emission spectra of the Hoechst 33342 in the upper solution were collected at 1 second intervals, using a 448 nm laser beam (10 mW) to excite the dye molecules as they were released from the nanoparticles. The baseline was collected at pH 7 for 2 hours. Adjusting the solution to pH 1 with addition of HCl triggered the release of Hoechst 33342. The release profiles were obtained by plotting the fluorescence intensity at 530 nm, which is the emission maximum of Hoechst 33342, as a function of time. The solution was gently stirred in the cuvette throughout all stimulated release experiments.

*Uptake Efficiency and Release Capacity Measurements:* The uptake efficiency of the samples was obtained by measuring the absorbance of Hoechst 33342 left in the loading

solution after soaking for 3 days. The value was then compared with the absorbance before loading to calculate the uptake efficiency. Uptake Efficiency (%) = $((A_{before}-A_{after})/A_{before}) \times 100$ %.

The release capacity of the samples at pH 1 and pH 3 were acquired respectively. 3 mg of the Hoechst 33342 loaded, α-CD capped nanoparticles were suspended in 1 mL of pH 1 and pH 3 solution of HCl respectively for 24 hours. The particles were separated from the solution by centrifugation, and the supernatant was kept for the measurement of released dye concentration by a UV-vis spectrophotometer. The release capacity at a certain pH is defined as the weight percent of Hoechst 33342 can be released from the tested amount of nanoparticle under that pH. Release capacity (wt %) = $(W_{released\ dye} / W_{particle}) \times 100$ %.

## 2.6. Figures and Tables

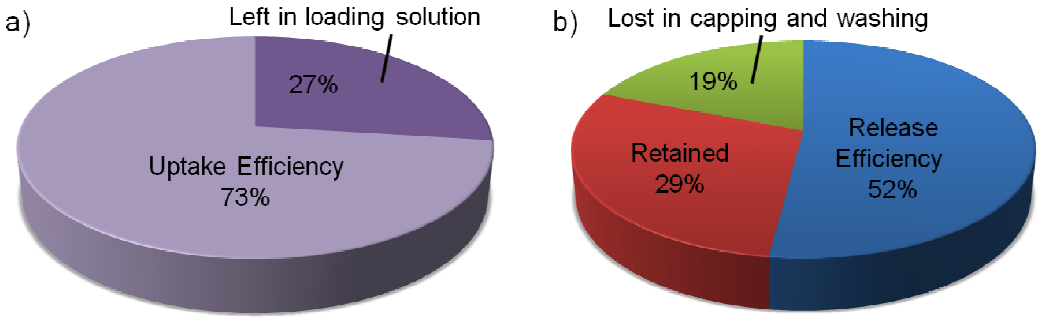


**Figure 2.1**. Pie charts of the distributions of Hoechst 33342 in MCM-41 under uptake, wash and release conditions. a) Results of Hoechst distribution during the loading process. "Uptake Efficiency": the Hoechst molecules taken out of the solution by the particles during the loading process; "Left in loading solution": the Hoechst molecules not taken up by the particles. b) Results of the distribution of the Hoechst molecules taken up by the particles. "Lost in capping and washing": the Hoechst molecules removed from the particles when the α-CD cap was added and the capped particles were washed; "Release efficiency": the Hoechst molecules that were released under pH 1; "Retained": the Hoechst molecules remaining in the particles after the pH 1 release. The numerical values refer to MCM-41 particles loaded in a 10 mM Hoechst solution as discussed in the text.

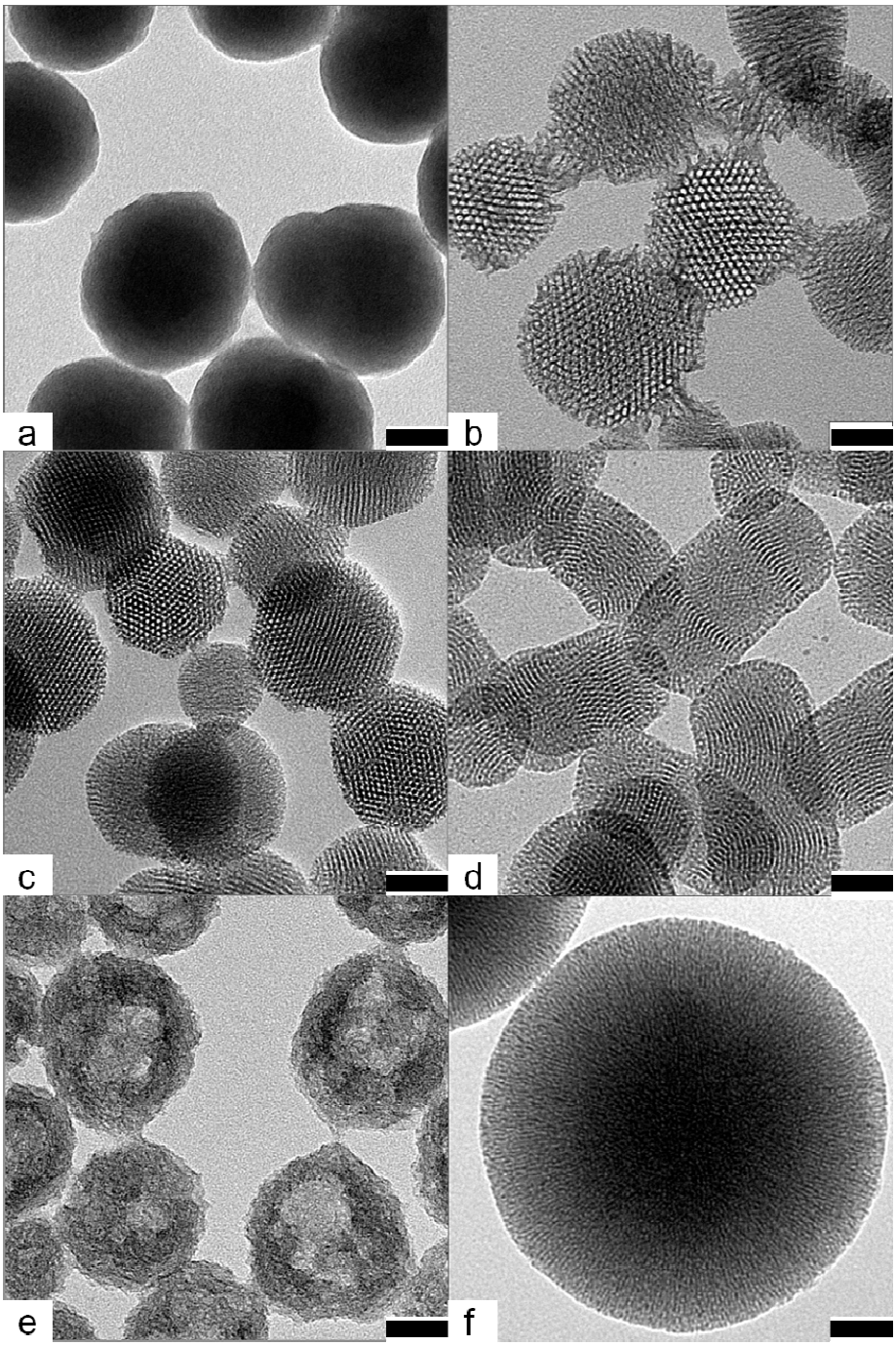


**Figure 2.2.** TEM images of the silica nanoparticles. a) Solid silica nanoparticles (SNPs); b) Swollen pore MCM-41 (SMCM-41s); c) 2D-hexagonal MCM-41 (MCM-41s); d) Rod-like MCM-41 (RMCM-41s); e) Hollow silica nanoparticles (HNPs); f) Radial mesoporous silica nanoparticles (RNPs). Scale bar equals 40 nm.

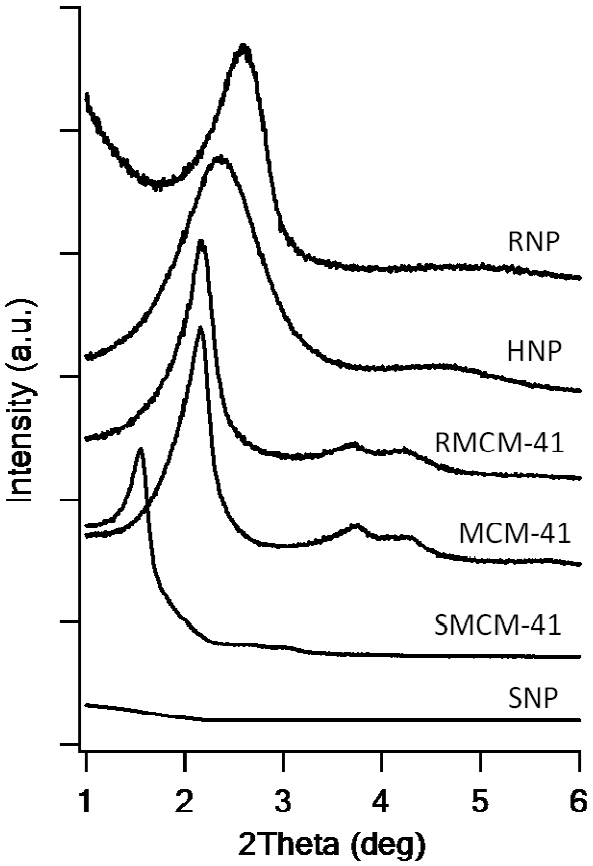


**Figure 2.3.** X-ray diffraction patterns for the six types of silica nanoparticles.

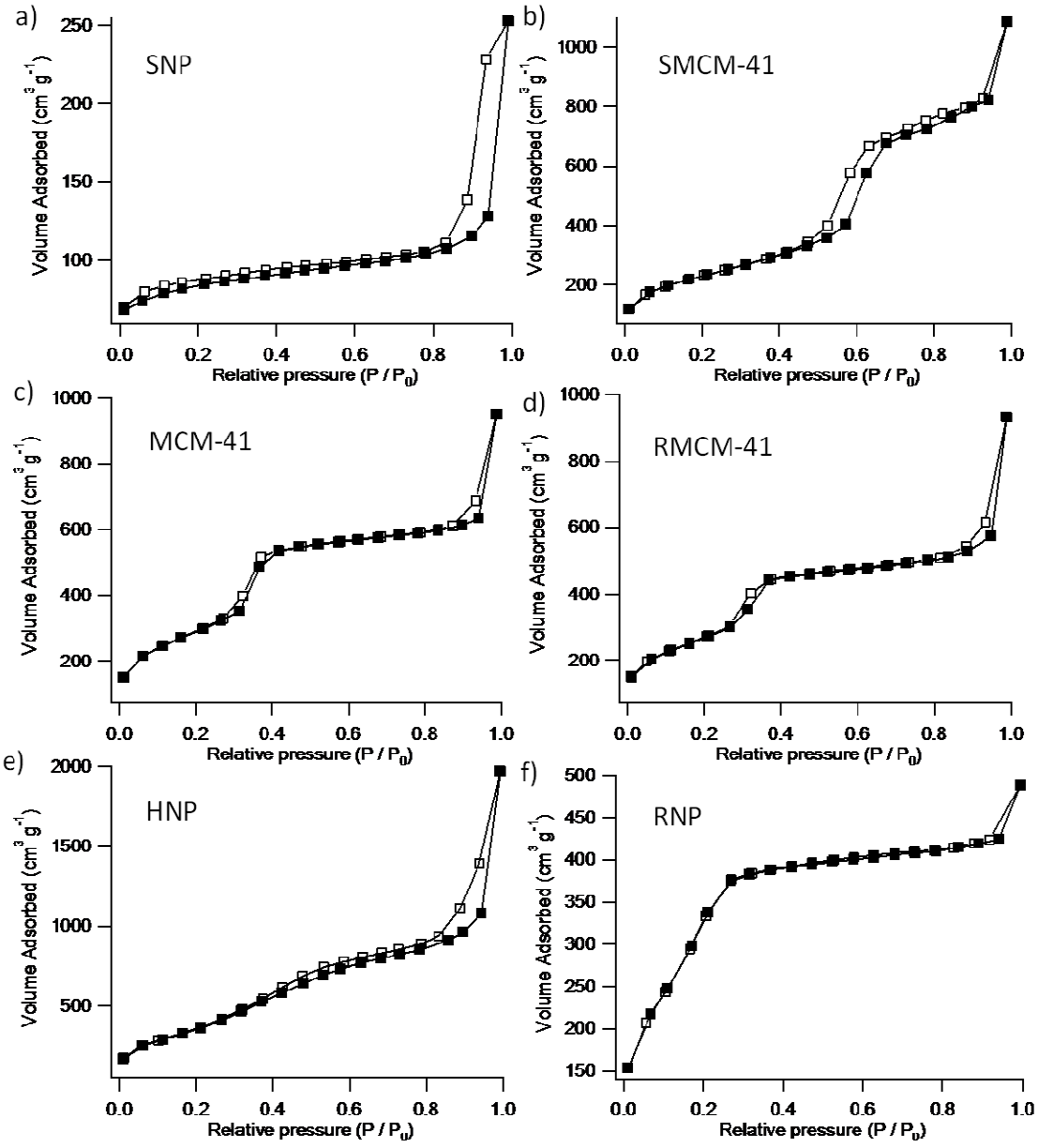


**Figure 2.4.** $N_2$ adsorption-desorption isotherms. a) SNP; b) SMCM-41; c) MCM-41; d) RMCM-41; e) HNP; f) RNP.

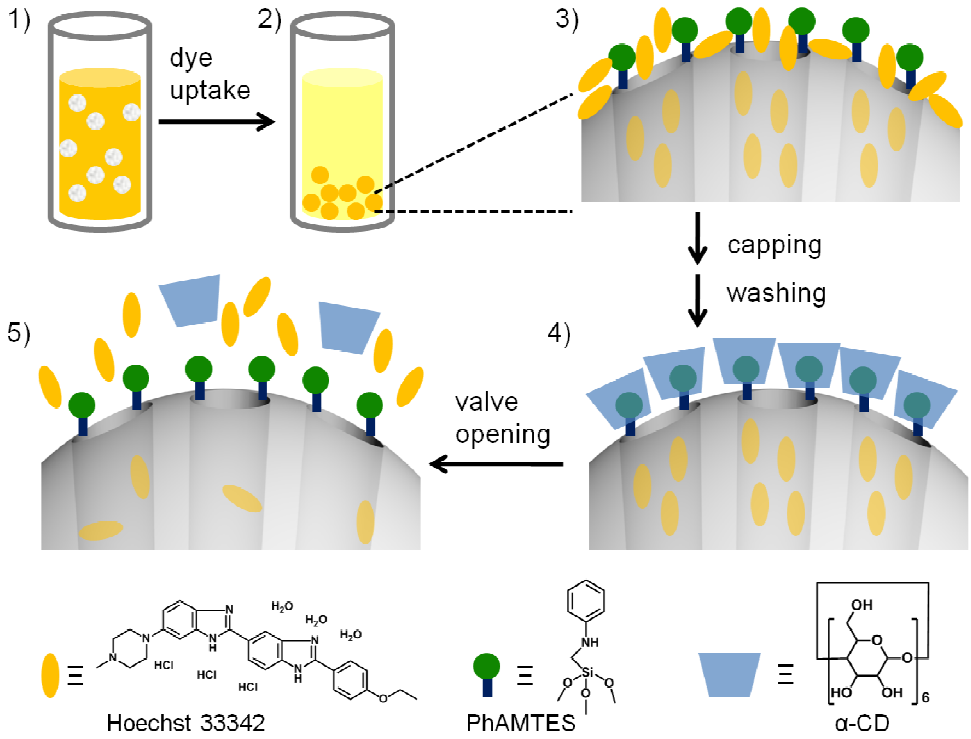


**Figure 2.5.** Uptake, trapping and release of Hoechst 33342 molecules by the nanovalve-gated mesoporous silica nanoparticles. 1) and 2) Uptake of Hoechst 33342 by the nanoparticles (surface and pores); 3) Magnified particle before capping and washing; 4) Dye trapped in pores after capping and washing off molecules from the surface; 5) Cargo molecules released by uncapping the pores.

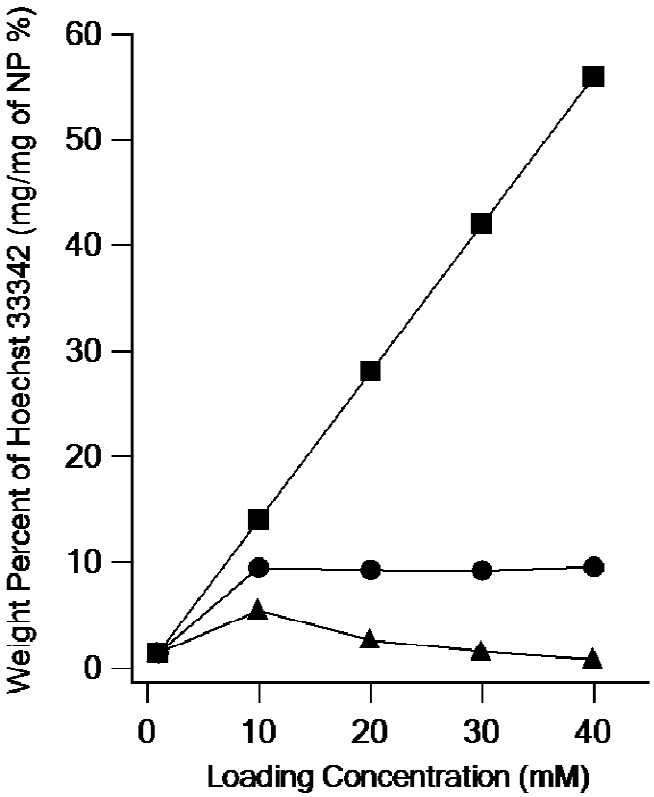


**Figure 2.6.** The uptake capacity and release capacity of MCM-41 at different loading concentrations of Hoechst 33342. ■: Theoretical maximum uptake capacity; ●: Experimental uptake capacity; ▲: Release capacity at pH 1.

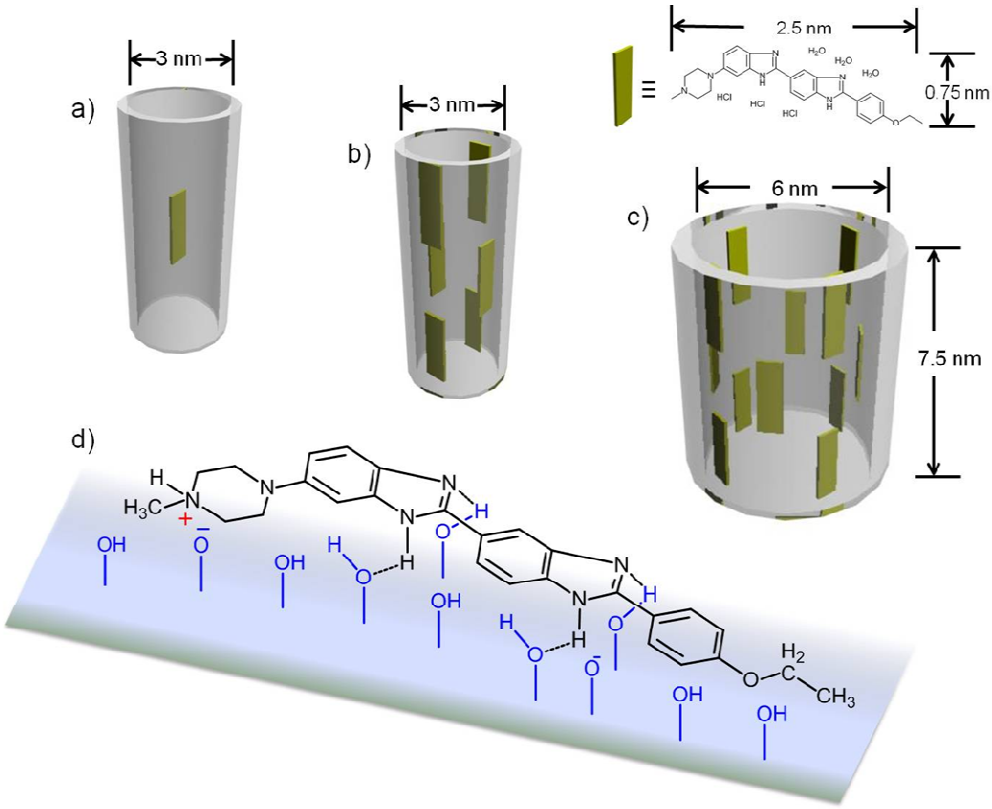


**Figure 2.7.** Population of cargo molecules in a section of the primary mesopore; a) 1 mM Hoechst loaded MCM-41; b) 10 mM Hoechst loaded MCM-41; c) 10 mM Hoechst loaded SMCM-41. d) Sketch of a Hoechst 33342 molecule adsorbed on a silica surface.

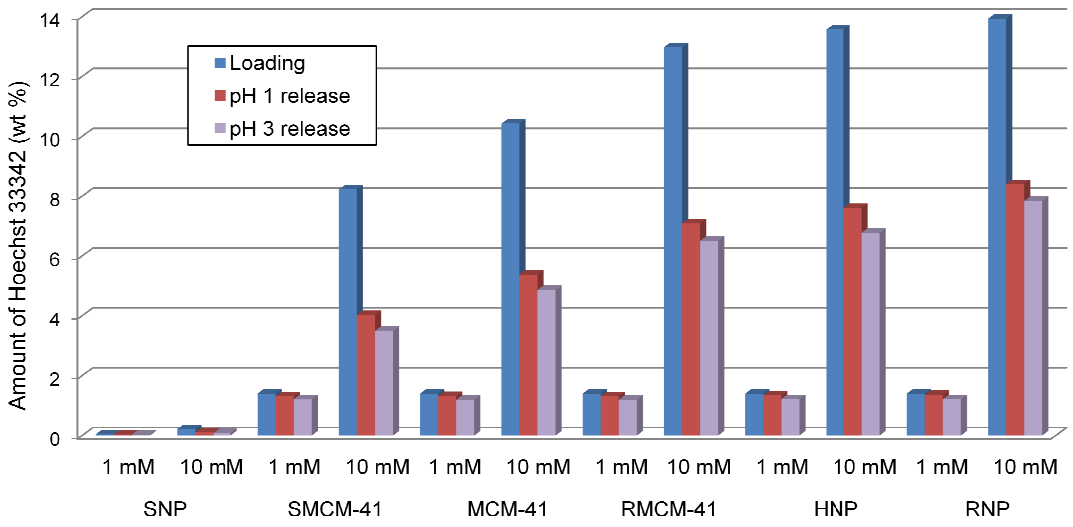


**Figure 2.8.** The amount of Hoechst 33342 loaded in 1 mM and 10 mM solution and the amount released at pH 1 and 3.

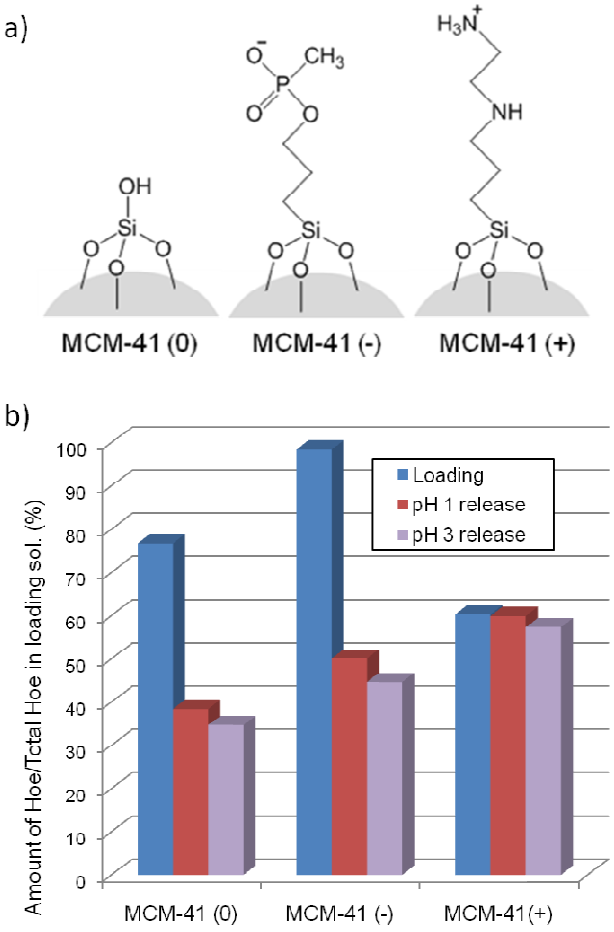


**Figure 2.9.** a) Silica surface groups on MCM-41(0), MCM-41(-) and MCM-41(+); b) Amount of Hoechst loaded and released from MCM-41(0), MCM-41(-) and MCM-41(+).

**Table 2.1.** Properties of the Nanoparticles Calculated from X-ray Diffraction Pattern and $N_2$ Adsorption-Desorption Isotherms.

| | $S_{BET}$ ($m^2$/g) | $V_p$ (mL/g) | 2θ(°) | $d_{100}$ (nm) | a (nm) | $D_{4V/S}$ (nm) | $D_{BJH}$ (nm)[a] | APD (nm) |
|---|---|---|---|---|---|---|---|---|
| SNP | 75 | -- | -- | -- | -- | -- | -- | -- |
| SMCM-41 | 828 | 1.12 | 1.56 | 5.88 | 6.53 | 5.41 | 4.64 | 6.14 |
| MCM-41 | 1023 | 0.83 | 2.16 | 4.09 | 4.72 | 3.25 | 3.39 | 3.99 |
| RMCM-41 | 1064 | 0.77 | 2.15 | 4.11 | 4.74 | 2.88 | 3.38 | 3.95 |
| HNP | 1150 | 1.99 | 2.37 | 3.73 | 4.31 | -- | 3.42, 30[b] | -- |
| RNP | 1257 | 0.62 | 2.60 | 3.39 | 3.92 | 1.98 | 2.19 | 3.13 |

[a] determined from the desorption branch. [b] primary mesopore size and large inner-core macropore size, respectively.

**Table 2.2.** Uptake Efficiency (%) of the Samples at 1 mM and 10 mM Loading Concentration.

| loading Conc. | | SNP | SMCM-41 | MCM-41 | RMCM-41 | HNP | RNP |
|---|---|---|---|---|---|---|---|
| 1 mM | uptake efficiency (%) | 3 | 100 | 100 | 100 | 100 | 100 |
| | uptake capacity (wt %) | 0.04 | 1.40 | 1.40 | 1.40 | 1.40 | 1.40 |
| 10 mM | uptake efficiency (%) | 2 | 59 | 73 | 93 | 97 | 100 |
| | uptake capacity (wt %) | 0.2 | 8.2 | 10.2 | 13.0 | 13.6 | 13.9 |

**Table 2.3**. Zeta Potential and Hoechst 33342 Coverage for MCM-41 with Different Surface Charges Loaded in 10 mM Hoechst 33342 Solution.

| particle | zeta potential (mv) | uptake efficiency (%) | Hoe density (n/100 $nm^2$) | Hoe coverage area ($nm^2$/n) | percent coverage (%) |
|---|---|---|---|---|---|
| MCM-41(-) | -33 | 98 | 12 | 8 | 25 |
| MCM-41(0) | -16 | 73 | 9 | 11 | 20 |
| MCM-41(+) | 31 | 60 | 7 | 14 | 15 |

**Table 2.4**. Release Capacity and Release Efficiency at pH 1 and 3 for the particles loaded with 1 mM and 10 mM Hoechst solution.

| | 1 mM Hoechst | | | | 10 mM Hoechst | | | |
|---|---|---|---|---|---|---|---|---|
| | pH 1 | | pH 3 | | pH 1 | | pH 3 | |
| | release capacity (wt %) | release efficiency (%) | release capacity (wt %) | release efficiency (%) | release capacity (wt %) | release efficiency (%) | release capacity (wt %) | release efficiency (%) |
| SNP | 0.04 | 95 | 0.03 | 78 | 0.1 | 51 | 0.1 | 38 |
| SMCM-41 | 1.31 | 93 | 1.20 | 86 | 4.0 | 49 | 3.5 | 42 |
| MCM-41 | 1.32 | 94 | 1.19 | 85 | 5.4 | 52 | 4.9 | 47 |
| RMCM-41 | 1.31 | 93 | 1.19 | 85 | 7.1 | 55 | 6.5 | 50 |
| HNP | 1.34 | 95 | 1.21 | 87 | 7.6 | 56 | 6.8 | 50 |
| RNP | 1.35 | 97 | 1.21 | 86 | 8.4 | 60 | 7.8 | 56 |

## 2.7. References


1. Zhao, D.; Feng, J.; Huo, Q.; Melosh, N.; Fredrickson, G.H.; Chmelka, B.F.; Stucky, G.D. *Science* **1998**, 279, 548.
2. Kim, J.M.; Kim, S.K.; Ryoo, R. *Chem. Commun.* **1998**, 259.
3. Vivero-Escoto, J.L.; Slowing, I.I.; Trewyn, B.G.; Lin, V.S.-Y. *Small* **2010**, 6, 1952.
4. Vallet-Regi, M.; Balas, F.; Arcos, D. *Angew. Chem. Int. Ed.* **2007**, 46, 7548.
5. Coti, K.K.; Belowich, M.E.; Liong, M.; Ambrogio, M.W.; Lau, Y.A.; Khatib, H.A.; Zink, J.I.; Khashab, N.M.; Stoddart, J.F. *Nanoscale* **2009**, 1, 16.
6. Trewyn, B.G.; Slowing, I.I.; Giri, S.; Chen, H.; Lin, V.S.-Y. *Acc. Chem. Res.* **2007**, 40, 846.
7. Manzano, M.; Aina, V.; Arean, C.O.; Balas, F.; Cauda, V.; Colilla, M.; Delgado, M.R.; Vallet-Regi, M. *Chem. Eng. J.* **2008**, 137, 30.
8. Horcajada, P.; Ramila, A.; Perez-Pariente, J.; Vallet-Regi, M. *Micropor. Mesopor. Mater.* **2004**, 68, 105.
9. Andersson, J.; Rosenholm, J.; Areva, S.; Linden, M. *Chem. Mater.* **2004**, 16, 4160.
10. Kruk, M.; Jaroniec, M.; Sayari, A. *J. Phys. Chem. B* **1997**, *101*, 583.
11. Izquierdo-Barba, I.; Sousa, E.; Doadrio, J.C.; Doadrio, A.L.; Pariente, J.P.; Martinez, A.; Babonneau, F.; Vallet-Regi, M. *J. Sol-Gel Sci. Tech.* **2009**, *50*, 421.
12. Horcajada, P.; Ramila, A.; Gerard, F.; Vallet-Regi, M. *Solid State Sci.* **2006**, *8*, 1243.
13. Munoz, B.; Ramila, A.; Perez-Pariente, J.; Diaz, I.; Vallet-Regi, M. *Chem. Mater.* **2003**, *15*, 500.
14. Nieto, A.; Colilla, M.; Balas, F.; Vallet-Regi, M. *Langmuir* **2010**, 26, 5038.

15. Nieto, A.; Balas, F.; Colilla, M.; Manzano, M.; Vallet-Regi, M *Micropor. Mesopor. Mater*. **2008**, *116*, 4.

16. Chung, T.-H.; Wu, S.-H.; Yao, M.; Lu, C.-W.; Lin, Y.-S.; Hung, Y.; Mou, C.-Y.; Chen, Y.-C.; Huang, D.-M. *Biomaterials* **2007**, 28, 2959.

17. Rosenholm, J.M.; Linden, M. *J. Control. Release* **2008**, *128*, 157.

18. Du, L.; Liao, S.; Khatib, H.A.; Stoddart, J.F.; Zink, J.I. *Journal J. Am. Chem. Soc.* **2009**, *131*, 15136.

19. Zhu, C.-L.; Song, X.-Y.; Zhou, W.-H; Yang, H.-H; Wen, Y.-H.; Wang, X.-R. *J. Mater. Chem.* **2009**, *19*, 7765.

20. Lai, C.Y.; Trewyn, B.G.; Jeftinija, D.M.; Jeftinija, K.; Xu, S.; Jeftinija, S.; Lin, V.S.-Y. *J. Am. Chem. Soc.* **2003**, *125*, 4451.

21. Giri, S.; Trewyn, B.G.; Stellmaker, M.P.; Lin, V.S.-Y. *Angew. Chem. Int. Ed.* **2005**, *44*, 5038.

22. Vivero-Escoto, J.L.; Slowing, I.I.; Wu, C.W.; Lin, V.S.-Y. *J. Am. Chem. Soc.* **2009**, *131*, 3462.

23. Mal, N.K.; Fujiwara, M.; Tanaka, Y. *Nature* **2003**, 421, 350.

24. Yang, Q.; Wang, S.; Fan, P.; Wang, L.; Di, Y.; Lin, K.; Xiao, F.-S. *Chem. Mater*. **2005**, *17*, 5999.

25. Park, C.; Oh, K.; Lee, S.C.; Kim, C. *Angew. Chem. Int. Ed.* **2007**, *46*, 1455.

26. Liu, R.; Zhang, Y.; Feng, P. *J. Am. Chem. Soc.* **2009**, *131*, 15128.

27. Park, C.; Lee, K.; Kim, C. *Angew. Chem. Int. Ed.* **2009**, *48*, 1275.

28. Park, C.; Kim, H.; Kim, S.; Kim, C. *J. Am. Chem. Soc.* **2009**, *131*, 16614.

29. Aznar, E.; Coll, C.; Marcos, M.D.; Martinez-Manez, R.; Sancenon, M.; Soto, J.; Amoros, P.; Cano, J.; Ruiz, E. *Chem.-Euro. J*. **2009**, *15*, 6877.

30. Hernandez, R.; Tseng, H.-R; Wong, J.W.; Stoddart, J.F.; Zink, J.I. *J. Am. Chem. Soc.* **2004**, *126*, 3370.

31. Nguyen, T.D.; Leung, K.C.-F.; Liong, M.; Pentecost, C.D.; Stoddart, J.F.; Zink, J.I. *Org. Lett*. **2006**, *8*, 3363.

32. Angelos, S.; Johansson, E.; Stoddart, J.F.; Zink, J.I. *Adv. Funct. Mater*. **2007**, *17*, 2261.

33. Nguyen, T.D.; Liu, Y.; Saha, S.; Leung, K.C.-F.; Stoddart, J.F.; Zink, J.I. *J. Am. Chem. Soc.* **2007**, *129*, 626.

34. Nguyen, T.D.; Leung, K.C.-F.; Liong, M.; Liu, Y.; Stoddart, J.; Zink, J. *Adv. Funct. Mater*. **2007**, *17*, 2101.

35. Angelos, S.; Yang, Y.-W; Patel, K.; Stoddart, J.F.; Zink, J.I. *Chem. Int. Ed.* **2008**, *47*, 2222.

36. Johansson, E.; Choi, E.; Angelos, S.; Liong, M.; Zink, J.I. *J. Sol-Gel Sci. Tech.* **2008**, *46*, 313.

37. Angelos, S.; Khashab, N.M.; Yang, Y.-W; Trabolsi, A.; Khatib, H.A.; Stoddart, J.F.; Zink, J.I. *J. Am. Chem. Soc.* **2009**, *131*, 12912.

38. Ferris, D.P.; Zhao, Y.L.; Khashab, N.M.; Khatib, H.A.; Stoddart, J.F.; Zink, J.I. *J. Am. Chem. Soc.* **2009**, *131*, 1686.

39. Khashab, N.M.; Trabolsi, A.; Lau, Y.A.; Ambrogio, M.W.; Friedman, D.C.; Khatib, H.A.; Zink, J.I.; Stoddart, J.F. *J. Org. Chem*. **2009**, 1669.

40. Ambrogio, M.W.; Pecorelli, T.A.; Patel, K.; Khashab, N.M.; Trabolsi, A.; Khatib, H.A.; Botros, Y.Y.; Zink, J.I.; Stoddart, J.F. *Org. Lett.* **2010**, *12*, 3304.

41. Meng, H.; Xue, M.; Xia, T.; Zhao, Y.; Tamanoi, F.; Stoddart, J.F.; Zink, J.I.; Nel, A. *J. Am. Chem. Soc.* **2010**, *132*, 12690.

42. Aznar, E.; Marcos, M.D.; Martinez-Manez, R.; Sancenon, F.; Soto, J.; Amoros, P.; Guillem, C. *J. Am. Chem. Soc.* **2009**, *131*, 6833.

43. Qu, F.; Zhu, G.; Lin, H.; Zhang, W.; Sun, J.; Li, S.; Qiu, S. *J. Solid State Chem*. **2006**, *179*, 2027.

44. Rossi, L.M.; Shi, L.; Quina, F.H.; Rosenzweig, Z. *Langmuir* **2005**, 21, 4277.

45. Lin, Y.-S.; Haynes, C.L. *J. Am. Chem. Soc.* **2010**, *132*, 4834.

46. Slowing, I.I.; Trewyn, B.G.; Lin, V.S.-Y. *J. Am. Chem. Soc.* **2007**, *129*, 8845.

47. Mellaerts, R.; Jammaer, J.A.; Van Speybroeck, M.; Chen, H.; Van Humbeeck, J.; Augustijns, P.; Van den Mooter, G.; Martens, J.A. *Langmuir* **2008**, 24, 8651.

48. Lu, J.; Liong, M.; Li, Z.; Zink, J.I.; Tamanoi, F. *Small* **2010**, 6, 1794.

49. Lu, F.; Wu, S.-H.; Hung, Y.; Mou, C.-Y. *Small* **2009**, 5, 1408.

50. Rejman, J.; Oberle, V.; Zuhorn, I.S.; Hoekstra, D. *Biochem. J.* **2004**, *377*, 159.

51. Trewyn, B.G.; Nieweg, J.A.; Zhao, Y.; Lin, V.S.-Y. *Chem. Eng. J.* **2008**, *137*, 23.

52. Sun, W.; Fang, N.; Trewyn, B.G.; Tsunoda, M.; Slowing, I.I.; Lin, V.S.-Y.; Yeung, E. *Anal. Bioanal. Chem.* **2008**, *391*, 2119.

53. Huang, X.L.; Teng, X.; Chen, D.; Tang, F.Q.; He, J.Q. *Biomaterials* **2010**, *31*, 438.

54. Slowing, I.I.; Trewyn, B.G.; Lin, V.S.-Y. *J. Am. Chem. Soc.* **2006**, *128*, 14792.

55. Klichko, Y.; Liong, M.; Choi, E.; Angelos, S.; Nel, A.E.; Stoddart, J.F.; Tamanoi, F.; Zink, J.I. *J. Am. Ceram. Soc.* **2009**, *92*, S2.

56. Liong, M.; Lu, J.; Kovochich, M.; Xia, T.; Ruehm, S.G.; Nel, A.E.; Tamanoi, F.; Zink, J.I. *Acs Nano* **2008**, *2*, 889.

57. Kresge, C.T.; Leonowicz, M.E.; Roth, W.J.; Vartuli, J.C.; Beck, J.S. *Nature* **1992**, *359*, 710.

58. Han, Y.J.; Stucky, G.D.; Butler, A. *J. Am. Chem. Soc.* **1999**, *121*, 9897.

59. Slowing, I.I.; Vivero-Escoto, J.L.; Wu, C.-W; Lin, V.S.-Y. *Adv. Drug Deliv. Rev.* **2008**, *60*, 1278.

60. Hudson, S.P.; Padera, R.F.; Langer, R.; Kohane, D.S. *Biomaterials* **2008**, *29*, 4045.

61. Vallet-Regi, M.; Ramila, A.; del Real, R.P.; Perez-Pariente, J. *Chem. Mater.* **2001**, *13*, 308.

62. Gruenhagen, J.A.; Lai, C.-Y.; Radu, D.R.; Lin, V.S.-Y.; Yeung, E. *Appl. Spectrosc.* **2005**, *59*, 424.

63. Xia, T.; Kovochich, M.; Liong, M.; Meng, H.; Kabehie, S.; George, S.; Zink, J.I.; Nel, A.E. *Acs Nano* **2009**, *3*, 3273.

64. Tsai, C.-P.; Chen, C.-Y.; Hung, Y.; Chang, F.-H.; Mou, C.-Y. *J. Mater. Chem.* **2009**, *19*, 5737.

65. Rosenholm, J.M.; Meinander, A.; Peuhu, E.; Niemi, R.; Eriksson, J.E.; Sahlgren, C.; Linden, M. *Acs Nano* **2009**, *3*, 197.

66. Yang, S.; Zhao, L.; Yu, C.; Zhou, X.; Tang, J.; Yuan, P.; Chen, D.; Zhao, D. *J. Am. Chem. Soc.* **2006**, *128*, 10460.

67. Ohsuna, T.; Liu, Z.; Che, S.; Terasaki, O. *Small* **2005**, 1, 233.

# Chapter 3

# Spectroscopic Study of the Physical States of the Encapsulated Cargo Molecules in Mesoporous Silica Nanoparticles

## 3.1. Abstract

In the last chapter we have demonstrated how much cargo can be loaded into the mesoporous silica nanoparticles, the next logical step would be to study the physical states of these encapsulated cargo molecules. Key questions include how mobile are the cargo molecules, and how rigid is the solvent inside the pore channels. In this chapter, we answer these two questions using the fluorescence depolarization and rigidochromism method, respectively. First, the time-resolved fluorescence depolarization and preliminary results for five samples of a Re complex dye will be presented to quantitatively describe the dye mobility. Then results of a steady-state depolarization study will be shown for MCM-41 samples loaded in different dye concentrations. Finally, the rigidochrmic studies on non-hollow and hollow particles will be described to show the difference in the internal environments for different particle morphologies.

## 3.2. Introduction

Mesoporous silica nanoparticles have attracted attention in recent years as easily-functionalized nano-sized containers for drug delivery applications. Many sizes and shapes of mesoporous silica nanoparticles with different pore morphologies exist for this purpose, and these are commonly derivatized with a variety of molecular machines. Since these systems are primarily designed to deliver cargo, knowledge of the nanoparticles' internal environments is essential. However, this information is difficult to obtain via traditional nanoparticle characterization methods.

Molecular probes are capable of relaying vast amounts of information about their environments, including cargo mobility, local viscosity, solvent reorganization ability,

and local polarity, pH, and solvent conditions.[1] These probes interact with their environments in a variety of ways, producing changes in emission intensity and spectral position. In this chapter, we use molecular dyes that exhibit large polarization and rigidochromic changes depending on their environments. With these molecular dyes, we investigate the internal environments of mesoporous silica nanoparticles and the molecule/matrix interactions involved in these structures.

The first type of experiment we performed provided information on the mobility of the cargo molecules encapsulated in the pore channels of mesoporous silica nanoparticles measures. In these experiments, the fluorescent cargo molecules in the samples were irradiated by polarized light, and then the fluorescence anisotropy of the emitted light was measured. The experimental setup is illustrated below.

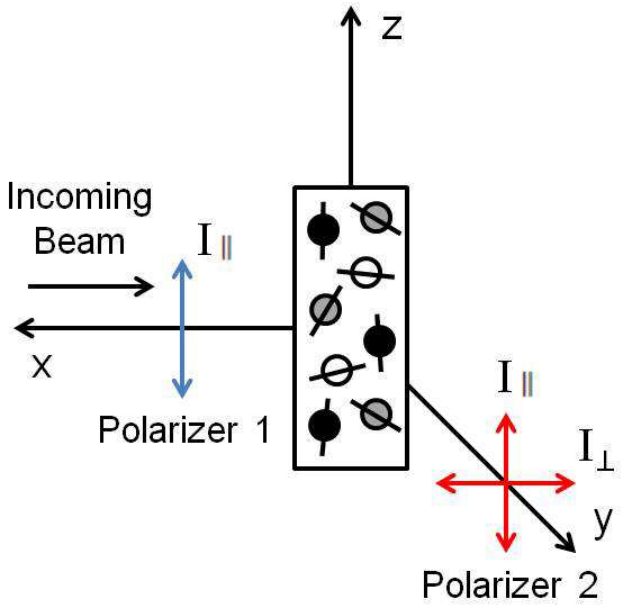


The sample is considered to be a collection of randomly oriented fluorophores. When it is irradiated with polarized light, fluorophores with transition dipoles aligned with the

electric field vector of the incoming radiation are preferentially excited, which is often referred to as photoselection. This results in partially polarized fluorescence emission. The degree of polarization of the emitted light can be determined by measuring the intensity of the emission parallel($I_{\parallel}$) and perpendicular($I_{\perp}$) to the polarization of the excitation beam. A decrease in the emission polarization indicates an increase of the cargo mobility.

The second type of experiment we performed utilizes the rigidochromic properties of certain fluorophores. Rigidochromic probes experience dipole shifts during excitation, temporarily creating a higher energy state where the solvent and probe dipoles are misaligned. If the solvent dipoles are slow to reorient because they are in a rigid environment, emission occurs from this higher energy state, causing blue-shifts in the probe's emission band maxima. If the environment is very fluid (i.e. reorganization occurs quickly), the emission band will occur at a longer wavelength. Therefore, rigidochromic probes can reveal intricate details of the local environments. Since the probes' luminescences in different environments appear at different wavelengths, a variety of local environments can be detected and investigated concurrently.

## 3.3. Results and Discussion

### 3.3.1. Time-resolved Fluorescence Anisotropy Studies

The strength of the oscillating electric field in a light wave can be expressed as $E = Acos(kx - \omega t + \varphi)$, where $A$ is the amplitude of the light wave. The energy carried by this light wave can be expressed by its intensity, $I$. Intensity is proportional to the square of amplitude ( $\propto A^2$). Now if we take a light wave vector that oscillates at an

angle θ from the vertical direction, we can see that the original amplitude does not equal to the sum of its vertical and horizontal components, $A_0 \neq A_{\parallel} + A_{\perp}$, but the original intensity value can be expressed as the sum of the its vertical and horizontal components, $I_0 = I_{\parallel} + I_{\perp}$.

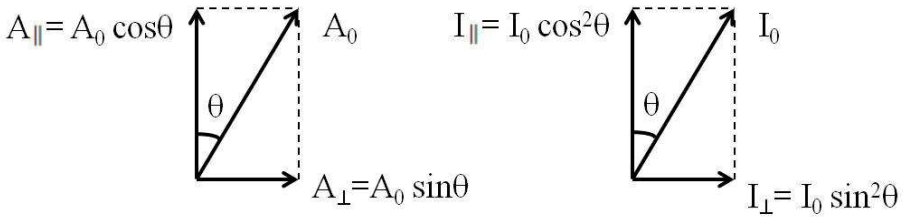


Since the intensity of a light wave vector in any direction can be broken down into its vertical and horizontal components, the intensity of an unpolarized light can be expressed as the sum of a vertical and a horizontal component of the same intensity.

The emission light signals we detect in the fluorescence depolarization experiments are considered partially polarized, which means that they contain a polarized component and an unpolarized component. The intensity of the polarized component can be expressed as a vertical vector. The intensity of the unpolarized component can be expressed as a vertical vector and a horizontal vector of the same length. The overall intensity of the partially polarized light is a superimposition of the polarized and the unpolarized components.

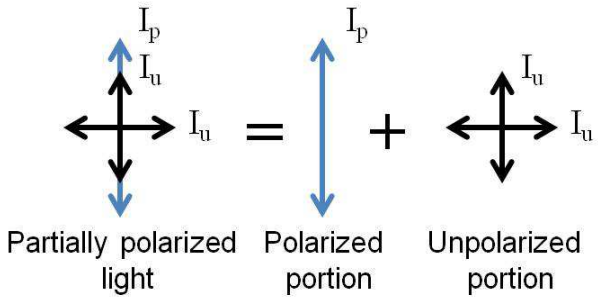

When the excitation laser beam is polarized in the vertical direction, the vertical direction is defined as the parallel direction, and the horizontal as the perpendicular direction. Therefore the emission intensity in the parallel and perpendicular directions can be expressed by the intensity of the polarized and unpolarized components in this partially polarized light beam.

$$\begin{cases} I_{\parallel} = I_p + I_u \\ I_{\perp} = I_u \end{cases}$$

Therefore,

$$\begin{cases} I_p = I_{\parallel} - I_{\perp} \\ I_t = I_{\parallel} + I_{\perp} \end{cases}$$

Herein, we define the polarization value ($P$) of this emission light to be the intensity of the polarized component over the total emission intensity.

$$P = \frac{I_p}{I_t} = \frac{I_{\parallel} - I_{\perp}}{I_{\parallel} + I_{\perp}}$$

The above equation applies when the light is only polarized in two dimensions. However, this is not true for a sample that emits three-dimensionally, in which case there are two perpendicular components of the same strength. The total emission intensity would then be,

$$I_t = I_{\parallel} + 2I_{\perp}$$

We define the intensity of the polarized component over the total emission intensity in this case as fluorescence anisotropy ($r$).

$$r = \frac{I_p}{I_t} = \frac{I_{\parallel} - I_{\perp}}{I_{\parallel} + 2I_{\perp}}$$

Additionally, the *G* factor is defined as the relative sensitivity of the detector between the parallel and the perpendicular directions.

$$\begin{cases} I_{\parallel} = S_{\parallel} \times I_u \\ I_{\perp} = S_{\perp} \times I_u \end{cases}$$

$$G = \frac{S_{\parallel}}{S_{\perp}} = \frac{I_{\parallel}}{I_{\perp}}$$

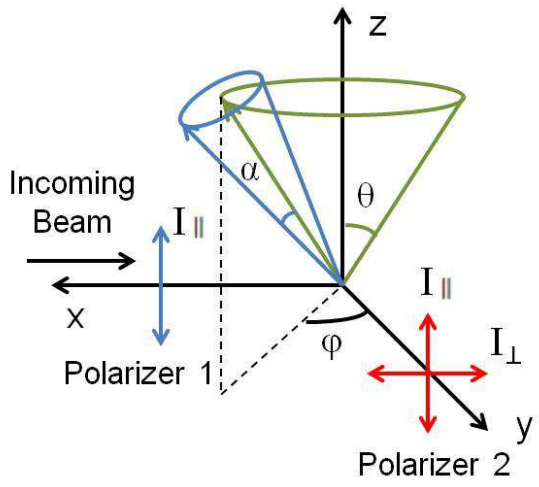


If a fluorophore at angle θ absorbs the vertically polarized excitation light, the emission given out in the parallel direction is

$$I_{\parallel} = cos^2\theta \cdot I_0$$

The emission in the perpendicular direction is

$$I_{\perp} = sin^2\theta \cdot sin^2\varphi \cdot I_0$$

We then average $sin^2\varphi$ over all the $\varphi$ angles,

$$\frac{\int_0^{2\pi} sin^2\varphi d\varphi}{\int_0^{2\pi} d\varphi} = \frac{1}{2\pi}\int_0^{2\pi} sin^2\varphi d\varphi = \frac{1}{2\pi}\int_0^{2\pi} \frac{1-cos2\varphi}{2} d\varphi = \frac{1}{2\pi}\left(\frac{2\varphi - sin2\varphi}{4}\right)_0^{2\pi} = \frac{1}{2}$$

The emission in the perpendicular direction then becomes

$$I_{\perp} = sin^2\theta \cdot sin^2\varphi \cdot I_0 = \frac{1}{2} sin^2\theta \cdot I_0$$

The *r* value for this particular molecule,

$$r = \frac{I_{\parallel} - I_{\perp}}{I_{\parallel} + 2I_{\perp}} = \frac{cos^2\theta \cdot I_0 - \frac{1}{2} sin^2\theta \cdot I_0}{cos^2\theta \cdot I_0 + 2 \cdot \frac{1}{2} sin^2\theta \cdot I_0} = \frac{3cos^2\theta - 1}{2}$$

Now if we would like to calculate the overall *r* value for all the molecules in the sample, we need to take into account the probability of a molecule at the angle $\theta$ to absorb the excitation light (proportional to $cos^2\theta$), and the population of molecules at the angle $\theta$ (proportional to the size of the cone, $sin\theta$).

$$P_{\theta} = cos^2\theta \cdot sin\theta$$

Therefore, the overall parallel intensity is

$$I_{\parallel} = I_0 \int_0^{\pi} P_{\theta} cos^2\theta d\theta = I_0 \int_0^{\pi} cos^4\theta sin\theta d\theta = (-\frac{1}{5} I_0 cos^5\theta)_0^{\pi} = \frac{2}{5} I_0$$

Similarly, the overall perpendicular intensity is

$$I_{\perp} = I_0 \int_0^{\pi} \int_0^{2\pi} P_{\theta}\, sin^2\theta sin^2\varphi d\varphi d\theta = \frac{1}{2} I_0 \int_0^{\pi} cos^2\theta sin^3\theta d\theta$$

$$= -\frac{1}{2} I_0 \int_0^{\pi} cos^2\theta (1 - cos^2\theta) dcos\theta = -\frac{1}{2} I_0 (\frac{1}{3} cos^3\theta - \frac{1}{5} cos^5\theta)_0^{\pi}$$

$$= \frac{2}{15} I_0$$

Thus when the molecules do not move, the anisotropy value due to the absorption probability at different angles can be calculated as

$$r_1 = \frac{I_{\parallel} - I_{\perp}}{I_{\parallel} + 2I_{\perp}} = \frac{\frac{2}{5} I_0 - \frac{2}{15} I_0}{\frac{2}{5} I_0 + 2 \cdot \frac{2}{15} I_0} = \frac{2}{5}$$

This is the maximum *r* value one can get. Correspondingly, the maximum *P* value is

$$P = \frac{I_{\parallel} - I_{\perp}}{I_{\parallel} + I_{\perp}} = \frac{1}{2}$$

For a certain fluorophore, the orientation of its emitting dipole moment may be different from the absorbing dipole moment. If there exists an angle α between the two dipole moments, the loss in the emission polarization due to this angle is

$$r_2 = \frac{3cos^2\alpha - 1}{2}$$

In a frozen solution containing a collection of immobilized fluorophores, the fluorescence anisotropy are calculated upon taking into account the photoselection during excitation and the angle between the absorption and emission transition dipoles,

$$r_0 = r_1 \cdot r_2 = \frac{2}{5} \cdot \frac{3cos^2\alpha - 1}{2} = \frac{3cos^2\alpha - 1}{5}$$

In the case of liquid solutions, the rotational diffusion of the fluorophores occurs on a comparable timescale of the fluorescence decay. This leads to the depolarization of the emitted radiation. In non-viscous solvents at room temperature, the experimentally observable r value of free fluorophores decays exponentially due to the rotational tumbling motion of the molecules. The lifetime of this decay is defined as the rotational correlation time $\tau_c$.

$$r(t) = r_0 e^{-t/\tau_c}$$

$$= \frac{3cos^2\alpha - 1}{5} \cdot e^{-t/\tau_c} = \frac{I_{\parallel}(t) - I_{\perp}(t)}{I_{\parallel}(t) + 2I_{\perp}(t)}$$

The total emission intensity decays over time as well, where $\tau_F$ is the fluorescence lifetime for this particular fluorophore.

$$I_t(t) = I_0 e^{-t/\tau_F} = I_{\parallel}(t) + 2I_{\perp}(t)$$

The expressions for the parallel and perpendicular intensity as a function of time can be solved from the above two equations.

$$I_{\parallel}(t) = I_0 \left[\frac{1}{3} + (\frac{4}{15}) e^{-t/\tau_c} \frac{3cos^2\alpha - 1}{5}\right] e^{-t/\tau_F}$$

$$I_{\perp}(t) = I_0 \left[\frac{1}{3} - (\frac{2}{15}) e^{-t/\tau_c} \frac{3cos^2\alpha - 1}{5}\right] e^{-t/\tau_F}$$

The expressions for $I_t(t)$, $r(t)$, $I_{\parallel}(t)$ and $I_{\perp}(t)$ are the main fitting equations for our time-resolved fluorescence anisotrpy data.

The fluorescence anisotropy can also be observed in steady-state data collection modes. In the steady-state mode, samples are illuminated continuously at constant incident light intensity. Since the illumination time is significantly longer than the fluorescence lifetime, steady-state experiment yields a time-averaged view of anisotropy. The steady-state anisotropy is mathematically defined as the normalized average of the time-resolved anisotropy, $r(t)$, weighted by the total time-dependent fluorescence emission, $I_t(t)$.

$$r = \frac{\int_0^{\infty} r(t) I_t(t)\, dt}{\int_0^{\infty} I_t(t)\, dt}$$

When the fluorophores in two samples are in similar environments and have similar fluorescence lifetimes, the steady-state anisotropy is an easy analysis to determine the relative mobility of the fluorophores in these two samples.

The time-resolved fluorescence depolarization experiments were performed on an aqueous solution of (sodium bathocuproine disulfonate)$Re(CO)_3Cl$. The fluorescence

lifetime $\tau_F$ obtained from the fluorescence decay when no polarizer was placed in front of the detector is 0.99 ± 0.01 μs. The initial r value is 0.010 ± 0.001, and the rotational correlation time $\tau_c$ fitted from the $I_{\parallel}(t)$-$t$ , $I_{\perp}(t)$-$t$ and $r(t)$-$t$ curves are 0.17, 0.26 and 0.11 μs, respectively (Figure 3.1). When the same experiments were performed on a solid state sample, the initial r value becomes 0.28 ± 0.02, which is significant higher than that of the solution sample. The rotational correlation time $\tau_c$, 2.30 ± 0.05 μs is also longer. These results demonstrate the lower mobility of the dye molecules in the solid state sample. The fluorescence lifetime for the solid sample (0.51 ±0.03 μs), on the other hand, is slightly shorter than the solution sample, which can be explained by the intermolecular energy transfer between the solid state dye molecules.

The Re complex was then loaded into MCM-41 meosporous silica nanoparticles and the time-resolved fluorescence decays were measured on a dry sample of the loaded particles, and on samples that are immersed in water or toluene. The initial r value for the dry sample is 0.39 ± 0.01, which is very close to the maximum r (Figure 3.2). This can be explained by the low mobility of dye molecules when they reside in the pore channels with no solvent around. The rotational correlation time fitted from the $r(t)$-$t$ curve is 3.43 ± 0.09 μs, which is much higher than that for the dye solution sample. This also proves the slow rotational motion of the encapsulated dye molecules. The fluorescence lifetime can be fitted from the $I_t(t)$ -$t$ curve using a biexponential function, with the two components at 1.6 and 0.44 μs, respectively. This demonstrates that there are two populations of dye molecules in the sample with different lifetimes. The 0.44 μs lifetime is close to that of the solid state dye sample, and therefore corresponds to the dye

molecules that have little or no interaction with the silica matrix. It has been observed for other fluorophores that the fluorescence lifetime becomes longer when the dye molecules are attached to a matrix. The population with the fluorescence lifetime of 1.6 μs corresponds to the dye molecules that are more tightly adsorbed onto the pore walls.

When the dye-loaded particles are immersed in water, the initial r value (0.04 ± 0.01) decreased to the level of the solution sample (Figure 3.3), which shows that solvent molecules are getting into the pore channels and serves to increases the mobility of the encapsulated dye molecules. Two different components emerged while fitting the rotational correlation time $\tau_c$ from the $r(t)$-$t$ curve, showing two separate dye populations with different rotational diffusion rates. One of the two populations has a $\tau_c$ of 0.09 ± 0.05 μs, which is close to the solution value, and therefore corresponds to the dye molecules that are dissolved into the solvent. The other less mobile population has a longer $\tau_c$ of 2.1 ± 0.4 μs, which corresponds to the dyes that stay within the pore channels.

The $r_0$ and $\tau_c$ values for the dye-loaded particles immersed in toluene are 0.19 ± 0.01 and 1.11 ± 0.04 μs, respectively (Figure 3.4), which are higher than the values in water, but lower than the values for the dried particle sample. These results demonstrate that the the dye molecules have a lower mobility in toluene than in water, which is consistent with the higher viscosity of toluene. The Re dye molecule does not dissolve in toluene, therefore only one rotational correlation time was obtained from the $r(t)$-$t$ curve. The results for the above five samples have demonstrated that the $r_0$, $\tau_F$ and $\tau_c$ values from the time-resolved fluorescence anisotropy measurements can be used to describe the relative dye mobility within each sample. The results are summarized in Table 3.1.

### 3.3.2. Steady-State Fluorescence Anisotropy Studies

The water-soluble dye Hoechst 33342 was chosen as the probe for the steady-state fluorescence anisotropy studies primarily for its large change in polarization in different environments.[5] All studies done in this subsection were performed using MCM-41 nanoparticles of ~100 nm in diameter, with ~2.5 nm pores. These nanoparticles were capped using the acid valve described (see Methods) and washed many times to ensure that the observed emission from the Hoechst dye originates from inside the pores. Observed polarization values for the dyes in these nanoparticles (see Figure 3.5) ranged from $P$ = 0.1 to $P$ = 0.3. This is typical of the polarization range of Hoechst molecules reported in the literature.[5, 7]

Figure 3.5 is a polarization profile of capped MCM-41 samples with different loading concentrations of Hoechst dye. The polarization values for these samples are comparable because the fluorophores are located in similar environments, and the fluorescence lifetime of the Hoechst molecules are very similar. The profile exhibits a maximum polarization at 1 mM loading concentration, but at high loading concentrations reaches a polarization minimum of ~0.13. It was expected that polarization would increase steadily at higher loading concentrations, but the opposite was found.

One likely explanation for this is the occurrence of Förster Resonance Energy Transfer (FRET) at higher concentrations that reduces the polarization of the emission. Studies of Hoechst in cell nuclei by Peterson et al. have concluded that losses due to energy transfer between Hoechst molecules can lead to significantly diminished polarization values, depending on concentration.[6]

The likelihood of FRET transfer depends on the average distances between dyes and the Förster distance $R_0$. The Förster distance, where intermolecular energy transfer becomes 50% efficient, is given by

$$R_0^6 = 9.78 \cdot 10^3 (\kappa^2 n^{-4} \Phi J) ,$$

where $\kappa^2$ is the orientation factor that depends on the orientation of the dipoles of the donor and acceptor, $n$ is the refractive index of the medium (1.345 for water near 400 nm),[8] $\Phi$ is the quantum yield of the donor, and $J$ is the spectral overlap integral given by

$$J = \int F_D(\lambda) \varepsilon_A(\lambda) \lambda^4 d\lambda / \int F_D(\lambda) d\lambda ,$$

where $F_D$ is the fluorescence intensity of the donor and $\varepsilon_A$ is the molar absorbance of the acceptor.[9]

$R_0$ was calculated for this system to be 1.3 nm using absorption and emission spectra of Hoechst and PhotochemCAD 2.1 software.[10] This assumes an orientation factor ($\kappa^2$) of 2/3, meaning that the Hoechst dyes are in a random orientation. Calculations using data from a recent loading capacity study[11] suggest that there are on average 10 Hoechst molecules loaded per 75 nm-long MCM-41 pore at a loading concentration of 1 mM, and a maximum of 40 Hoechst molecules loaded per 75 nm MCM-41 pore at loading concentrations of ~5 mM and higher. Taking a typical pore to be cylinder-shaped, this results in an average distance between dye molecules of 4.6 nm at a 1 mM loading capacity, and 3.2 nm at a 3 mM loading capacity. A 3.2 nm distance between molecules with a Förster distance of $R_0$ =1.3 nm results in less than a 1% likelihood of energy transfer. However, this calculation assumes that all molecules are evenly spaced, so the real distance between Hoechst molecules is less than 3.2 nm.

Moreover, the quantum yield of Hoechst is likely to be much higher when it is interacting with the pore wall (i.e. increases from .034 to .22 when in solution to when intercalated in single stranded DNA) and also displays a blue-shift in its emission from 490 to 466. Taken together, these two changes increase the Förster distance from 1.3 nm to 1.9 nm, and increase the likelihood of transfer between two molecules with an average distance of 3.2 nm to 4%.[10] Although a FRET efficiency less than 5% will not affect polarization to a significant degree, the calculated transfer efficiency is probably underestimated by the calculations in this section because: (1) the available pore volume is likely smaller than estimated due to crowding from the linker and cyclodextrin cap, (2) the orientation factor $\kappa^2$ may increase due to the molecules aligning vertically in the pores, (3) the lifetime has been shown to increase when Hoechst interacts with DNA (in solutions of double stranded DNA Hoechst's lifetime increases almost ten-fold relative to aqueous solutions) so it could also increase due to electrostatic interactions with the silica surface of these particles and (4) the quantum yield of the dye interacting with the silica surface is probably even higher than .22 (in solutions of double stranded DNA Hoechst's quantum yield increases to .38). Therefore, a moderate amount of FRET transfer is expected in our system, but the degree to which this occurs is unknown.

According to the polarization profile in Figure 3.5, the system appears to reach a minimum polarization at a concentration of 3 mM, and does not change significantly past that value. A recent study by Li et al[11] indicates that the Hoechst loading capacity for MCM-41 particles reaches a maximum value between 1 mM and 10 mM, and past this point dye loading concentration increases have no effect on amount of dye uptake. It is

possible that the minimum polarization values seen in the 3-10 mM part of Figure 3.5 indicates that maximum loading capacity for these particles occurs at 3 mM. The polarization does not change significantly past this point because the concentration of dye inside the pores has reached its maximum.

### 3.3.3. Rigidochromic Studies

Since Hoechst undergoes only minor wavelength shifts in nanoparticle environments, rhenium-based complexes were chosen for rigidochromic measurements. While $ClRe(CO)_3$(2,2‘-bipyridine) is typically used for rigidochromic measurements in sol gels,[12] it is not entirely soluble in water and requires alcohol/water mixtures to dissolve fully. Since even small quantities of alcohol can release the acid valve cap, we instead synthesized a water-soluble rigidochromic rhenium-based complex, (sodium bathocuproine disulfonate)$Re(CO)_3Cl$, that has been used previously as a probe for the setting of gypsum plaster (synthesis shown in Figure 3.6).[2] This complex also exhibited polarization changes, but to a lesser degree than that observed in Hoechst.

Rigidochromic probes exhibit a change in dipole moment upon excitation, temporarily creating a high energy configuration where the nearby solvent molecule dipoles are misaligned, resulting in a high energy configuration. If the solvent molecules reorient quickly, no effect will be seen. However, if the solvent is slow to reorient (or if the lifetime of the dye is very short), emission will occur while in this high energy configuration. The resulting degree of blue-shift seen in the spectrum depends on the solvent's reorganization ability.

The rhenium complex [(sodium bathocuproine disulfonate)$Re(CO)_3Cl$] fluoresces at 590 nm in water. Its spectrum broadens considerably when trapped inside MCM-41 nanoparticles (see Figure 3.7), indicating that the dye is experiencing a wide variety of environments. While a majority of the emission is blue-shifted (as expected when solvent mobility is hindered), some emission appears to be red-shifted (indicating there may be areas inside MCM-41 where solvent reorganization is enhanced). The fact that this red-shifted population is seen with the anionic rhenium dye and not cationic Hoechst is thought to depend on the low degree of electrostatic interaction between the negatively charged pore walls and the negatively charged dye. Additionally, the rhenium probe contains hydrophilic and hydrophobic regions that can interact with water and the pore walls in multiple ways. More work is needed to fully characterize the interactions of the rhenium complex and solvent with the silica walls inside the pores.

The internal environments within non-hollow and hollow particles were compared by loading the Re complex into both types of particles. To make more efficient use of the hollow particles, a modification of the loading procedure was used. In this new procedure, modeled after other successful methods involving consecutive dye impregnation and drying cycles to increase loading capacity,[13, 14] the particles were loaded with 1 mM rhenium dye three times, fully drying the particles under vacuum between each loading step. Emission spectra of the non-hollow and hollow particles (Figure 3.8) loaded with each method are plotted in Figure 3.9. With a higher loading dose, the dye emission from the non-hollow particles had a larger P value at the emission maximum, but no significant change in peak position. This indicates a denser packing of dye molecules with no change

in solvent environment. However, when the hollow particles are loaded three times, the emission maximum red shifted, along with a slight decrease in P value. This indicates that the dye molecules are within a less rigid environment and are less densely packed, which can be an indication of dye molecules entering the hollow cavity. These results demonstrated the different internal environments within the non-hollow and hollow particles.

### 3.4. Conclusions

Two types of spectroscopic methods were used to study the mobility of the encapsulated cargo molecules in mesoporous silica nanoparticles and the internal solvent rigidity of these particles. The fluorescence depolarization studies, which can be performed in time-resolved and steady-state fashions, provide information on the cargo mobility. Time-resolved experiments on five different samples with a Re complex probe demonstrated that the mobility of the dye molecules decreases in the order of dye solution > dye-loaded particles in water > dye-loaded particles in toluene > solid-state dye samples > solid-state dye-loaded particles. Steady-state fluorescence depolarization studies on Hoechst 33342 loaded MCM-41 particles demonstrated that the polarization values depend on the loading concentrations. As the loading concentration increases, the P values first increase due to the increase in dye packing density, and then decrease due to the intermolecular energy transfer between neighbouring dye molecules.

The rigidochromic studies on non-hollow and hollow particles loaded with the water soluble Re complex were able to show the differenct internal environments between the two types of particles. When the hollow particles are loaded with more cargo,

the red shift in the cargo emission indicates that the molecules are being forced into the hollow cavity of these particles. This red shift in emission maximum is absent in the non-hollow particles.

### 3.5. Experimental

Polystyrene (Aldrich) was vacuum distilled to remove the inhibitor, but all other analytical and reagent grade materials were used as purchased without further purification or modification: cetyltrimethylammonium bromide (CTAB) [≥98%, Sigma], tetraethyl orthosilicate (TEOS) [98%, Aldrich], Tetrahydrofuran (THF) [Sigma Aldrich], Rhenium pentacarbonyl choride, 98%, ACROS Organics, Bathocuproinedisulfonic acid, disodium salt hydrate, 97%, ACROS Organics, Bisbenzimide H 33342 (Hoechst 33342) [≥98%, Aldrich], sodium hydroxide (NaOH) [certified ACS, Fisher], hydrochloric acid (HCl) [certified ACS plus, Fisher ], methanol [certified ACS, Fisher], ethanol [certified ACS, Fisher], acetone [certified ACS, Fisher], ammonium hydroxide solution [28 wt%, certified ACS, Fisher], sodium dodecyl sulfate (SDS) [Sigma Aldrich], Potassium persulfate (KPS) [Sigma Aldrich], 1-pentanol [Sigma Aldrich], N-phenylaminomethyl)triethoxysilane (PhAMTES) [≥95%, Gelest], and α-cyclodextrin (α-CD) [98%, Sigma]. The water-soluble rigidochromic probe (sodium bathocuproine disulfonate)$Re(CO)_3Cl$ was synthesized according to the procedure given by Volger et al. (see Figure 3.6).[2]

*Synthesis of MCM-41 Mesoporous Silica Nanoparticles:* To prepare the 2D-hexagonal MCM-41 mesoporous silica nanoparticles (MCM-41 nanoparticles), CTAB (250 mg, 0.67 mmol) was dissolved in deionized $H_2O$ (120 mL) with a 2M NaOH water

solution (0.875 mL).[3] The mixture was stirred and heated to 80 °C when TEOS (1.25 mL, 6 mmol) was slowly added into the solution. TEOS was allowed to hydrolyze for 2 hours and the reaction was cooled down to room temperature. The product was collected by centrifugation and washed with methanol. To remove the templating surfactant molecules from the mesopores, 250 mg of the as-synthesized MCM-41 nanoparticles were suspended in acidic methanol. The mixture was refluxed under nitrogen for 12 hours. The solvent extracted particles were collected by centrifugation, washed by methanol, and dried under vacuum. Transmission electron microscopy (Figure 3.8) and powder x-ray diffraction (not shown) techniques were used for characterization and reveal the existence of highly ordered hexagonally-packed pores.

*Synthesis of Mesoporous Hollow Spheres:* Mesoporous hollow spheres were synthesized around polystyrene spheres (PS). PS spheres were made with the following procedure: a 250 mL round-bottom flask was filled with 100 mL water, KPS (0.2 g; 0.74 mmol), and SDS (0.14 g 0.49 mmol). Solution was stirred for 1 hour at room temperature. Another 10 mL flask was filled with styrene (5 g; 48 mmol) and 1-pentanol (0.1 g; 1.13 mmol). $N_2$ was bubbled through the two flasks for one hour and water solution was heated to 70 $^{o}$C while being stirred at 600 rpm. At a temperature of 70 $^{o}$C, the styrene and 1-pentanol mixture was added dropwise to the solution. This solution was stirred at 600 rpm for 12 hours at 70 $^{o}$C. White sol solution was obtained then centrifuged and washed three times with a 1:1 ethanol/water solution.

Mesoporous hollow spheres were prepared by controlled growth of the mesoporous silica wall in PS spheres in an ethanol/water mixture. CTAB (0.64 g) was

dissolved in water (120 mL) and PS (0.265 g) and ethanol (45 mL) were added to the solution. The mixture was stirred at room temperature for one hour, and then 28 wt% ammonium hydroxide solution (0.11 mL) and TEOS (0.8 g) were added. The above reaction mixture was continuously stirred for an additional 48 hours and heated to 80 $^{o}$C for 24 hours. The white solid product was centrifuged and washed with a 1:1 solution of water and ethanol three times and dried in a vacuum oven overnight. The CTAB surfactant was removed by stirring the as-synthesized sample (500 mg) in 80 mL of methanol with 0.3 grams of ammonium nitrate at 60 $^{o}$C for 15 minutes. The resulting solid was centrifuged, washed with cold ethanol three times, and dried under vacuum. The PS was extracted by stirring in THF (50 mL) for 12 hours at room temperature. The product was centrifuged, washed with a 1:1 acetone/THF solution three times, and dried under vacuum. Both extracting procedures were conducted twice to fully extract CTAB and PS, and TEM (CM 120 microscope located at California NanoSystems Institute) confirmed the presence of intact hollow nanoparticles of diameter ~130 nm with ~80 nm hollow interiors (see Figure 3.8).

*Construction of the Acid-Responsive Nanovalves:* The methods for the assembling the acid-responsive nanovalves have been described in our previous work.[4] Typically, the solvent extracted nanoparticles (100 mg) were suspended in dry toluene (10 mL). Then 30 μL (0.1 mmol) of N-phenylaminomethyl)triethoxysilane was added into the particle suspension under stirring. The mixture was stirred at room temperature under nitrogen for 24 hours. The product was collected by centrifugation, washed extensively with methanol, and dried under vacuum. Dye molecules were loaded into the nanoparticles by soaking 50

mg of the PhAMTES-modified nanoparticles in 1 mL aqueous solution of the dye at room temperature for 3 days. Finally, the loaded samples were capped with α-cyclodextrin (0.1 g, 0.1 mmol) at room temperature for 24 hours. The final product was collected by centrifugation and washed with deionized water. The particles were dried under vacuum prior to the spectroscopic measurements, and placed in the end of an NMR tube for the spectroscopic analysis. Prior to spectroscopic analysis, the particles were rewetted with deionized water to resolvate the dyes inside the pores.

*Spectroscopic Techniques:* In the time-resolved fluorescence depolarization studies, samples were excited by a Optical Parametric Oscillator MagicPrism (OPOTEK), bumped by a Brilliant Compact Pulsed Nd:YAG laser (Quantel). Time-resolved data were collected by a PI-MAX intensified CCD camera (Princeton Instruments). In the steady-state fluorescence depolarization studies, the rhenium probe was excited using the 407 nm line from a Coherent I302C krypton ion laser, and the Hoechst probe was excited using the 351 nm line from a Coherent I306C argon ion laser. The dyes are relatively robust, but all laser powers were less than 5 mW to minimize damage to the linker and acid-valve in the capped system. Emission was collected throughout the visible region using an Acton 2300i monochromator and a CCD (Princeton Instruments). A Glan-Thompson polarizer was used to select out parallel and perpendicular emission components, and a polarization scrambler was used to reduce polarization-related spectral bias. The optics were tested with an isotropic light source, with a resulting error of <0.5% between parallel and perpendicular intensity measurements.

## 3.6. Figures and Tables

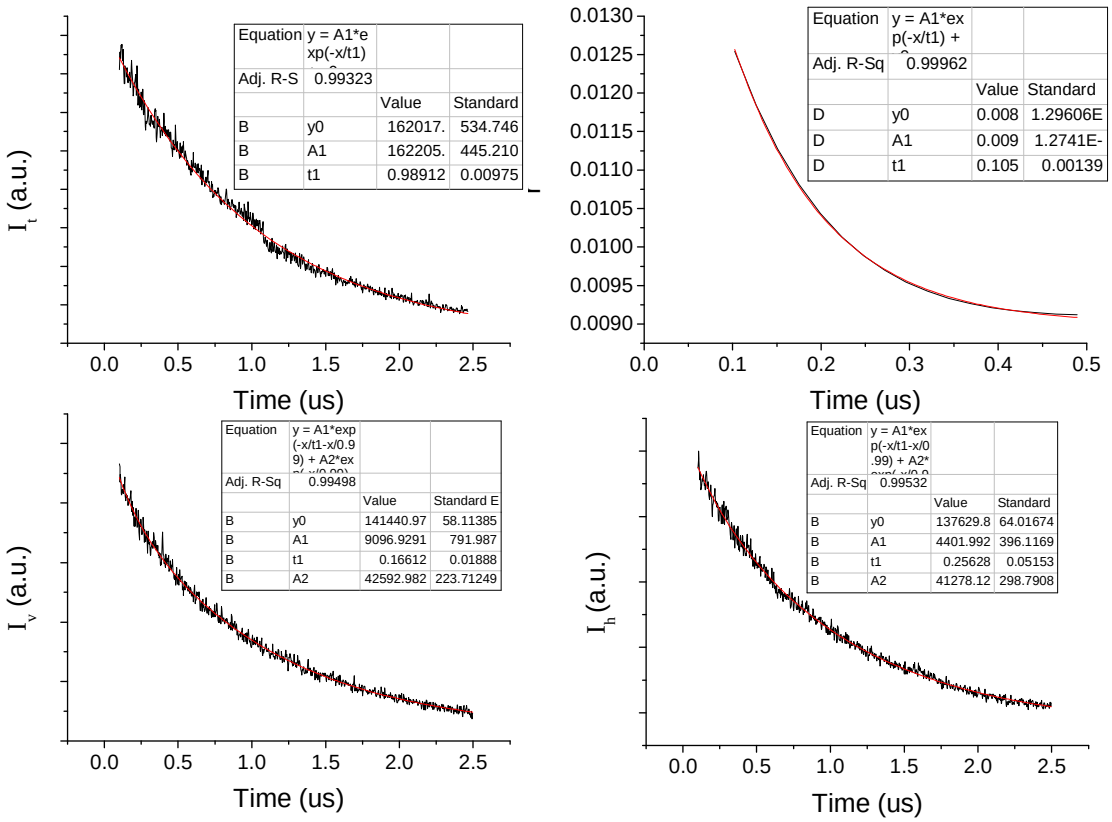


**Figure 3.1.** $I_t(t)$-$t$, $r(t)$-$t$, $I_{\|}(t)$-$t$ and $I_{\perp}(t)$-$t$ data collected on (sodium bathocuproine disulfonate)$Re(CO)_3Cl$ in aqueous solution.

A)

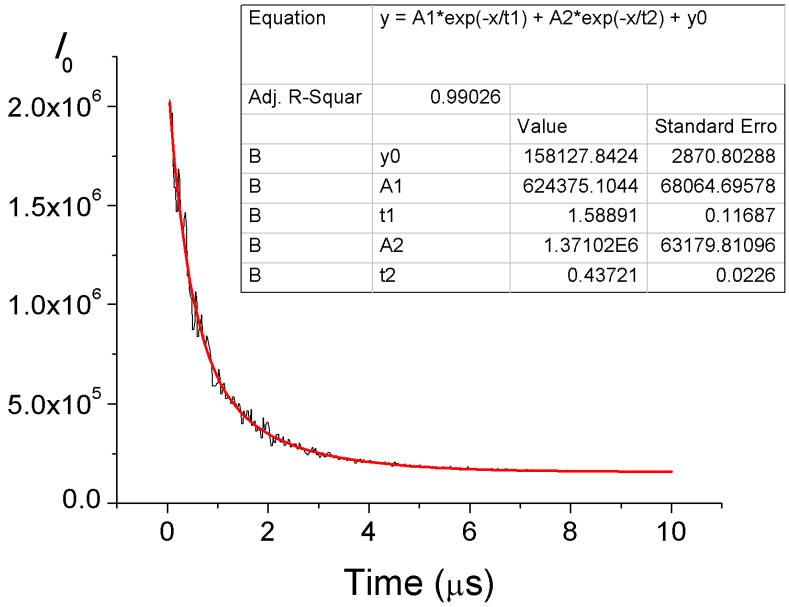


B)

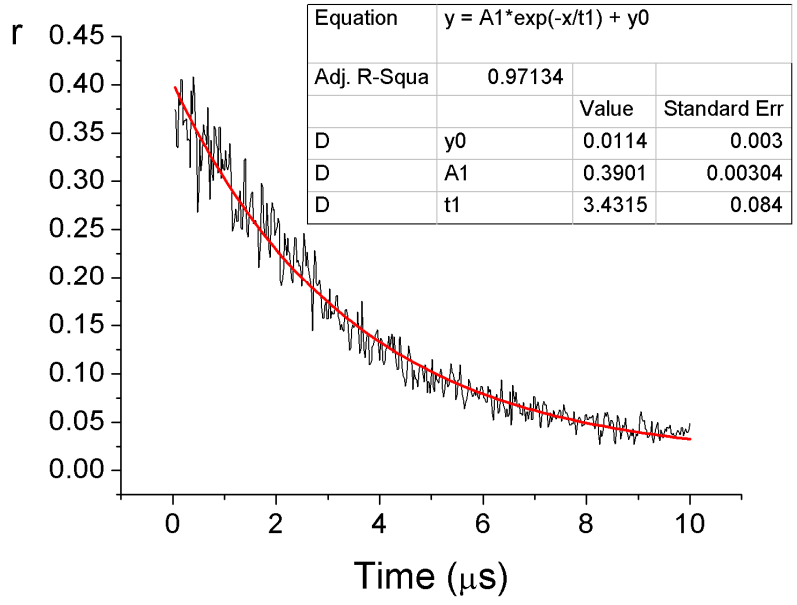


**Figure 3.2.** A) $I_t(t)$-$t$ and B) $r(t)$-$t$ data collected on dry MCM-41 particles loaded in 2.5 mM (sodium bathocuproine disulfonate)$Re(CO)_3Cl$ solution.

A)

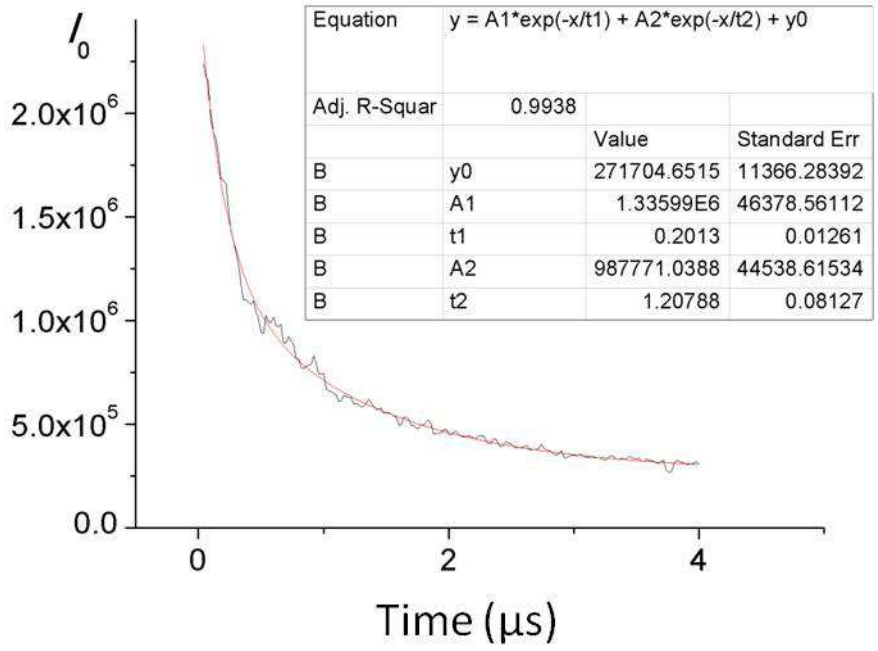


B)

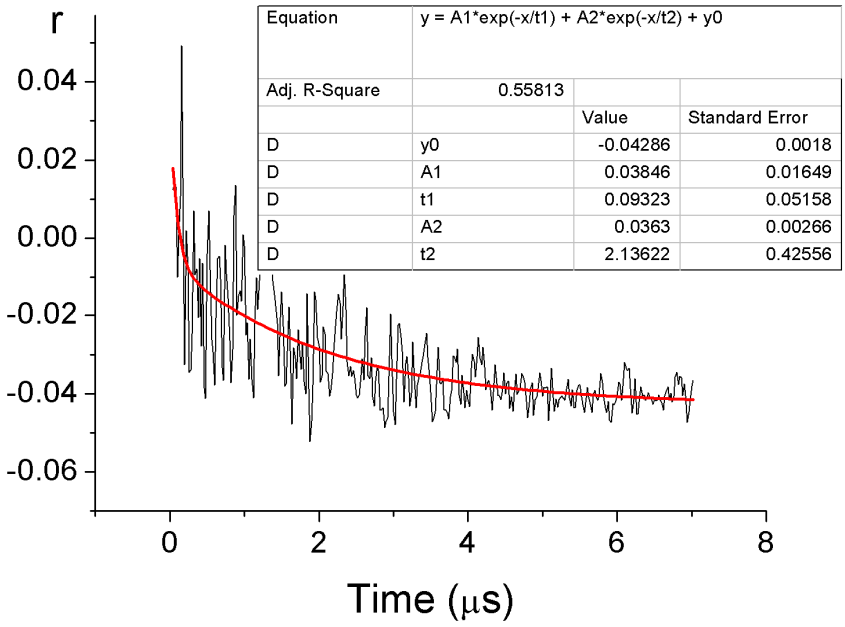


**Figure 3.3.** A) $I_t(t)$-$t$ and B) $r(t)$-$t$ data collected on water immersed MCM-41 particles loaded in 2.5 mM (sodium bathocuproine disulfonate)$Re(CO)_3Cl$ solution.

A)

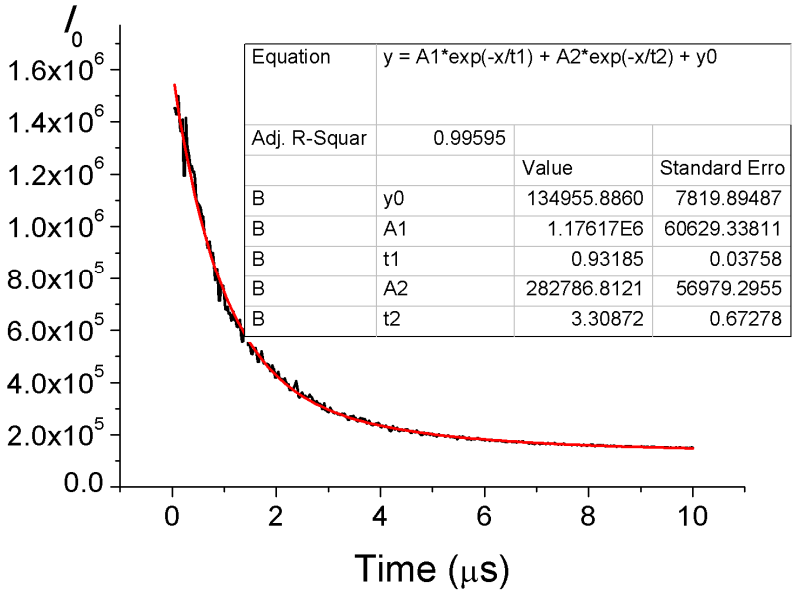


B)

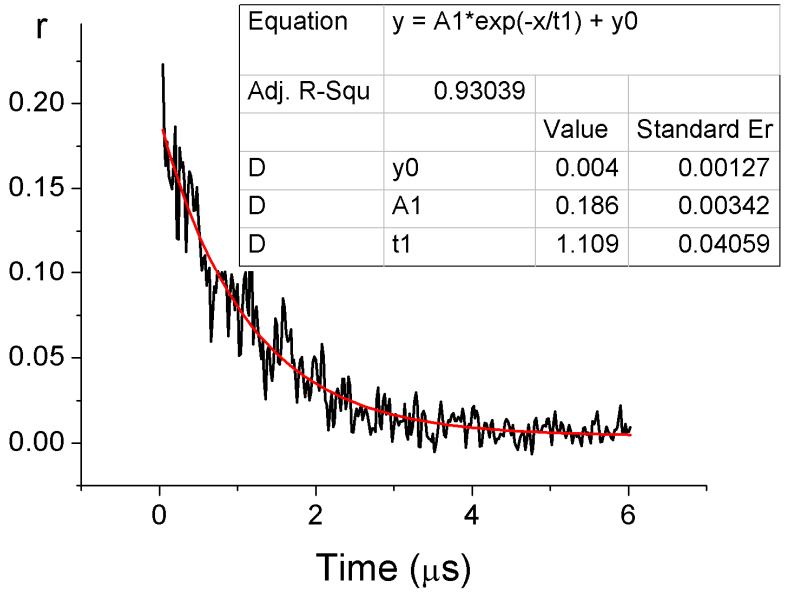


**Figure 3.4.** A) $I_t(t)$-$t$ and B) $r(t)$-$t$ data collected on toluene immersed MCM-41 particles loaded in 2.5 mM (sodium bathocuproine disulfonate)$Re(CO)_3Cl$ solution.

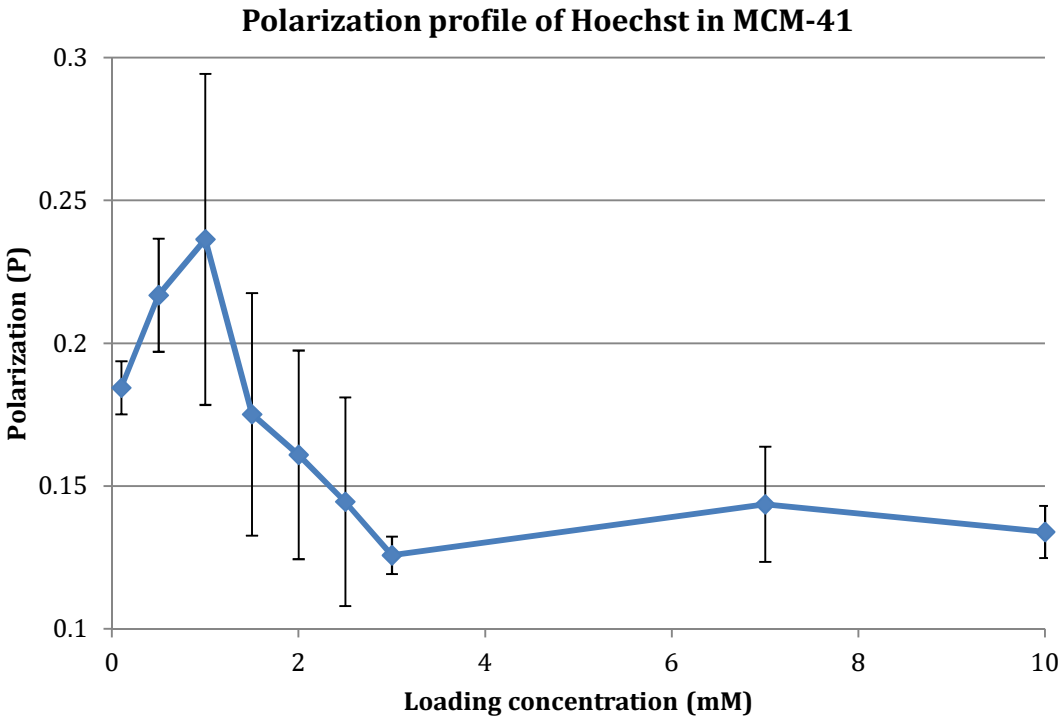


**Figure 3.5.** Polarization profile of Hoechst 33342 in MCM-41 as a function of loading concentration. Error bars represent standard deviations of the data trials.

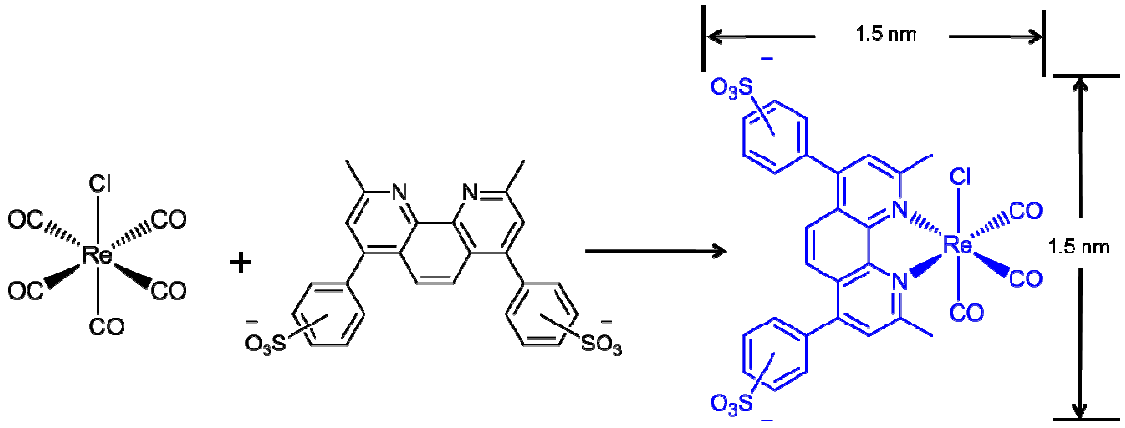


**Figure 3.6.** Synthesis and dimensions of (sodium bathocuproine disulfonate)$Re(CO)_3Cl$. The final product has dimensions of roughly 1.5 nm x 1.5 nm.

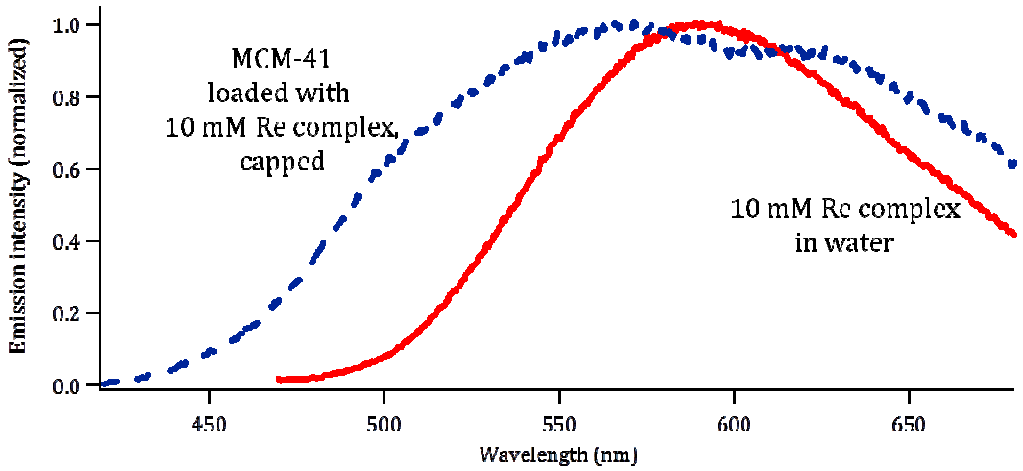


**Figure 3.7.** Emission spectra of (sodium bathocuproine disulfonate)$Re(CO)_3Cl$ in MCM-41 compared to solution. The dashed trace is the emission intensity seen from the water-soluble rhenium complexes loaded into MCM-41 nanoparticles and capped with the acid valve. The MCM-41 nanoparticles were wetted with deionized water prior to spectral analysis in order to resolvate the dye molecules inside the pores. The solid trace is a 10 mM solution of the rhenium complex freely-rotating in deionized water (emission maximum = 590 nm). The rhenium dyes experience a wide range of environments when loaded in MCM-41, some hindering and some promoting solvent reorganization ability. Both traces are normalized to 1.0 for clarity.

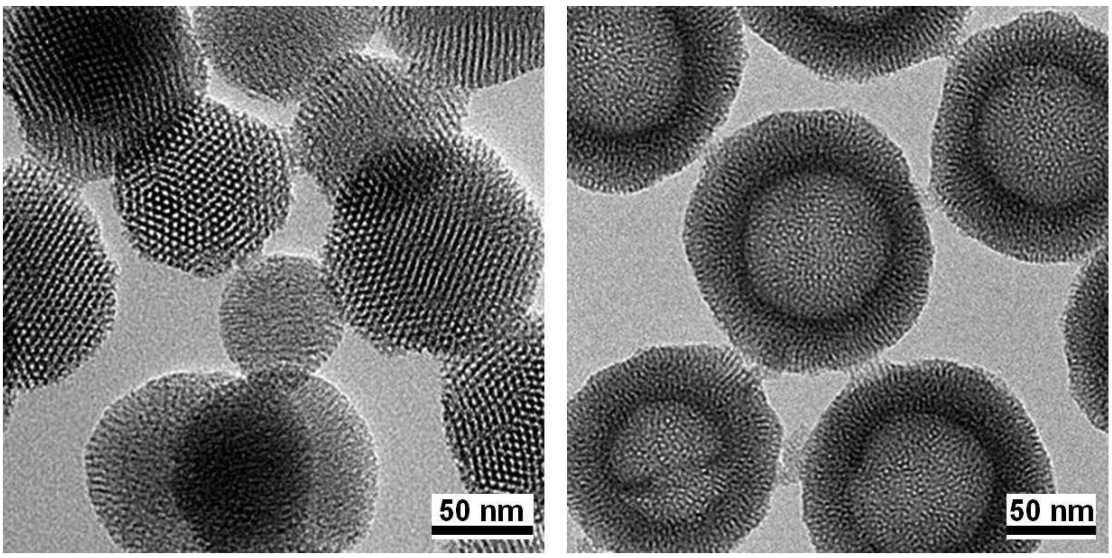


**Figure 3.8.** Transmission electron microscope images of MCM-41 nanoparticles (left) and hollow-core MCM-41 nanoparticles (right) used in this study. The hexagonal pore structure is clearly seen in the TEM image on the left. MCM-41 and other mesoporous silica-based structures are popular due to their versatility, robustness, and non-toxicity.

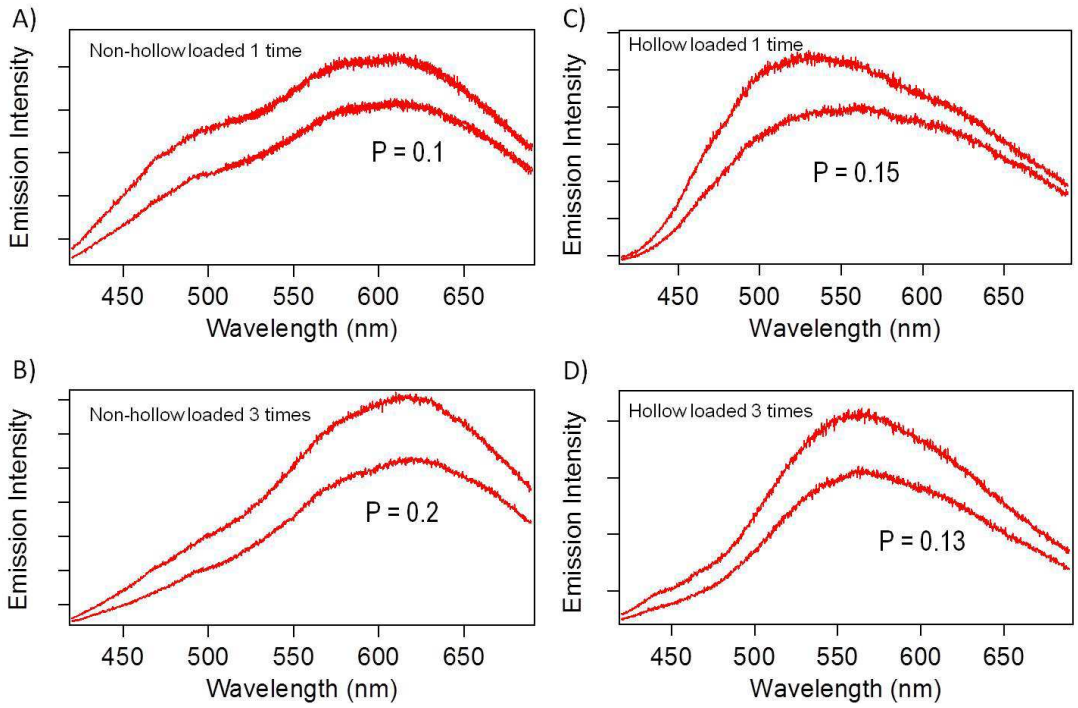


**Figure 3.9.** Comparison of rigidochromic spectra of non-hollow and hollow particles using different loading procedures. A) Non-hollow MCM-41 particles loaded 1 time; B) Non-hollow MCM-41 particles loaded 3 times; C) Hollow particles loaded 1 time; D) Hollow particles loaded 3 times.

**Table 3.1.** The $r_0$, $\tau_F$ and $\tau_c$ values for five samples with the (sodium bathocuproine disulfonate)$Re(CO)_3Cl$ dye.

| | Initial anisotropy $r_0$ | Fluorescence lifetime $\tau_F$ (μs) | Rotational correlation time $\tau_c$ (μs) |
|---|---|---|---|
| Solid-state dye | 0.28 ± 0.02 | 0.51 ± 0.03 | 2.30 ± 0.05 |
| Solution dye | 0.010 ± 0.001 | 0.99 ± 0.01 | 0.105 ± 0.001 |
| Dry particle | 0.39 ± 0.01 | 1.6 ± 0.1<br>0.44 ± 0.02 | 3.43 ± 0.09 |
| Particle in toluene | 0.19 ± 0.01 | 3.3 ± 0.7<br>0.93 ± 0.04 | 1.11 ± 0.04 |
| Particle in water | 0.04 ± 0.01 | 1.21 ± 0.08<br>0.20 ± 0.01 | 0.09 ± 0.05<br>2.1 ± 0.4 |

## 3.7. References


1. Dunn, B.; Zink, J. I., *Chemistry of Materials* **1997,** 9, (11), 2280-2291.
2. Kunkely, H.; Vogler, A., *Materials Chemistry and Physics* **2008,** 109, (2-3), 506-509.
3. Lu, J.; Liong, M.; Li, Z.; Zink, J. I.; Tamanoi, F., *Small* **2010,** 6, (16), 1794-1805.
4. Du, L.; Liao, S.; Khatib, H. A.; Stoddart, J. F.; Zink, J. I., *Journal of the American Chemical Society* **2009,** 131, (42), 15136-15142.
5. Shapiro, A. B.; Fox, K.; Lam, P.; Ling, V., *European Journal of Biochemistry* **1999,** 259, (3), 841-850.
6. Petersen, T. W.; Ibrahim, S. F.; Diercks, A. H.; van den Engh, G., *Cytometry Part A* **2004,** 60A, (2), 173-181.
7. Tawar, U.; Jain, A. K.; Chandra, R.; Singh, Y.; Dwarakanath, B. S.; Chaudhury, N. K.; Good, L.; Tandon, V., *Biochemistry* **2003,** 42, (45), 13339-13346.
8. Schaefer, B. E., *Science* **1996,** 272, (5268), 1595-1595.
9. Demchenko, A. P., Introduction to Fluorescence Sensing. In *Introduction to Fluorescence Sensing*, 2009.
10. Du, H.; Fuh, R. C. A.; Li, J. Z.; Corkan, L. A.; Lindsey, J. S., *Photochemistry and Photobiology* **1998,** 68, (2), 141-142.
11. Li, Z.; Nyalosaso, J. L.; Hwang, A. A.; Ferris, D. P.; Yang, S.; Derrien, G.; Charnay, C.; Durand, J.-O.; Zink, J. I., *The Journal of Physical Chemistry C* **2011,** 115, (40), 19496-19506.

12. Franville, A.-C.; Dunn, B.; Zink, J. I., *The Journal of Physical Chemistry B* **2001,** 105, (42), 10335-10339.

13. Charnay, C.; Bégu, S.; Tourné-Péteilh, C.; Nicole, L.; Lerner, D. A.; Devoisselle, J. M., *European Journal of Pharmaceutics and Biopharmaceutics* **2004,** 57, (3), 533-540.

14. Vialpando, M.; Martens, J. A.; Van den Mooter, G., *Therapeutic Delivery* **2011,** 2, (8), 1079-1091.

Part II

# Organic Functionalization of Mesoporous Silica Nanoparticles for Applications as Controlled Release Vehicles

# Chapter 4

# pH-Operated Nanopistons on the Surfaces of MSNs

## 4.1. Abstract

The development of drug delivery systems for the targeted and on-demand release of pharmaceutical products has risen rapidly to become a contemporary challenge in the field of nanobiotechnology. Biocompatible mechanized phosphonate-clothed silica nanoparticles have been designed and fabricated in which the supramolecular machinery, which covers the surfaces of the nanoparticles, behaves like nanopistons, releasing encapsulated guest molecules in a controlled fashion under acidic conditions. The mechanized nanoparticles consist of a monolayer of β-cyclodextrin rings positioned selectively around the orifices of the nanopores of the mesoporous nanoparticles. A Rhodamine B / benzidine conjugate has been prepared and serves as the nanopistons for movement in and out of the cylindrical cavities provided by the β-cyclodextrin rings on the surfaces of the nanoparticles. Luminescence experiments indicate that the mechanized nanoparticles are able to store small cargo molecules – e.g., 2,6-naphthalenedisulfonic acid disodium – within their nanopores at neutral pH and then release them as a result of passage through the cavities of the β-cyclodextrin rings as soon as the pH is lowered to ~ 5. In further investigations, the phosphonate-covered silica nanoparticles were functionalized selectively with the β-cyclodextrin rings, but, on this occasion, the seven linkers attaching the rings to the orifices surrounding the nanopores contain cleavage imine double bonds. The β-cyclodextrin rings on the surface of the nanoparticles serve as gates for the storage of large cargo molecules, such as Rhodamine B, inside the nanopores of the nanoparticles under neutral conditions. Since imine bonds can be hydrolyzed under acidic conditions, the β-cyclodextrin rings can be severed from the

surface of the nanoparticles when pH is decreased to 6, releasing the large cargo molecules. The results described here present a significant step towards the development of pH-responsive nanoparticle-based dual drug delivery vehicles that are potentially capable of being interfaced with biological systems. The author acknowledges Dr. Yanli Zhao for his help on the organic synthesis described in this chapter.

## 4.2. Introduction

In this chapter, we employed phosphonate-covered silica nanoparticles to prepare MSNs in which $\beta$-CD rings are immobilized selectively around the orifices of the nanopores of the nanoparticles and the gates are nanopistons which can be induced to move in or out of the cylindrical cavities provided by the $\beta$-CD rings.

The phosphonate-covered silica nanoparticles were prepared from tetraethyl orthosilicate (TEOS) and 3-(trihydroxysilyl)propyl methylphosphonate monosodium (TPMP) by a surfactant-directed self-assembly process,[1] whereby the surfaces of the nanoparticles are covered fully with propyl methylphosphonate units. After the surfactant – cetyltrimethylammonium bromide (CTMA) – has been removed from the nanopores of the nanoparticles under acidic conditions, the orifices around entrances to the nanopores are exposed for further functionalization. This synthetic strategy has made it possible for us to functionalize, only and specifically, the exposed areas – namely, the orifices surrounding the entrances to the nanopores in order to align the nanopores, the $\beta$-CD rings, and the nanopistons in a co-linear manner. The fabrication process ensures that the $\beta$-CD rings are only located at the orifices of the nanopores on the surface of the nanoparticles. A schematic representation of this next generation of MSNs is shown in

Figure 4.1. Their design is fashioned according to the following blueprint: $\beta$-CD rings persubstituted on their 6-positions with kinetically stable linkers, serve as the monocylinders which are linked covalently around the orifices of the nanopores of the phosphonate-covered silica nanoparticles. Rhodamine B / benzidine conjugates fulfill the role of the nanopistons, which have been designed to move in and out of the nanosylinders provided by the cavities of the $\beta$-CD rings[2, 3] in response to changes in pH to ~ 5 (Figure 4.2). In addition, 2,6-naphthalenedisulfonic acid disodium (NDAD) has been employed as the cargo inside the nanopores. Since both Rhodamine B and the NDAD cargo have characteristic fluorescent properties, we can monitor the operation of the nanopistons by following the changes in their luminescent properties.

## 4.3. Results and Discussion

The size and shape of the phosphonate silica nanoparticles **2** were evaluated (Figure 4.3) using TEM. The nanoparticles are roughly spherical in shape and around 100 nm in diameter. They possess perfect hexagonal nanopore arrays with an average nanopore diameter of 2 nm. The nanoparticles also show typical XRD patterns of the MCM-41-type hexagonal mesoporous silica.[4] An interplanar spacing ($d_{100}$) of about 3.8 nm was calculated from these patterns. After the nanoparticles have been functionalized with the β-CD rings, the shape of the nanoparticles, it appears, had experienced no obvious changes, at least as judged by TEM and XRD, indicating that the β-CD-capped MSNs retain the characteristic of mesoporous silica nanoparticles.

CP/MAS Solid-state NMR experiments provide direct evidence for the formation of the β-CD capped nanoparticles. On examination of the $^{13}$C CP/MAS solid-state NMR

spectrum (Figure 4.4a) of the capped nanoparticles **6**, (i) the signals resonating around 22 ppm can be attributed to the characteristic peaks of aliphatic carbons *l* and *m* on the linker between the β-CD ring and the phosphonate silica nanoparticle, (ii) the signals resonating around 45 ppm can be assigned to the characteristic peaks of the carbons *a*, *b*, *c*, *h*, *i*, and *k* on the linker, (iii) the signals resonating around 50, 73, 84, and 104 ppm can be attributed to the characteristic carbon peaks of $C_6$, $C_{2/3/5}$, $C_4$, and $C_1$ on the β-CD skeleton,[5] (iv) the signals resonating around 130 ppm can be assigned to the characteristic peaks of the aromatic carbons *d*, *e*, and *f* on the phenyl groups, and (v) the signals resonating around 165 ppm can be attributed to the characteristic peaks of the carbons *g* and *j*. From an examination of the $^{13}C$ CP/MAS solid-state NMR spectrum (Figure 4.4b) of the nanoparticles **2**, we know that the carbon nuclei of the TPMP units also contribute to the signals resonating around 9, 22, and 65 ppm. The $^{29}Si$ CP/MAS solid-state NMR spectrum (Figure 4.4) of the nanoparticles 6 shows two silicon peaks around −60 and −105 ppm, corresponding10 to the functionalized silica (T region) and bulk silica (Q region), respectively. Although the silicon nuclei in the nanoparticles 2 also give rise to two peaks which are attributed to the phosphonate silica (T region) and bulk silica (Q region), the peak around −60 ppm in the phosphonate-covered silica nanoparticles 2 is of relatively low intensity compared with that observed for the capped nanoparticles 6.

On the basis of the large $K_f$ value ($8605 \pm 85\ M^{-1}$) for the complex between the *β*-CD ring and the plug, the extent to which the plugs occupy the *β*-CD heptapuses on the nanoparticles under neutral conditions could be estimated. Despite the fact that the plugs bind with the *β*-CD rings on the surfaces of the mechanized nanoparticles at the interface

of the aqueous solution and the $\beta$-CD monolayer, we assumed that the sites of host-guest binding between the plugs and the $\beta$-CD rings are equivalent and independent.[6-9] Thus, the formation constant for complexation of the plug to a single $\beta$-CD ring on the surface of a mechanized nanoparticle at the interface was assumed to be comparable to the $K_f$ value for this host-guest pair in aqueous solution. In the particular procedure for the preparation of the silica nanoparticle-based nanopistons, the initial concentrations of the $\beta$-CD rings and the plugs were calculated to be $2.46 \times 10^{-5}$ and $2.0 \times 10^{-3}$ M, respectively; from these, we computed the concentration of the complex formed in this reaction.

The calculations assume that the phosphonate-covered silica nanoparticles are fully attached to the $\beta$-CD heptapuses with one $\beta$-CD ring position as an extension over each nanopore (somewhat like a porch outside the front door of a house). During the preparation of the silica nanoparticle-based nanopistons (see the Experimental Section), 50 mg of the phosphonate-covered silica nanoparticles and a solution volume of 10 mL were used. Thus, the concentration of the $\beta$-CD ring is $[\beta\text{-CD}]_0$ ) $2.46 \times 10^{-5}$ M [(total weight of the nanoparticle/weight of individual nanoparticle/Avogadro constant) × (number of $\beta$-CD rings on one nanoparticle)/(volume of solution) ) = [(0.05 g)/($7.62 \times 10^{-16}$ g)/($6.02 \times 1023$ $mol^{-1}$) × (2260)/(0.01 L)], and the concentration of the plug is $[plug]_0$ ) $2.0 \times 10^{-3}$ M (0.02 mmol/0.01 L). For the complex of a $\beta$-CD ring with a plug, $K_f$ is defined as

$$K_f = \frac{[complex]_{eq}}{[plug]_{eq}[\beta - CD]_{eq}}$$

where "eq" subscripts denote equilibrium concentrations. Using the measured $K_f$ value ($8605 \pm 85\ M^{-1}$) in this equation gives

$$8605\ M^{-1} = \frac{[complex]_{eq}}{[plug]_{eq}[\beta - CD]_{eq}}$$

$$= \frac{[complex]_{eq}}{([plug]_0 - [complex]_{eq}) \times ([\beta - CD]_0 - [complex]_{eq})}$$

$$= \frac{[complex]_{eq}}{(2.0 \times 10^{-3} M - [complex]_{eq}) \times (2.46 \times 10^{-5} M - [complex]_{eq})}$$

which can be solved to obtain a concentration of $2.32 \times 10^{-5}$ M for the complex. Therefore, the percentage of plugs filling the $\beta$-CD heptapuses on the nanoparticles at the concentrations in question was $100\% \times (2.32 \times 10^{-5}\ M)/(2.46 \times 10^{-5}\ M) ) = 94\%$. In view of this high coverage, it is hardly surprising that the silica nanoparticle-based nanopistons do not exhibit any serious leakage under neutral conditions.

The operation of the mechanized silica nanoparticle-based nanopistons **1** was monitored in aqueous solution by fluorescence spectroscopy. A sample of the NDAD-loaded nanoparticles (5 mg) was placed in the corner of a cuvette, and distilled $H_2O$ (5 mL, pH 7) was added very carefully to the cuvette so as not to disturb the nanoparticles. A laser probe beam directed into the solution was used to excite the released cargo molecules. The emission intensities of these molecules were collected as a function of time and used to generate a release profile. The pH of the solution was adjusted to the desired value by the addition of HCl solution (0.1 M). The percentage of the cargo released was calculated using absorbance spectroscopy to enable quantitative comparison of the release efficiency. Since there are two fluorescent units – the Rhodamine B unit on

**7** and the NDAD cargo – in the system based on pH-operating release, we monitored the release profiles of the nanoparticles using two laser sources, one laser source operating at 448 nm was used to monitor the Rhodamine B unit and the other laser source at 377 nm was used to monitor the NDAD cargo. Figures 4.5a and 4.5b show the release profiles of Rhodamine B unit and NDAD cargo from the mechanized silica nanoparticle-based nanopistons **1**, respectively. The flat baselines (black curves) indicate that both Rhodamine B unit and NDAD cargo do not leak from the mechanized silica nanoparticle-based nanopistons **1** under neutral conditions. The emission intensity of the solution before any pH-triggered release was monitored for over 40 minutes. The pH value of the system was then decreased from 7 to 4 by the addition of 0.1 M HCl. As the protonated plug **7** leaves the cavity of the β-CD ring on the nanoparticles, the NDAD cargo is released from the nanopores of the nanoparticles and we monitor the fluorescence changes of the solution in order to evaluate the cargo storage and release abilities of the mechanized nanoparticles in response to the pH changes. After the pH is lowered, the emission intensities of both the Rhodamine B unit and the NDAD cargo in solution increased immediately, confirming that the positively charged plug **7** is no longer blocking the β-CD ring on the nanopores of the nanoparticle and, in turn, the NDAD cargo in the nanopores is released into the solution. In a control experiment, the NDAD-loaded nanoparticles **6** without plug **7** showed a sustained release profile when the loaded nanoparticles were not washed. However, when the NDAD-loaded nanoparticles were washed thoroughly, there was no fluorescent change even after lowering the pH value of the solution. The reason for the difference lies in the fact that the NDAD cargo molecules

had escaped through the unblocked β-CD rings on the nanopores of the nanoparticles during the washing process.

## 4.4. Conclusions

On the basis of the tenets of supramolecular chemistry[11] and mechanostereochemistry,[12] we have described the nanoscale fabrication and pH-responsive operation of phosphonate-covered mesoporous silica nanoparticle-based nanopistons. β-CD rings were attached covalently with structural precision around the orifices of the nanopores of these protected nanoparticles, creating an inorganic–organic material that constitutes an integrated system. The introduction of the β-CD rings around the orifices of the nanopores on the spherical surfaces of the nanoparticles affords much greater stereoelectronic control over the entrapment and release of small-molecule cargos than we have achieved previously in our design and fabrication of mechanized silica nanoparticles. The next generation of this particular class of nanoparticles allows for much more delicately controlled monolayers of nanopistons covering their surfaces. The β-CD rings not only constitute a chemical modification of mechanized mesoporous silica nanoparticles but also impose stereoelectronic control upon the orifices of the nanopores at the surfaces of the nanoparticles. As far as the nanopistons on the surfaces of the mechanized silica nanoparticles are concerned, the rhodamine B/benzidine plug can slide in and out of the cylindrical cavities provided by the β-CD rings on the surfaces of the nanoparticles in order to control the trapping and release of the cargo molecules in response to pH changes. A few carefully chosen spectroscopic techniques have demonstrated that the nanopistons are able to incorporate cargo molecules inside the

nanopores of the nanoparticles under neutral pH conditions but release them when the pH is lowered just a little. Fluorescent molecules were chosen as the cargos in order to establish a proof-of-principle operation of nanopistonoperated mesoporous silica nanoparticles.

## 4.5. Experimental

The phosphonate-covered silica nanoparticles **2** were prepared using an approach similar to that described in literature.[1] Cetyltrimethylammonium bromide (0.50 g, 1.4 mmol) was dissolved in a mixture of distilled $H_2O$ (240 mL) and 2 M NaOH (1.75 mL), and the solution was stirred under an atmosphere of $N_2$ and heated up to 80 °C. Tetraethylorthosilicate (2.5 mL, 2.33 g, 11.2 mmol) was then added to the solution. After 15 min, 3-(trihydroxysilyl)propylmethylphosphonate monosodium (0.65 mL, 0.81 g, 3.4 mmol) was slowly added to the mixture solution. After the solution was stirred at 80 °C for 2 h, it was cooled down to room temperature and the nanoparticles which formed were filtered, washed with MeOH and $H_2O$, and dried at room temperature overnight. In order to remove the surfactant from the nanopores of the nanoparticles, they were suspended in a mixture of MeOH (50 mL) and concentrated HCl (3 mL) and the solution was heated under reflux for 24 h. The nanoparticles **2** were then filtered and washed thoroughly. The product was dried under vacuum prior to its characterization by solid-state NMR spectroscopy, transmission electron microscope (TEM), and powder X-ray diffraction (XRD). $^{13}$C CP/MAS solid-state NMR (300 MHz): 65, 22, 9 ppm.

The isocyanato-functionalized nanoparticles **3** were prepared using an approach modified from one published in the literature.[10] The phosphonate-covered silica

nanoparticles **2** (100 mg) were suspended in anhydrous PhMe (15 mL) and 3-isocyanatopropyltriethoxysilane (50 μL, 0.05 g, 0.2 mmol) was added to the solution. The reaction mixture was stirred at room temperature under an atmosphere of $N_2$ overnight. The isocyanato-functionalized nanoparticles **3** were isolated by centrifugation, washed by PhMe and MeOH, and dried under vacuum.

The isocyanato-functionalized nanoparticles **3** (50 mg) were suspended in anhydrous PhMe (15 mL) and 4-(2-hydroxyethoxy)benzaldehyde (0.02 g, 0.15 mmol) was then added to the solution. The reaction mixture was stirred under reflux in an atmosphere of $N_2$ overnight. The formyl-functionalized nanoparticles **4** were obtained by centrifugation, washed by PhMe and MeOH, and dried under vacuum.

The formyl-functionalized nanoparticles **4** (50 mg) and anhydrous $MgSO_4$ (0.02 g, 0.2 mmol) were suspended in anhydrous *N*,*N*-dimethylformamide (20 mL) and diamino-β-CD derivative **5** (0.03 g, 0.02 mmol) was then added to the solution. While the solution mixture was being stirred at room temperature in an atmosphere of $N_2$ for 6 h, $NaBH_4$ (0.01 g, 0.25 mmol) was added to it slowly at 0 °C. After the solution had been stirred for 2 h at 0 °C, the reaction was quenched with $H_2O$ at room temperature. The β-CD-capped nanoparticles **6** were isolated by centrifugation, washed by $H_2O$, and dried under vacuum. $^{13}C$ CP/MAS solid-state NMR (300 MHz): 165, 130, 104, 84, 73, 50, 45, 22, 9 ppm. $^{29}Si$ CP/MAS solid-state NMR (300 MHz): −60, −105 ppm.

The β-CD-capped nanoparticles **6** (50 mg) were added to an aqueous buffer solution (pH 7) containing 2,6-naphthalenedisulfonic acid disodium (10 mL, 1.0 mM). The reaction mixture was stirred and sonicated to maximize the dispersion. The solution

was then stirred under an atmosphere of $N_2$ overnight to allow 2,6-naphthalenedisulfonic acid disodium to diffuse into the nanopores of the nanoparticles. The plug **7** (0.02 g, 0.02 mmol) was then added to the reaction mixture. After the solution had been stirred under an atmosphere of $N_2$ for 4 h, the mechanized silica nanoparticle-based nanopistons **1** were obtained by centrifugation, washed by aqueous buffer solution, and dried under vacuum. The fresh nanoparticles were used immediately for the laser investigation involving fluorescence spectroscopy and release profiles.

Cargo-loaded nanoparticles were examined employing a spectroscopic set-up. The nanoparticles (5 mg) were placed in the corner of a cuvette. Distilled $H_2O$ (pH ~7, 5 mL) was added to the cuvette in a dropwise fashion in order to prevent the nanoparticles from dispersing into the solution. A 1 mm stirring bar was added to the cuvette. The solution in the cuvette was stirred slowly so as not to perturb the nanoparticles. The solution was monitored by a CCD, which collects the emission spectra of the solution. A laser probe beam directed into the solution ca. 2 cm above the bottom of the cuvette was used to excite the released cargo molecules. A suitable filter lens was mounted in front of the CCD detector to remove the scattered probe beam. The fluorescence spectra of the released cargo molecules were collected in one-second intervals during the course of the experiment. The fluorescence intensity at the emission maximum of the cargo molecules was plotted as a function of time in order to generate a release profile. Activation of releasing the cargo molecules from the nanoparticles was accomplished by adjusting the pH values of the solution with addition of HCl solution (0.1 M). The percentage of the

cargo release was calculated using UV-Vis absorption spectroscopy, thus enabling quantitative comparison of the release efficiency.

## 4.6. Figures and Tables

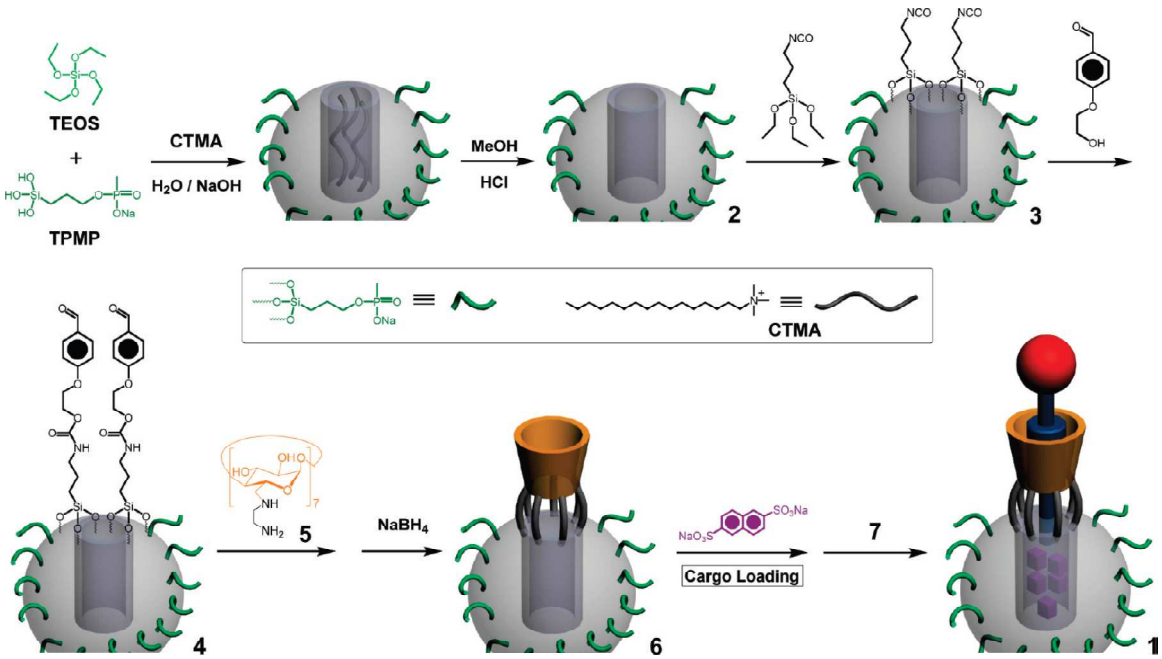


**Figure 4.1.** Synthetic procedure for the mechanized silica nanoparticle-based nanopistons **1.**

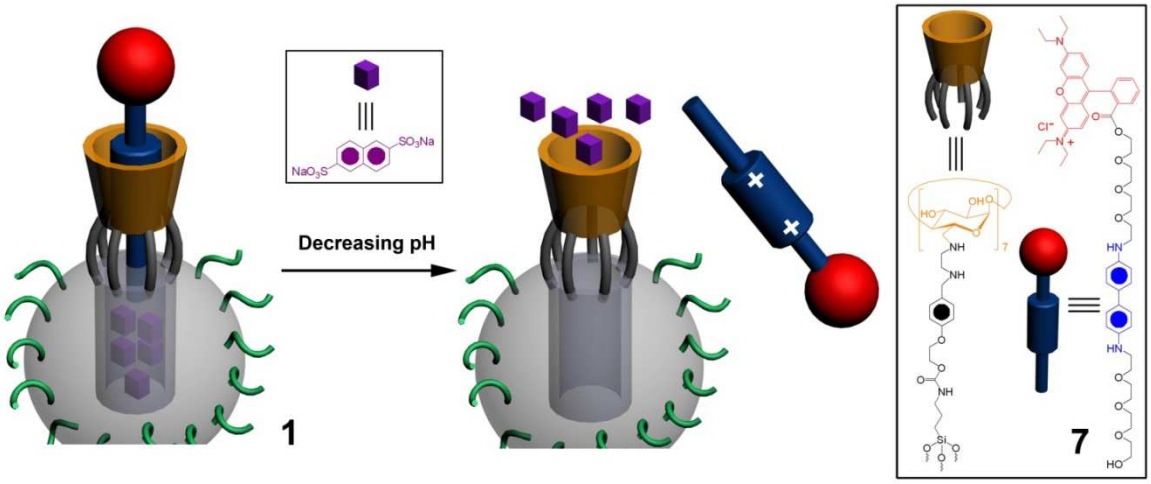


**Figure 4.2.** Schematic representation of nanopistons on mechanized phosphonate-covered silica nanoparticles. According to the size match of the nanopore and the $\beta$-CD ring, the ideal mode is that one nanopore is functionalized with one $\beta$-CD ring as shown in the figure.

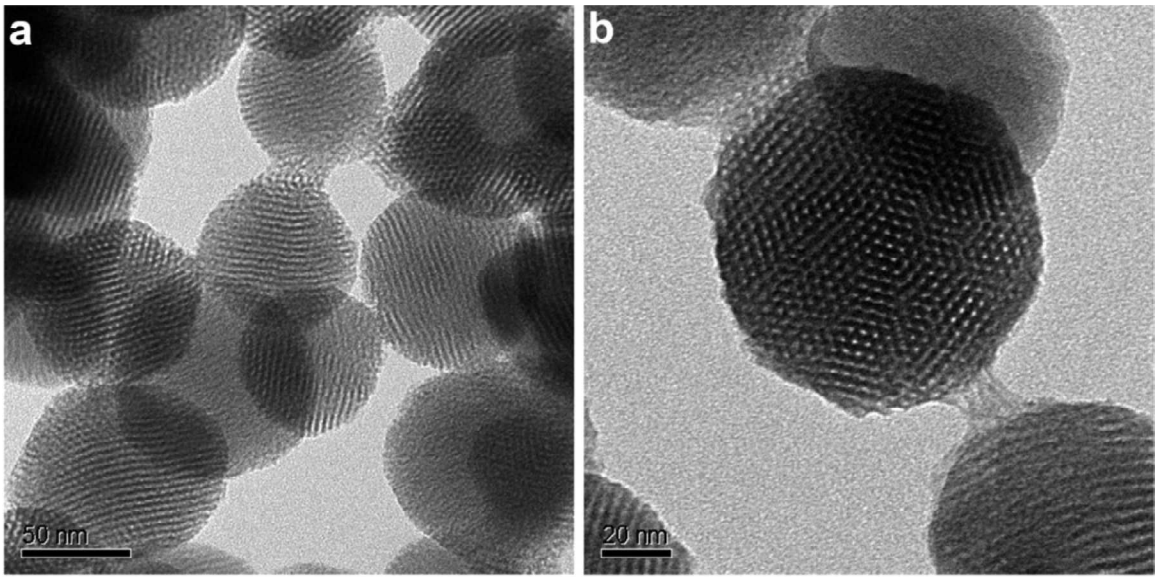


**Figure 4.3.** TEM images of the phosphonate-covered silica nanoparticles **2** at (a) low and (b) high resolution.

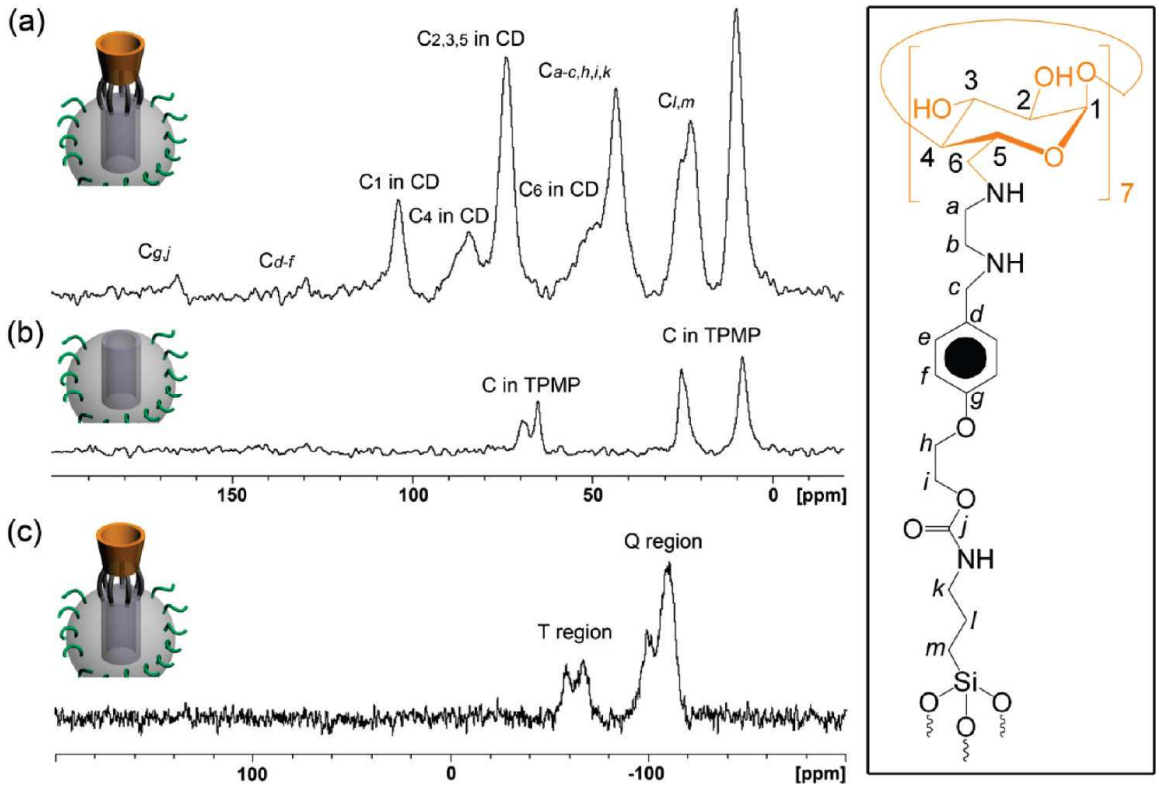


**Figure 4.4.** $^{13}C$ and $^{29}Si$ CP-MAS solid-state NMR spectra. (a) 13C CP-MAS solid-state NMR spectrum of the $\beta$-CD-capped nanoparticles **6**. (b) 13C CP-MAS solid-state NMR spectrum of the phosphonate-covered silica nanoparticles **2**. (c) 29Si CP-MAS solid-state NMR spectrum of the capped nanoparticles **6**. The carbon nuclei of the $\beta$-CD ring and the linker are defined alongside the structural formula.

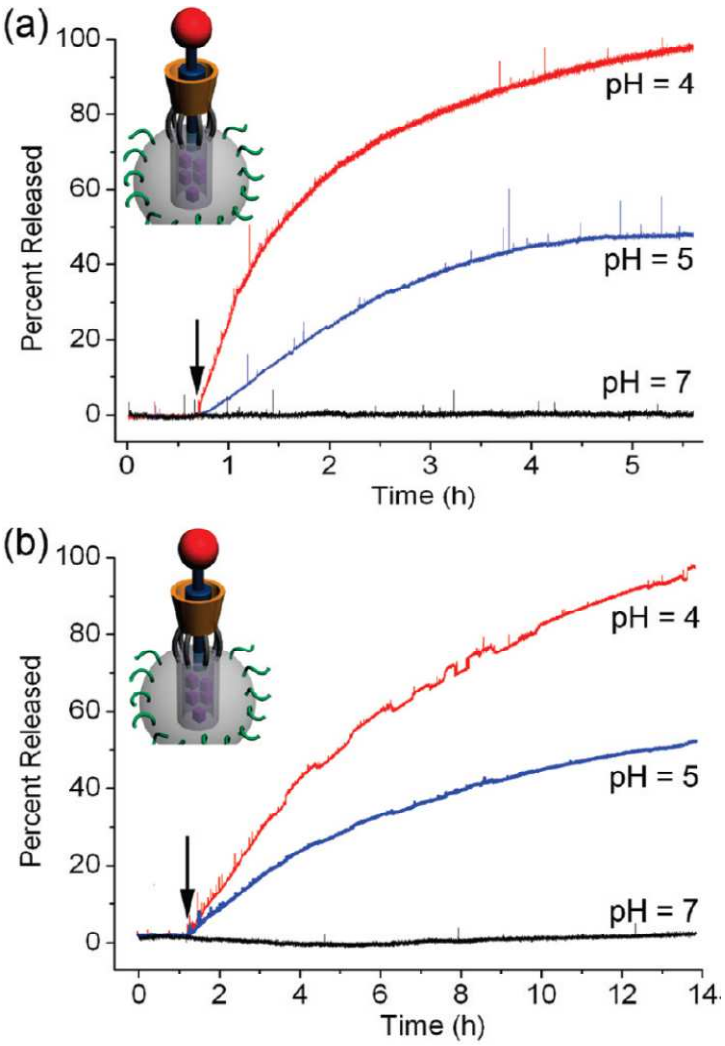


**Figure 4.5.** Release profiles of the mechanized nanoparticles under pH control. (a) Release profile of the mechanized silica nanoparticle-based nanopistons **1** while monitoring the emission (565 nm) of the Rhodamine B unit on the plug **7**. (b) Release profile of the mechanized silica nanoparticle-based nanopistons **1** while monitoring the NDAD cargo emission at 415 nm. (c) Release profile of the mechanized nanoparticles **8** while monitoring the Rhodamine B cargo emission at 565 nm.

## 4.7. References


1. Lu, J.; Liong, M.; Zink, J. I.; Tamanoi, F. *Small* **2007**, *3*, 1341-1346.
2. Tian, H.; Wang, Q.-C. *Chem. Soc. Re*v. **2006**, *35*, 361-374.
3. Frampton, M. J.; Anderson, H. L. *Angew. Chem., Int. Ed.* **2007**, *46*, 1028-1064.
4. Kresge, C. T.; Leonovicz, M. E.; Roth, W. J.; Vartuli, J. C.; Beck, J. S. *Nature* **1992**, *359*, 710–712.
5. Gidley, M. J.; Bociek, S. M. *J. Am. Chem. Soc.* **1988**, *110*, 3820-3829.
6. Mulder, A.; Auletta, T.; Sartori, A.; Ciotto, S. D.; Casnati, A.; Ungaro, R.; Huskens, J.; Reinhoudt, D. N. *J. Am. Chem. Soc.* **2004**,*126*, 6627-6636.
7. Corbellini, F.; Mulder, A.; Sartori, A.; Ludden, M. J. W.; Casnati, A.; Ungaro, R.; Huskens, J.; Crego-Calama, M.; Reinhoudt, D. N. *J. Am. Chem. Soc.* **2004**, *126*, 17050-17058.
8. Crespo-Biel, O.; Lim, C. W.; Ravoo, B. J.; Reinhoudt, D. N.; Huskens, J. *J. Am. Chem. Soc.* **2006**, *128*, 17024-17032.
9. Ludden, M. J. W.; Li, X.; Greve, J.; van Amerongen, A.; Escalante, M.; Subramaniam, V.; Reinhoudt, D. N.; Huskens, J. *J. Am. Chem. Soc.* **2008**, *130*, 6964-6973.
10. Nguyen, T. D.; Tseng, H.-R.; Celestre, P. C.; Flood, A. H.; Liu, Y.; Stoddart, J. F.; Zink, J. I. *Proc. Natl. Acad. Sci. U.S.A.* **2005**, *102*, 10029-10034.
11. Stoddart, J. F. *Nat. Chem.* **2009**, *1*, 14–15.
12. Olson, M. A.; Botros, Y. Y.; Stoddart, J. F. *Pure Appl. Chem.* **2010**, *82*, 1569–1574.

Chapter 5

# Controlled Release of Two Cargos in Succession from MSNs

## 5.1. Abstract

The goal of drug delivery systems is to deploy drugs to a specifically targeted part of body, and then control the therapy administration by means of either a physiological or chemical trigger. In order to administer therapeutic combinations and produce synergistic action, well-organized multidrug release systems which can control the administration order, timing and dosing of each individual drug, must be established. In this chapter, we describe an on-command dual cargo release system based on $\beta$-cyclodextrin ($\beta$-CD) modified mesoporous silica nanoparticles (MSNs), in which two differently-sized cargos were loaded into MSNs step-by-step and then released step-by-step after the release mechanisms were triggered by different stimuli. As a proof of concept, we first released the small cargo (e.g., coumaric acid) by lowering the pH and expelling a methyl orange plug from $\beta$-CD, and then release the large cargo (e.g., Hoechst 33342) after cleavage of disulfide bonds. The results reported here represent a significant step toward the development of programmed multidrug delivery systems and may potentially be used to deliver different drugs for combination therapy in the future. The organic synthesis of the machine components described in this chapter was performed by Dr. Cheng Wang in the Stoddart group at Northwestern Univeristy.

## 5.2. Introduction

Combination drug therapy,[1] a regimen in which multiple drugs with different therapeutic outcomes are used in parallel or in sequence, has become the dominant strategy in the clinical treatment of HIV/AIDS,[2] diabetes,[3] and cancer,[4] For example, in cancer therapy, the U.S. Food and Drug Administration (FDA) approved the use of

Avastin in combination with Carboplatin and Paclitaxel for the initial systemic treatment of patients with lung cancer in 2006. Unlike monotherapy, combination therapy maximizes therapeutic efficacy against individual targets and is more likely to overcome mechanisms behind drug resistance. Such combination therapy also has the potential to increase the odds of a positive prognosis and reduce harmful side effects.

On account of the shifting interests of the pharmaceutical industry, researchers have moved away from the development of new drug candidates toward new ways to deliver well-known drugs. Drug delivery systems, which can administer[5] medically active molecules to diseased cells in a targeted and controlled manner, have gained much attention in the past couple of decades. Polymers,[6] dendrimers,[7] micelles,[8] vesicles[9] and nanoparticles[10] have all been investigated for their use as possible drug delivery systems. Most of the so-far developed drug delivery systems provide either delivery of a single drug or simultaneous delivery[11] of multiple drugs. It is difficult, however, with these systems to control[12] the administration order, timing and dose of each individual drug in a comprehensive way. While it is possible to deliver the cocktail of drugs using several different co-administered drug delivery systems, this approach comes with disadvantages. For example, it is extremely difficult to expose several co-administered drug delivery systems to the same target at the right time, and also difficult to control the dosage rates and ratios of each individual drug. In order to administer chemotherapeutic combinations and produce synergistic actions, a well-organized multidrug release system which can provide combination therapy by controlling the release behavior of each drug individually needs to be invented.

Mesoporous silica nanoparticles (MSNs) have attracted[13] widespread research interest in the past decade for use in functional materials. They have large surface exteriors and porous interiors that can be harnessed as reservoirs for small molecule drug storage. It has also been demonstrated[14] that MSNs are nontoxic to cells and can undergo cellular uptake into acidic lysosomes by endocytosis when they are 100~200 nm in diameter, making them a popular candidate[15] for drug delivery systems. In particular, MSNs can be functionalized with molecular, as well as supramolecular, switches that control the release of internal cargo/drug molecules in response to external stimuli. On-command release systems which respond to a range of stimuli, including pH changes,[16] light-initiation,[17] competitive binding,[18] redox activation,[19] biological triggers[20] and temperature-controlled release,[21] have been reported by us and others. To the best of our knowledge, however, all the on-command release systems reported thus far cannot release multiple drugs step-by-step.

Cyclodextrins (CDs), especially because of their capability to form[22] inclusion complexes with guest molecules that dissociate in the face of the right external stimuli, have been a target of intensive research. $\beta$-Cyclodextrin ($\beta$-CD), which is comprised of seven D-glucopyranosyl units with top and bottom cavities of 6.0 and 6.5 Å, respectively, have been used[23] as gatekeepers in drug delivery systems. The functionalization of MSNs surface with $\beta$-CD rings provides us with a way to establish a dual cargo release system. The $\beta$-CD rings on the surface of the nanoparticles can serve as a gate for the storage of large cargo molecules (>6.0 Å). Since the nanopores are not fully occupied by large cargo molecules there issome space for small cargo molecules (<6.0 Å) to diffuse into the

nanopores through the middle of the *β*-CD cavity, which are sealed inside after the formation of a complex between *β*-CD and a plug. Moreover, the nanoparticles will first of all release the small cargo molecules when the plugs are removed from the cavities of the *β*-CD rings; then, the large cargo molecules will be released after cleaving the *β*-CD rings from the surface of the nanoparticles.

In this chapter, an on-command dual cargo release system based on *β*-CD modified MSNs is described, in which two differently-sized cargos are loaded into MSNs **1** in sequence and then released in succession, by first of all, lowering the pH and then by adding a reducing agent as described schematically in Figure 5.1. The *β*-CD rings, persubstituted on their seven C6 positions and the seven linkers covalently connected to the surface via disulfide units, serve as the gatekeepers for the large cargo Hoechst 33342 molecules. The small cargo, *p*-coumaric acid (CA), is then diffused into the pore channels of the nanoparticles through the cavity of *β*-CD rings. The *β*-CD cavity is then capped by a plug, specifically methyl orange (MO), which was selected because it moves in and out of the cavities of the *β*-CD rings in response to changes in pH. The small cargo molecules are released after protonation of MO, and then, the large cargo molecules are released after cleavage of the disulfide bonds. Since both the Hoechst 33342 and CA cargos have characteristic fluorescent properties, the dual release process step-by-step can be monitored by tracking the changes in their emission spectra.

## 5.3. Results and Discussion

Hoechst 33342 and CA were chosen as the fluorescent cargos to trace the independent release process because, firstly, the size of Hoechst 33342 (~20 Å) and CA

(~4.5 Å) are optimal for them to act as the large and small cargos, respectively, and secondly, their fluorescent spectra are distinguishably different. The synthetic procedure for the preparation of MSNs **1** is shown in Figure 5.2. To engineer the dual-loaded system, the bare MCM-41 nanoparticles[24] were first functionalized with 3-isocyanatopropyltri-ethoxysilane, which were then reacted with propargyl ether **8** to offer the alkynyl-functionalized MSNs **2**. The FT-IR spectrum (see Supporting Information, SI) of MSNs **2** shows a peak at 2150 $cm^{-1}$, indicating the presence of C≡C bonds. The structure of the MSNs **2** was confirmed (see Figure 5.3) by transmission electron microscopy (TEM) to be hollow and consisting of pores with an average diameter of 2.5 nm. Following addition of per-6-azido-*β*-CD to the mixture of MSNs **2** and Hoechst 33342, the Hoechst 33342-loaded MSNs **3** was formed by means of a series of click reactions. CA was then allowed to diffuse through the cavities of the *β*-CD caps into the pores. After that, the *β*-CD openings were blocked with MO plugs thanks to host-guest interactions. The MSNs **1** loaded with both Hoechst 33342 and CA cargos inside could be obtained in a stepwise manner.

In order to gain insight on the fundamental mechanism of release in MSNs **1**, Hoechst 33342-loaded MSNs **3** were assembled in which the *β*-CD units were connected covalently onto the particle surface using disulfide units. The mechanism of operation of the Hoechst 33342-loaded MSNs **3** is shown in Figure 5.5a. After cleavage of the disulfide bonds by a reducing agent, the Hoechst 33342 cargo will be released. This mechanism is designed so that the release can be potentially triggered by glutathione from the cell cytosol,[25] and the system would thus operate autonomously within living

cells. The Hoechst 33342-loaded MSNs **3** were synthesized according to the approach outlined in Figure 5.2. After normal work-up, the nanoparticles were washed with acidic water (pH=3). It is worth emphasizing that it is very important to wash the nanoparticles with acidic water because the Hoechst 33342 dye can be adsorbed on the outer surface of the nanoparticles and also dissociated from the particle surface upon lowering the pH. Therefore, without an acidic wash, the Hoechst 33342 dye could come out after lowering the pH while operating the dual-loaded system MSNs **1**, interfering with the independent release processes.

The release of Hoechst 33342 from the MSNs **3** was monitored by a 351 nm probe beam to track the fluorescence intensity of the released dye as a function of time. A sample of MSNs **3** was placed in the corner of a cuvette and pH 7 water was slowly added into the cuvette without disturbing the particles. A flat baseline shows that the Hoechst 33342 molecules are held within the particles under neutral aqueous conditions, without any premature release. The pH of the solution was then lowered to 3.5 to confirm that negligible Hoechst 33342 is released singly by lowering the pH. After that, 2-mercaptoethanol (ME) was used as the reductant to cleave the disulfide bonds. Upon the addition of ME, the release of the Hoechst 33342 molecules was observed (Figure 5.6a) as a rapid increase of the fluorescence intensity around 500 nm as a function of time. The release of the Hoechst 33342 could not be detected prior to the addition of ME, an observation which indicates there was no detectable leakage and all the Hoechst 33342 was sealed inside the nanopores. Fluorescence intensity was used to calculate that 0.20

μmol of Hoechst 33342 was released from 5 mg of MSNs **3** after ~2 h, corresponding to a release capacity of 2.5 wt%.

In order to test whether the CA cargo can diffuse into the nanoparticles through the cavities of *β*-CD, a pH-operated system, MSNs **5**, was designed. A schematic representation of the operation of CA-loaded MSNs **5** is shown in Figure 5.5b. After lowering the pH, the protonated MO molecules move out from the cavities of *β*-CD, and the CA cargos will be released. There are three reasons for choosing MO as the piston to form a complex with *β*-CD. Firstly, the formation constant ($K_f$) for the complex[26] between *β*-CD and MO[27] is 4550 $M^{-1}$ at pH 7, which is much stronger than that (408 $M^{-1}$) of *β*-CD with CA. Secondly, the $K_f$ of *β*-CD with MO decreases[27] to 292 $M^{-1}$ at pH 2. This difference results in the release of cargo. These pH-responsive MSNs may potentially be interfaced with biological systems, because the lysosomal pH levels in cancer cells are somewhat lower[14c] than pH levels in healthy cells. Finally, the existence of the protonated MO does not interfere with the tracing of either Hoechst 33342 or CA.

The synthetic protocol for producing MSNs **5** is shown in Figure 5.2. After reaction of MSNs **2** and 6-azido-*β*-CD by means of a series of click reactions, the *β*-CD-capped MSNs **4** were isolated. MSNs **4** were characterized by TEM and $^{13}C$ and $^{29}Si$ cross-polarization magic-angle-spinning (CP-MAS) solid-state NMR spectroscopy (See Figure 5.4). The TEM (see Figure 5.3) results show that the shape of the nanoparticles experiences no obvious changes compared to bare MCM-41. The $^{13}C$ and $^{29}Si$ CP-MAS solid-state NMR experiment (see Figure 5.3) clearly shows the successful

functionalization of nanoparticles with $\beta$-CD rings. The MSNs **5** were finally obtained after the MSNs **4** were loaded with the CA cargo and then capped by the MO plug.

The operation of the MSNs **5** was followed by fluorescence spectroscopy (Figure 5.6b). A sample (5 mg) of CA-loaded MSNs **5** was placed in the corner of a cuvette and $H_2O$ (2 mL, pH 7) was added very carefully to the cuvette. An excitation beam of 351 nm was introduced to the solution above the nanoparticles, and the fluorescence intensity of the released CA in the solution was measured as a function of time. A flat baseline at pH 7 indicates that no CA could be released under neutral conditions. The pH of the solution was adjusted[28] to 3.5 by the addition of HCl solution (0.1 M). A rapid increase in the emission intensity around 425 nm shows that the CA cargo was released from the pores of the nanoparticles upon lowering the pH. UV-Vis absorption spectrophotometery was used to calculate the fact that ~0.52 μmol of the CA was released from 5 mg of MSNs **5**, corresponding to a release capacity of ~1.7 wt%. In a control experiment, we prepared CA-loaded nanoparticles without the MO plugs. They also showed a release after lowering the pH to 3.5 (see Figure 5.6b). Since CA shows affinity for $\beta$-CD, it can also be used as a plug to some extent. However, the release capacity corresponds to a maximum of ~0.14%, which is much lower than that of the CA-loaded MSNs **5**. The reason for this difference lies in the fact the CA shows much lower $K_f$ compared to MO with $\beta$-CD, an observation which means CA can escape more through the $\beta$-CD rings during the washing process for CA-loaded nanoparticles without MO plugs. Another CA-loaded nanoparticle was prepared and capped by a 1-adamantylamine plug. In this case, no fluorescence changes were observed even after lowering the pH to 3. This observation

can be explained by the strong $K_f$ between protonated 1-adamantylamine and $\beta$-CD (~$10^4$), [22a] which means that even protonated 1-adamantylamine will remain in the $\beta$-CD cavities, thus not allowing the small cargo to be released.

From all these individual systems, it is very clear that changing pH can induce the release of CA, whereas the release of Hoechst 33342 can only be triggered by the addition of ME, separately. The MSNs **1** (Figure 5.2) was synthesized by loading Hoechst 33342 and CA step-by-step. The dual release of cargo molecules from the dye-loaded MSNs **1** was monitored by fluorescence spectroscopy. A sample of MSNs **1** (5 mg) was placed in the corner of a cuvette, and $H_2O$ (2 mL, pH 7) was added very carefully to the cuvette. The CA cargo was released first after lowering the pH, an observation which was confirmed by the release profile (Figure 5.7a). The fluorescence spectra (Figure 5.7b) for the solution before and after CA release were dramatically different. According to the UV-Vis absorption measurements, ~0.13 μmol of the CA was calculated to be released, corresponding to a 0.42 wt% release capacity. After that, since the existence of the released CA in solution may interfere with the monitoring of the subsequent release process upon ME addition, we removed the solution above the nanoparticles and added fresh $H_2O$ into the cuvette carefully. Again a flat baseline showed that negligible Hoechst was released from the nanoparticles into pH 7 aqueous media. The release profile in Figure 5.7a indicates that the cargo Hoechst 33342 can only be released upon ME addition, and the calculated released amount of Hoechst 33342 was ~0.22 μmol. The fluorescence spectra are shown (Figure 5.7c) for the solution before and after the Hoechst 33342 release. These results have demonstrated very clearly the fact that MSNs **1** can

hold two cargos successfully and more importantly, release CA first, after decreasing the pH, and then Hoechst 33342, after addition of ME.

## 5.4. Conclusions

In summary, a dual cargo release system was established in which two different size cargos were loaded into MSNs and then released step-by-step triggered by two different stimuli. The functionalization of the MSNs surface with *β*-CD rings not only act as a gatekeeper for large cargo but also allow the small cargo diffuse into the pore channels and then be capped by a plug. Fluorescent molecules were chosen as cargos in order to establish a proof-of-principle operation for this dual cargo release system. The results in this study demonstrate that the small cargo can be released first by lowering the pH, and then the large cargo can be released after the cleavage of the disulfide bond.

The results reported here present a significant step toward the development and production of a multidrug delivery system. This system has the potential to treat human diseases where combination therapy is desired. In view of the lower lysosome pH levels and the presence of higher concentrations of glutathione in cancer cells, further investigations will employ this integrated nanosystem to carry two anticancer drugs (i.e., cisplatinum and doxorubicin) and perform *in vivo* dual drug release.

## 5.5. Experimental

*Synthesis of MSNs 3:* MSNs **2** (50 mg) were soaked in an aqueous solution of Hoechst 333422 (1 mL, 3.0 mM) overnight at room temperature. A solution of Per-6-azido-*β*-cyclodextrin (0.03 g, 0.3 mmol) in DMF (2 mL) was then added, followed by the addition of sodium ascorbate (2 mg, 0.01 mmol) and $CuSO_4 \cdot 5H_2O$ (0.75 mg, 3 μmol). The

reaction mixture was left to stir for 3 days at room temperature to allow the preparation of a layer of *β*-CD on the surface of the nanoparticles by means of a series of click reactions. The nanoparticles were then filtered and washed with copious amounts of MeOH, acidic $H_2O$ (pH 3) and $H_2O$, and then dried under vacuum to afford MSNs **3**. The fresh MSNs **3** were used immediately for the laser investigations involving fluorescence spectroscopy and release profiles.

*Synthesis of MSNs 5: β*-CD capped MSNs **4** (50 mg) were added to coumaric acid aqueous solution (1 mL, 1.0 mM). The suspension solution was shaken at room temperature for 24 hours to allow the coumaric acid to diffuse into the nanopores of the nanoparticles. The loaded particles were centrifuged to remove the loading solution. Methyl orange (50 mg) was then added to the pellet and re-suspended in $H_2O$ (0.5 mL). After the solution was left on a shaker at room temperature for another 24 h, MSNs **5** were obtained by centrifugation, washed with $H_2O$ (10 times), and dried under vacuum. Release studies were carried out immediately.

*Synthesis of MSNs 1:* To prepare the dual-loaded system, MSNs **3** (50 mg) were soaked in an aqueous solution of *p*-coumaric acid (1 mL, 1.0 mM) at room temperature for 24 hours. The loaded nanoparticles were then centrifuged to remove the loading solution. Methyl orange (50 mg, 0.15 mmol) was then added to the pellet and re-suspended in $H_2O$ (0.5 mL). The mixture was left on a shaker for another 24 hours at room temperature. The

resulting MSNs **1** were collected by centrifugation, washed by $H_2O$ (10 times), and dried under vacuum. Release studies were carried out immediately.

## 5.6. Figures and Tables

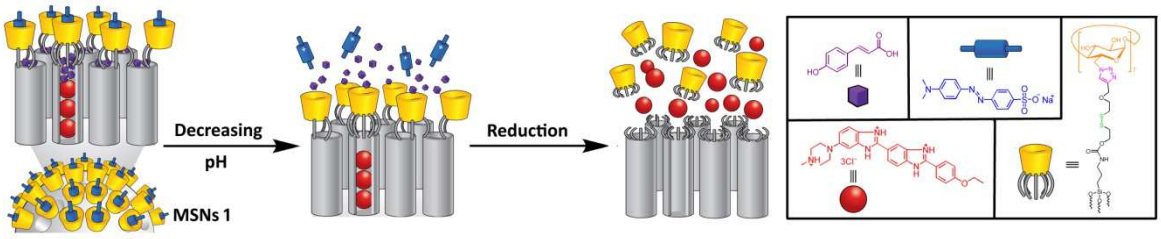


**Figure 5.1.** The schematic representation of the dual cargo release process. The dual cargos can be released step-by-step by first lowering the pH and then adding mercaptoethanol. For silica nanoparticles modified with $\beta$-CD rings, the $\beta$-CD rings are randomly distributed on the surface.

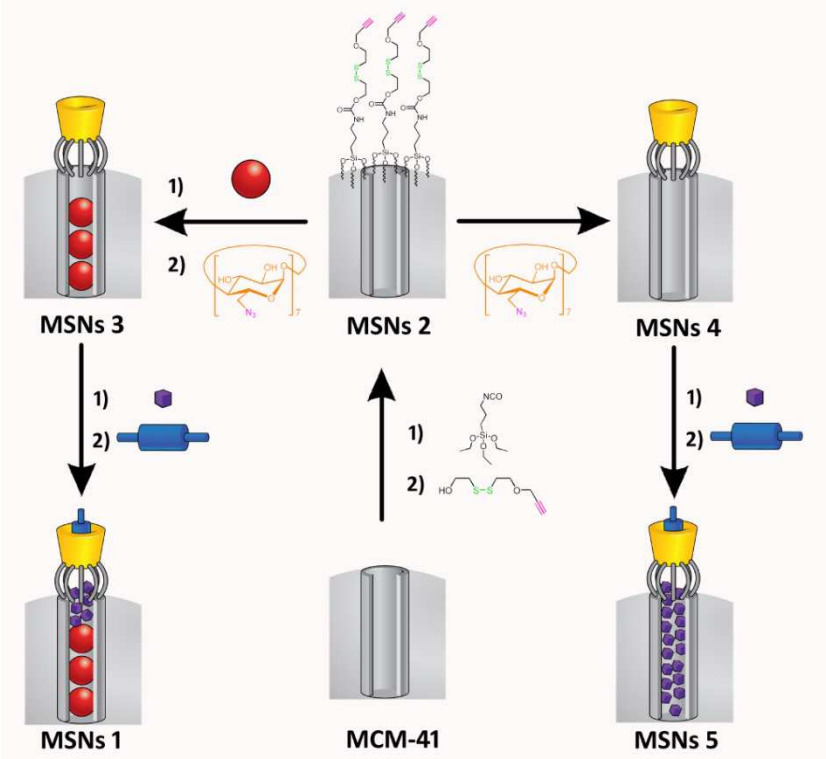


**Figure 5.2.** The synthetic procedure for MSNs **1** and MSNs **5**. Utilizing supramolecular chemistry and mechanostereochemistry, dual cargos (Hoechst 33342 and CA) were loaded into MSN **1** step-by-step. Although the *β*-CD rings are randomly distributed on the MSNs surface, the ideal mode is to have one nanopore functionalized with one *β*-CD ring according to the size match of the nanopore and the *β*-CD ring, as shown in the figure.

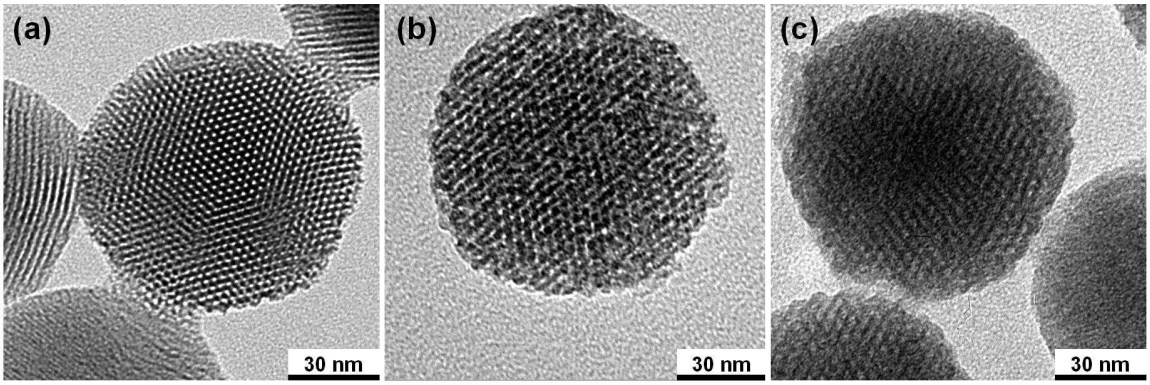


**Figure 5.3.** TEM images of the bare and functionalized MCM-41 nanoparticles. (a) Bare OH-surface MCM-41 mesoporous silica nanoparticles; (b) MSNs **4**; (c) Dual-loaded MSNs **1** assembled step-by-step.

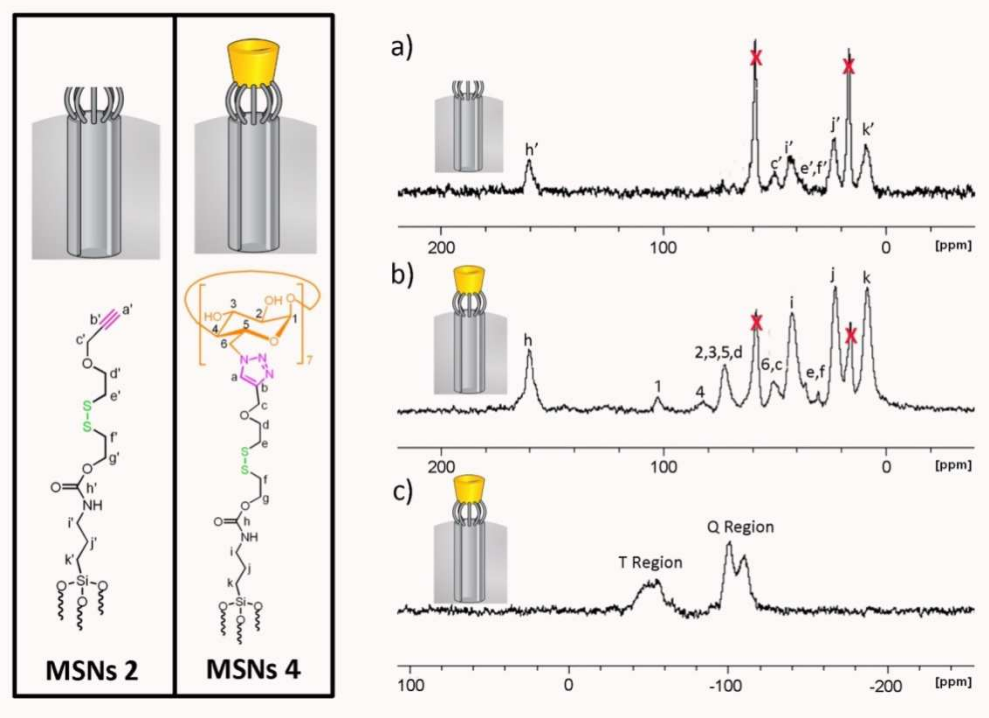


**Figure 5.4.** $^{13}C$ and $^{29}Si$ CP-MAS solid-state NMR spectra of MSNs **2** and the *β*-CD-capped MSNs **4**. a) $^{13}C$ CP-MAS solid-state NMR spectrum of MSNs **2**. b) $^{13}C$ CP-MAS solid-state NMR spectrum of MSNs **4**. c) $^{29}Si$ CP-MAS solid-state NMR spectra of MSNs **4**. The carbon nuclei of the linker and the *β*-CD ring are defined alongside the structural formula.

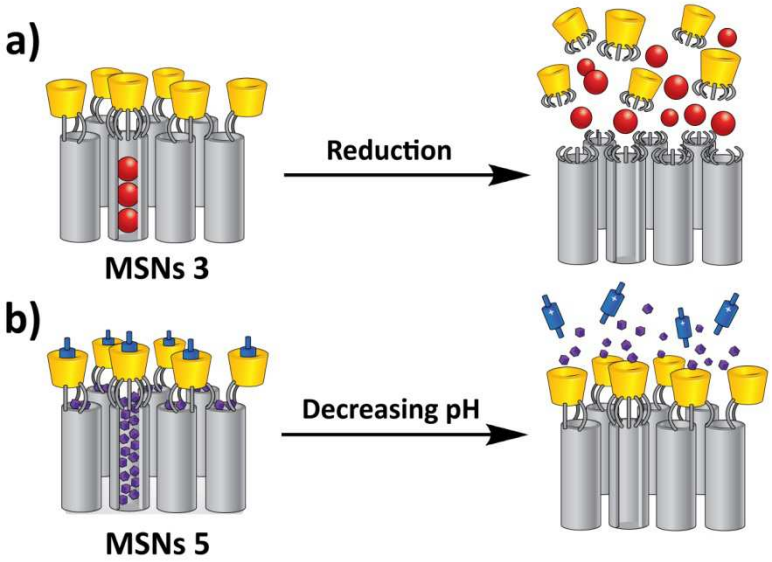


**Figure 5.5.** Schematic representation of the release process of a) MSNs **3**, which was prepared from Per-6-azido-*β*-CD and alkynyl-functionalized MSNs **2** in the presence of Hoechst 33342 by means of a series of click reactions; b) MSNs **5**, which was prepared from *β*-CD capped MSNs **4** and a MO plug in the presence of CA.

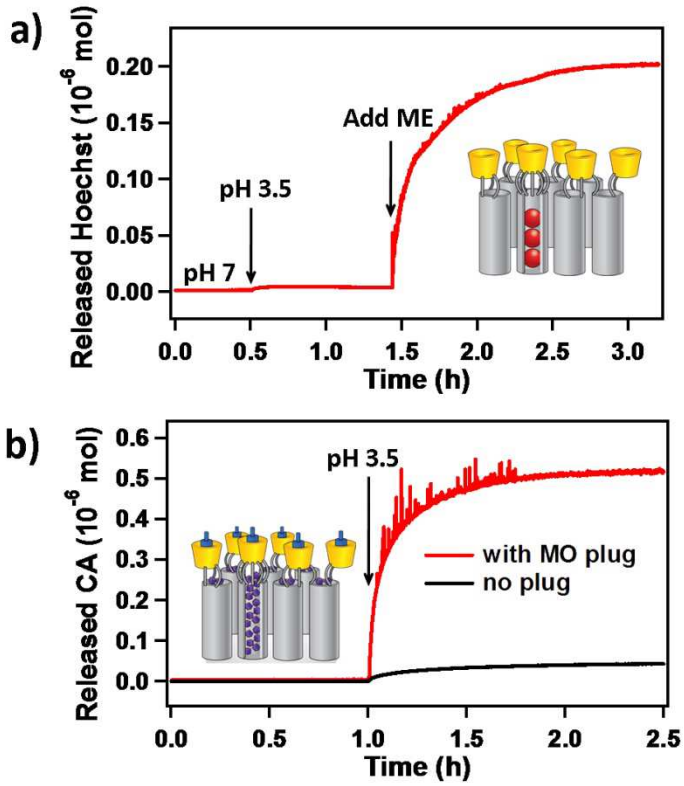


**Figure 5.6.** Release profiles of a) MSNs **3**, while monitoring emission of Hoechst 33342 at 500 nm following the addition of ME; b) MSN **5** and CA-loaded nanoparticles without the MO plugs, while monitoring emission CA after lowering the pH at 425 nm.

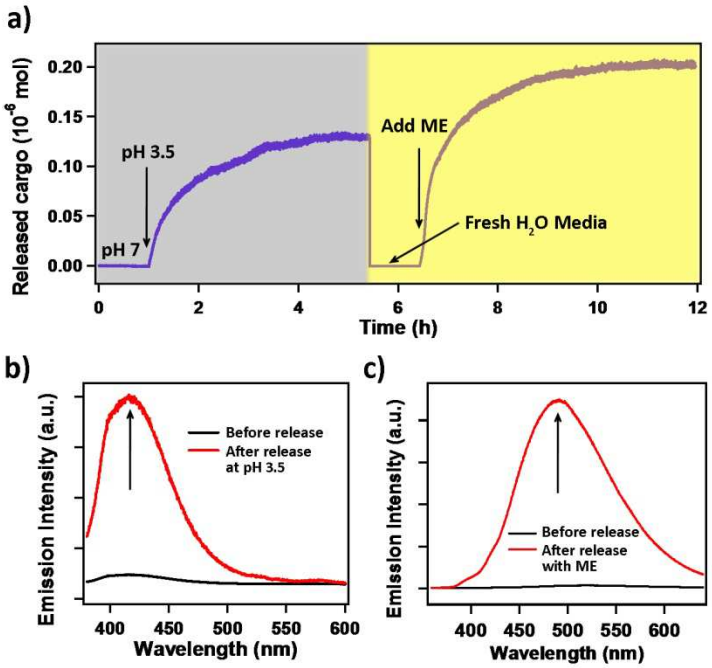


**Figure 5.7.** a) Step-by-step release profile of dual-cargo loaded MSNs **1** by lowering the pH (monitored at 425 nm) and then adding ME (monitored at 500 nm). The fluorescent spectra of dual-cargos loaded MSN **1** b) after lowering the pH; c) followed by addition of ME after changing the solution to fresh $H_2O$.

## 5.7. Reference


1. J. Jia, F. Zhu, X. Ma, Z. W. Cao, Y. X. Li, Y. Z. Chen, *Nature* **2009**, *8*, 111–128.
2. K. d. G. Donati, R. Rabagliati, L. Iacoviello, R. Cauda, *Lancet Infect. Dis.* **2004**, *4*, 213–222.
3. W. L. Suarez-Pinzon, R. F. Power, Y. Yan, C. Wasserfall, M. Atkinson, A. Rabinovitch, *Diabetes* **2008**, 57, 3281–3288.
4. D. Lane, *Nat. Biotech.* **2006**, *24*, 163–164.
5. a) R. Langer, *Science* **2006**, *249*, 1527–1533; b) T. M. Allen, P. R. Cullis *Science* **2004**, *303*, 1818–1822; c) J. Shi, A. R. Votruba, O. C. Farokhzad, R. Langer, *Nano Lett.* **2010**, *10*, 3223–3230.
6. K. E. Uhrich, S. M. Cannizzaro, R. S. Langer, K. M. Shakesheff, *Chem. Rev.* **1999**, *99*, 3181–3198.
7. C. C. Lee, J. A. MacKay, J. M. J. Fréchet, F. C. Szoka, *Nat. Biotech.* **2005**, *23*, 1517–1526.
8. K. Kataoka, A. Harada, Y. Nagasaki, *Adv. Drug Del. Rev.* **2001**, *47*, 113–131.
9. J. J. Moon, H. Suh, A. Bershteyn, M. T. Stephan, H. Liu, B. Huang, M. Sohail, S. Luo, S. H. Um, H. Khant, J. T. Goodwin, J. Ramos, W. Chiu, D. J. Irvine, *Nat. Mater.* **2011**, *10*, 243–251.
10. Brigger, C. Dubernet, P. Couvreur, *Adv. Drug Del. Rev.* **2002**, *54*, 631–651.
11. a) Y. Zhao, B. G. Trewyn, I. I. Slowing, V. S. Y. Lin, *J. Am. Chem. Soc.* **2009**, *131*, 8398–8400; b) C. E. Ashley, E. C. Carnes, G. K. Phillips, D. Padilla, P. N. Durfee, P.

A. Brown, T. N. Hanna, J. Liu, B. Phillips, M. B. Carter, N. J. Carroll, X. Jiang, D. R. Dunphy, C. L. Willman, D. N. Petsev, D. G. Evans, A. N. Parikh, B. Chackerian, W. Wharton, D. S. Peabody, C. J. Brinker, *Nat. Mater.* **2011**, *10*, 389–397.

12. a) N. Kolishetti, S. Dhar, P. M. Valencia, L. Q. Lin, R. Karnik, S. J. Lippard, R. Langer, O. C. Farokhzad, *Proc. Nat. Acad. Sci.* **2010**, *107*, 17939–17944; b) T. Okuda, K. Tominaga, S. Kidoaki, *J. Control Rel.* **2010**, *143*, 258–264.
13. a) A. Stein, B. J. Melde, R. C. Schroden, *Adv. Mater.* **2000**, *12*, 1403–1419; b) S. Angelos, E. Johansson, J. F. Stoddart, J. I. Zink, *Adv. Func. Mater.* **2007**, *17*, 2261-2271; c) M. Liong, S. Angelos, E. Choi, K. Patel, J. F. Stoddart, J. I. Zink, *J. Mater. Chem.* **2009**, *19*, 6251–6257; d) K. K. Coti, M. E. Belowich, M. Liong, M. W. Ambrogio, Y. A. Lau, H. A. Khatib, J. I. Zink, N. M. Khashab, J. F. Stoddart, *Nanoscale*, **2009**, *1*, 16–39; e) J. L. Vivero-Escoto, I. I. Slowing, B. G. Trewyn, V. S-Y. Lin, *Small* **2010**, *6*, 1952–1967; f) M. Manzano, M. Vallet-Regi, *J. Mater. Chem.* **2010**, *20*, 5593–5604; g) S. H. Wu, Y. Hung, C. Y. Mou, *Chem. Commun.* **2011**, *47*, 9972–9985.
14. a) M. Liong, J. Lu, M. Kovochich, T. Xia, S. G. Ruehm, A. E. Nel, F. Tamanoi, J. I. Zink, *ACS Nano* **2008**, *2*, 889–896; b) J. Lu, E. Choi, F. Tamanoi, J. I. Zink, *Small* **2008**, *4*, 421–426; c) J. M. Rosenholm, A. Meinander, E. Peuhu, R. Niemi, J. E. Eriksson, C. Sahlgren, M. Linden, *ACS Nano* **2009**, *3*, 197–206; d) H. Meng, M. Xue, T. Xia, Y.-L. Zhao, F. Tamanoi, J. F. Stoddart, J. I. Zink, A. E. Nel, *J. Am. Chem. Soc.* **2010**, *132*, 12690–12697.

15. a) M. Vallet-Regí, F. Balas, D. Arcos, *Angew. Chem.* **2007**, *119*, 7692–7703; *Angew. Chem. Int. Ed.* **2007**, *46*, 7548–7558; b) I. I. Slowing, J. L. Vivero-Escoto, C. -W. Wu, V. S. Y. Lin, *Adv. Drug Del. Rev.* **2008**, *60*, 1278–1288; c) M. W. Ambrogio, C. R. Thomas, Y. -L. Zhao, J. I. Zink, J. F. Stoddart, *Acc. Chem. Res.* **2011**, *44*, 903–913; d) J. E. Lee, N. Lee, T. Kim, J. Kim, T. Hyeon, *Acc. Chem. Res.* **2011**, *44*, 893–902; e) Z. Li, J. C. Barnes, A. Bosoy, J. F. Stoddart, J. I. Zink, *Chem. Soc. Rev.*, **2012**, doi:10.1039/C1CS152- 46G.

16. a) C. Park, K. Oh, S. C. Lee, C. Kim, *Angew. Chem.* **2007**, *119*, 1477–1479; *Angew. Chem. Int. Ed.* **2007**, *46*, 1455–1457; b) S. Angelos, Y. -W. Yang, K. Patel, J. F. Stoddart, J. I. Zink, *Angew. Chem.* **2008**, *120* 2254–2258; *Angew. Chem. Int. Ed.* **2008**, *47*, 2222–2226; c) L. Du, S. Liao, H. A. Khatib, J. F. Stoddart, J. I. Zink, *J. Am. Chem. Soc.* **2009**, *131*, 15136–15142; d) H. P. Rim, K. H. Min, H. J. Lee, S. Y. Jeong, S. C. Lee, *Angew. Chem.* **2011**, *123*, 9015–9019; *Angew. Chem. Int. Ed.* **2011**, *50*, 8853–8857.

17. a) Y. Zhu, M. Fujiwara, *Angew. Chem.* **2007**, *119*, 2291–2294; *Angew. Chem. Int. Ed.* **2007**, *46*, 2241–2244; b) S. Angelos, E. Choi, F. Vögtle, L. De Cola, J. I. Zink, *J. Phys. Chem. C* **2007**, *111*, 6589–6592; c) D. P. Ferris, Y. -L. Zhao, N. M. Khashab, H. A. Khatib, J. F. Stoddart, J. I. Zink, *J. Am. Chem. Soc.* **2009**, *131*, 1686–1688; d) S. Angelos, Y. -W. Yang, N. M. Khashab, J. F. Stoddart, J. I. Zink, *J. Am. Chem. Soc.* **2009**, *131*, 11344–11346; e) J. L. Vivero-Escoto, I. I. Slowing, C.-W. Wu, V. S. Y. Lin, *J. Am. Chem. Soc.* **2009**, *131*, 3462–3463.

18. K. C. F. Leung, T. D. Nguyen, J. F. Stoddart, J. I. Zink, *Chem. Mater*. **2006**, *18*, 5919–5928.

19. a) C.-Y. Lai, B. G. Trewyn, D. M. Jeftinija, K. Jeftinija, S. Xu, S. Jeftinija, V. S. Y. Lin, *J. Am. Chem. Soc.* **2003**, *125*, 4451–4459; b) T. D. Nguyen, H.-R. Tseng, P. C. Celestre, A. H. Flood, Y. Liu, J. F. Stoddart, J. I. Zink, *Proc. Nat. Acad. Sci.* **2005**, *102*, 10029–10034; c) K. Patel, S. Angelos, W. R. Dichtel, A. Coskun, Y.-W. Yang, J. I. Zink, J. F. Stoddart, *J. Am. Chem. Soc.* **2008**, *130*, 2382–2383; d) M. W. Ambrogio, T. A. Pecorelli, K. Patel, N. M. Khashab, A. Trabolsi, H. A. Khatib, Y. Y. Botros, J. I. Zink, J. F. Stoddart, *Org. Lett.* **2010**, *12*, 3304–3307.

20. a) C.-L. Zhu, C.-H. Lu, X.-Y. Song, H.-H. Yang, X.-R. Wang, *J. Am. Chem. Soc.* **2011**, *133*, 1278–1281; b) N. Singh, A. Karambelkar, L. Gu, K. Lin, J. S. Miller, C. S. Chen, M. J. Sailor, S. N. Bhatia, *J. Am. Chem. Soc.* **2011**, *133*, 19582–19585.

21. a) A. Schlossbauer, S. Warncke, P. M. E. Gramlich, J. Kecht, A. Manetto, T. Carell, T. Bein, *Angew. Chem.* **2010**, *122*, 4842 – 4845; *Angew. Chem. Int. Ed.* **2010**, *49*, 4734 – 4737; b) E. Aznar, L. Mondragón, J. V. Ros-Lis, F. Sancenón, M. D. Marcos, R. Martínez-Máñez, J. Soto, E. Pérez-Payá, P. Amorós, *Angew. Chem.* **2011**, *123*, 11368–11371; *Angew. Chem. Int. Ed.* **2011**, *50*, 11172–11175.

22. a) F. Cramer, *Einschlussverbindungen*, Springer-Verlag, Berlin, **1954**; b) D. French, *Adv. Carbohydr. Chem*. **1957**, *12*, 189–260; c) F. Cramer, *Angew. Chem.* **1956**, *68*, 115–120; d) M. L. Bender, M. Komiyama, *Cyclodextrin Chemistry*, Springer-Verlag, Berlin, 1978; e) R. Breslow, *Chem. Soc. Rev*. **1972**, *1*, 553–580; f) J. Szejtli,

*Cyclodextrin Technology*, Kluwer Academic Publishers, Dordrecht, **1988**; g) W. Saenger, *Angew. Chem.* **1980**, *92*, 343–361; *Angew. Chem. Int. Ed.* **1980**, *19*, 344–366; h) I. Tabushi, *Pure Appl. Chem.* **1986**, *58*, 1529–1534; i) J. F. Stoddart, *Carbohydr. Res.* **1989**, *192*, xii–xv; j) K. A. Connors, *Chem. Rev.* **1997**, *97*, 1325–1358; k) M. V. Rekharsky, Y. Inoue, *Chem. Rev.* **1998**, *98*, 1875–1918; l) H. Dodziuk, *Cyclodextrins and Their Complexes*, Wiley-VCH, Weinheim, **2006**; m) Y. Chen, Y. Liu *Chem. Soc. Rev.* **2010**, *39*, 495–505; n) R. Breslow, in *Molecular Encapsulation*, (Eds. Uso Berinker and Jean-Luc Mieusset), Wiley, Chichester UK, **2010**, pp. 43–65.

23. a) H. Kim, S. Kim, C. Park, H. Lee, H. J. Park, C. Kim, *Adv. Mater.* **2010**, *22*, 4280–4283; b) C. Park, K. Lee, C. Kim, *Angew. Chem.* **2009**, *121*, 1301–1304; *Angew. Chem. Int. Ed.* **2009**, *48*, 1275–1278; c) Y.-L. Zhao, Z. Li, S. Kagehie, Y. Y. Botro, J. F. Stoddart, J. I. Zink, *J. Am. Chem. Soc.* **2010**, *132*, 13016–13025.
24. The MCM-41 mesoporous silica nanoparticles were synthesized using a surfactant-templated sol-gel process. (See: M. Liong, J. Lu, M. Kovochich, T. Xia, S. G. Ruehm, A. E. Nel, F. Tamanoi, J. I. Zink, *ACS Nano* **2008**, *2*, 889–896.) The templating surfactant was removed by acid extraction, and the morphology of the resulting particles was characterized by transmission electron microscopy TEM and X-ray diffraction XRD. The spherical particles are around 100 nm in diameter and display hexagonal arrays of pore channels of around 2.5 nm.
25. a) R. Hong, G. Han, J. M. Fernández, B. Kim, N. S. Forbes, V. M. Rotello, *J. Am. Chem. Soc.* **2006**, *128*, 1078–1079; b) S. Takae, K. Miyata, M. Oba, T. Ishii, N.

Nishiyama, K. Itaka, Y. Yamasaki, H. Koyama, K. Kataoka, *J. Am. Chem. Soc.* **2008**, *130*, 6001–6009.

26. Although the binding constant was obtained in solution state, we assume that the sites of host-guest binding between the plugs and the β-CD rings are equivalent on surfaces. See: M. J. W. Ludden, X. Li, J. Greve, A. Amerongen, M. Escalante, V. Subramaniam, D. N. Reinhoudt, J. Huskens, *J. Am. Chem. Soc.* **2008**, *130*, 6964–6973.
27. Y. Liu, C.-C. You, S. He, G.-S. Chen, Y.-L. Zhao, *J. Chem. Soc., Perkin Trans.* **2002**, *2*, 463–469.
28. The p*K*a of MO is 3.47. MO has been used as pH indicator and it shows a color transition between pH 3.1~4.4.

# Part III

# Biomedical Applications of Mesoporous Silica Nanoparticles

# Chapter 6

# *In Vitro* Study of Mesoporous Silica Nanoparticles as siRNA Delivery Vehicles for Cancer Gene Therapy

## 6.1. Abstract

The functionalization of the surface of mesoporous silica nanoparticles (MSN) with a phosphonate group allows electrostatic binding of positively charged anti-cancer drugs to the porous interior, from where the drug could be released by acidification of the medium under abiotic and biotic conditions. In addition, phosphonate modification also allows exterior coating with the cationic polymer, polyethylenimine (PEI), which endows the MSNs to contemporaneously deliver the negatively charged nucleic acids. In this chapter, it will be demonstrated that mesoporous silica nanoparticles coated with PEI can deliver small interfering RNA (siRNA) to silence transgene expression. It will also be shown that these PEI-MSNs can be functionalized to effectively deliver a chemotherapeutic agent doxorubicin (Dox) as well as Pgp siRNA to a drug-resistant cancer cell line (KB-V1 cells) to accomplish cell killing in an additive or synergistic fashion. The biological experiments were performed by the collaborator in the research groups of Dr. Fuyuhiko Tamanoi and Dr. Andre E. Nel at UCLA.

## 6.2. Introduction

Genetic diseases are illnesses caused by abnormalities in genes or chromosomes, including hemophilia, Huntington's disease, and cancer. They can be caused by both genetic and environmental predispositions. Small interfering RNA (siRNA) is a powerful tool to inhibit gene function because it can be easily applied to any therapeutic target, providing revolutionary potency and selectivity of improved targeted therapeutics.[1] However, poor intracellular uptake, instability, and non-specific immune stimulation are obstacles associated with current methods of siRNA oligonucleotide delivery. Therefore,

developing a stable, highly effective siRNA delivery system with optimal cellular integration and low toxicity is of utmost importance. In the studies described in this chapter, we successfully use a nanocomplex assembly of polyethylenimine (PEI) and mesoporous silica nanoparticles (MSNs) to protect and deliver siRNA into human cells, and effectively shutdown both exogenous and endogenous gene signals.

In order to bind negatively charged nucleic acids and improve uptake, silica materials are typically modified with positively charged organic adjuncts, such as poly-l-lysine (PLL) or polyethyleneimine (PEI).[2-4] Consequently, we incorporated the cationic polymer, PEI (Figure 6.1D), to effect siRNA encapsulation in MSNs (PEI-MSNs; Figure 6.1E). Additionally, PEI is reported to promote nanoparticles' endosomal escape due to its ''proton sponge effect'',[3, 5, 6] although in our previous study, the MSNs were observed to be able to release loaded cargo out of endolysosomes into cytosol.[7] As discussed below, PEI-MSNs are biocompatible, possess high affinity for their particular payload, sequester their payload, and allow delivery of their contents. PEI/siRNA complexes alone have been used for nonviral gene delivery but their cytotoxicity has been an obstacle to *in vivo* applications.[8] Compared to other nonviral transfection vehicles, such as Lipofectamine 2000 and PEI/siRNA complexes, PEI-MSNs showed much less cytotoxicity to cells,[9] suggesting that PEI-MSNs are a less toxic alternative for siRNA delivery. Moreover, having the porous structure would provide the possibility of both binding of siRNA on the nanoparticles surface and loading of small molecules, such as chemotherapeutic drugs, within the pores, providing dual delivery of drugs and nucleic acids.[10,11]

There are a number of circumstances where dual drug and siRNA delivery could achieve a synergistic therapeutic outcome. One example is the restoration of drug sensitivity in cancer cells by the knockdown of genes that are involved in the resistance to one or more chemotherapeutic agents. An example is the inducible P-glycoprotein (Pgp) gene that encodes for a gene product known as the multiple drug resistance protein 1 (MDR-1).[12] Pgp is constitutively expressed in normal cells such as capillary endothelial cells in the blood brain barrier but also is selectively overexpressed in carcinomas of the stomach, breast, pancreas, and cervix in response to a number of chemotherapeutics agents.[13] If overexpressed, Pgp could lead to drug resistance because MDR-1 contributes to the formation of a drug efflux pump that prevents the intracellular buildup of chemotherapeutic agents.[14] Because Pgp overexpression is one of the major mechanisms of multiple drug resistance (MDR) in cancer cells, knockdown of Pgp gene expression by nanoparticle siRNA delivery could help to restore the intracellular drug levels to the concentrations required for induction of apoptosis and cytotoxicity. Thus, dual drug and siRNA delivery by nanoparticles can be used to overcome drug resistance in MDR cancer cells.

To test the utility of MSN as a dual delivery platform, we used the drug-resistant squamous carcinoma cell line, KB-V1, to see if Pgp knockdown restores doxorubicin (Dox) sensitivity. KB-V1 cells exhibit MDR as a result of Pgp overexpression.[13] To effectively engineer particles to deliver Dox as well as Pgp siRNA, it was necessary to demonstrate that particle functionalization by the attachment of negative (phosphonate) as well as positive (PEI) surface groups is functionally effective. Moreover, since PEI

delivery of siRNA constructs to the cytosol requires intermediary lysosomal processing, we were also interested to determine whether this endocytic route is appropriate for Dox delivery. We demonstrate that Dox can be stably attached to the porous interior by a proton-sensitive electrostatic binding interaction that allows effective drug release from the acidifying LAMP-1-positive compartment. Pgp siRNA co-delivery increases intracellular Dox concentrations with improved cytotoxic killing. The improvement of Dox resistance provides proof-of-principal testing that MSN can be engineered to provide contemporaneous drug and siRNA delivery by effective use of charge and the state of protonation or deprotonation at the particle surface.

## 6.3. Results and Discussion

### 6.3.1. PEI-MSN-Mediated EGFP Silencing in PANC-1 Cells

The ability of PEI-MSNs to complex with siRNA was confirmed by UV absorption measurements and gel assays. PEI-MSNs were incubated with enhanced green fluorescent protein (EGFP) siRNA overnight at 4 °C to allow loading. They were then washed with phosphate buffered saline (PBS) solution to remove any unbound siRNA. Double-stranded siRNA has 11 base pairs per turn, with a diameter of 2.6 nm.[15] Since our nanoparticles have an average pore diameter of 2.5 nm, it is plausible for siRNA to enter MSN pores if they adopt the necessary orientation. However, because PEI coats both the external and pore nanoparticle surfaces, it is more likely that the majority of bound siRNA attaches to the external surface since no particular siRNA orientation is required. The gel assay showed negligible release of siRNA when bound to PEI-MSNs during electrophoresis (Figure 6.2, Lane 4). To confirm the binding between PEI-MSNs and

siRNA, absorption measurements determined that 175 mg of PEI-MSNs could sequester approximately 0.35 nmol of siRNA (approximately 2 pmol $mg^{-1}$ siRNA/MSN; Figure 6.1C). Agarose gel electrophoresis analysis also established that PEI-MSNs could protect siRNA from enzymatic cleavage. It has been previously reported that carbosilane dendrimer nanoparticles exhibit a protective effect on nucleic acids.[16] We sought to determine if the same was true for MSNs following the published protocol.[16] Similar to our UV absorption experiment, PEI-MSNs were loaded with EGFP siRNA by incubating them overnight at 4 °C. After washing with PBS to remove unbound siRNA, RNase A was added to the complex in solution, incubated at 37 °C for 1 h, and heparin was used to liberate siRNA from the PEI-modified nanoparticles immediately before running on the gel. Naked siRNA was completely degraded by RNase A treatment prior to gel electrophoresis (Figure 6.2, Lane 2), while siRNA retained in the gel wells due to their union with MSNs showed no signs of RNase degradation whatsoever (Figure 6.2, Lane 4). The small amount of siRNA that was not bound to the MSNs in the sample was presumably degraded due to RNaseA (Figure 6.2, Lane 4). Finally, the bound siRNA was found to be still intact following exposure to RNase A treatment and subsequent dissociation from MSNs by heparin (Figure 6.2, Lane 7). The size of the releasedsiRNA was the same as that released from PEI-MSNs (Lane 5). As a control, we also released bound siRNA with heparin then exposed the dissociated complex to RNase to confirm that free siRNA could still be degraded (Figure 6.2, Lane 6). Thus, we have shown that PEI-modified MSNs are able to efficiently complex with siRNAs and protect their siRNA payload from enzymatic degradation, an important finding if PEI-MSNs are to be utilized

in *in vivo* therapies. Next, we wanted to determine the intracellular fate of PEI-MSNs as siRNA carriers. In particular, it was of great importance to provide evidence of activity of the siRNA inside cells. This capability was tested in PANC-1 cells stably expressing EGFP (PANC-1/EGFP) through Lipofectamine 2000-mediated transfection. To test the specificity of knockdown, two different types of siRNAwere used for nanocomplex formation: siRNA against EGFP and a scrambled siRNA sequence as a control. Ahomogenous suspension of the EGFP siRNA-loaded PEI-MSNs in fetal bovine serum (FBS)-free media was added to PANC-1/EGFP cells to determine if the nanoparticles were able to transport siRNA into cancer cells and silence EGFP expression. The EGFP transgene was chosen for our initial *in vitro* experiments because EGFP's fluorescence properties facilitated analysis of silencing efficiency (Figure 6.1A). As EGFP emits strong green fluorescence (509 nm) under UV excitation (395 nm), we used fluorescence microscopy to monitor the distribution of EGFP-expressing cells following treatment (Figure 6.3A). As seen in Figure 6.3A g and h, siRNA-loaded PEI-MSNs caused dramatic decrease in the number of fluorescent cells (compare Figure 6.3Ad and h). As a comparison, a suspension of the same concentration of EGFP siRNA in FBS-free media was transfected into the cells by lipofectamine 2000 (Figure 6.3Ae, f). It appears that the use of siRNA-PEI-MSNs provides comparable or even better efficacy of delivering siRNA in silencing EGFP compared with Lipofectamine (Figure 6.3A, B, the down-regulation by siRNA-PEI-MSNs in PANC-1 cells is 61.7%). Control formulations with scrambled siRNA introduced through lipofectamine or PEI-MSNs revealed that gene silencing was highly specific. These results suggested that siRNA-loaded PEI-MSNs are

capable of sequestering and protecting siRNA, and delivering it intracellularly to affect transgene shutdown. Having proven that PEI-MSNs can deliver siRNAto silence transgene expression, the next logical step was to silence an endogenous gene. Accumulating genetic and cancer biology studies indicate a prominent role for Akt in cancer cell growth and survival, and have culminated in the aggressive development of PI3K/Akt pathway inhibitors as cancer therapies.[17] Therefore, we decided to test firstly the effect of delivering siRNA against Akt by PEI-MSNs to human cancer cells. A homogenous suspension of the Akt siRNA-loaded PEI-MSNs in FBS-free media was added to PANC-1 cells and incubated as described in the Experimental Section. Western-blot analysis indicated that upon incubation with siRNA-loaded nanoparticles, Akt expression was attenuated (Figure 6.3C, compare Lanes 1, 4, and 5). As a positive control, Akt siRNA was also introduced through Lipofectamine 2000 transfection into PANC-1 cells, and Akt expression was reduced to a similar degree as with nanoparticles (Lane 3). Thus, siRNA-loaded PEI-MSNs are capable of delivering siRNA into cancer cells to effect gene silencing of endogenous targets. To further investigate the shutdown of endogenous gene by PEI-MSN delivery of siRNA, we next tested K-ras signaling with a siRNA against K-ras, which is another critical target for cancer therapeutics, because activated mutations of K-ras are found in various cancers, including pancreatic cancers.[18] As shown in Figure 6.3D, expression of p-Erk, a direct downstream molecule of K-ras, was significantly reduced by PEI-MSN-mediated siRNA (compare Lanes 1, 4, and 5). The total Erk level, on the other hand, was unchanged.

### 6.3.2. Simultaneous Delivery of Dox and Pgp siRNA to KV-V1 Cells

To assess the efficacy of Pgp siRNA delivered by PEI coated particles, Pgp expression was followed by Western blotting. This demonstrated 80 or 90% reduction in MDR-1 expression in cells treated with PEI-coated particles that contain the 10 and 25 kD polymers, respectively. This efficacy was maintained in Dox-loaded MSN. Scrambled siRNA-PEI-MSN was used as a negative control to rule out any impact by the siRNA delivery method. No Pgp knockdown was seen in the scrambled siRNA-MSN group. The PEIcoated particles were also more effective than the commercially available transfection agent, Lipofectamine 2000, which is widely used in molecular biology.

An important consideration in the use of PEI is its potential cytotoxicity.[11] In this regard, we have recently shown that polymer size plays an important role in the cytotoxicity that results from proton sequestration by unsaturated PEI amines in the lysosomal compartment.[11] Thus, before the performance of Dox-induced cytotoxicity test, it was necessary to compare the cytotoxic potential of MSN coated with different PEI polymer length. In brief, the findings were that MSN coated with the 25 kD polymer shows considerable toxicity in the MTS assay when the particle concentration is >25 μg/mL. By contrast, particles coated with 10 kD PEI have no toxic effects if the concentration is kept <100 μg/mL and the exposure time is limited to <24 h. Consequently, we used MSN at doses <100 μg/mL and for exposure time periods <24 h in the drug delivery studies to avoid effects on cell viability. Although no cytotoxicity was seen with the 1.8 kD PEI polymer, this particle is relatively ineffective for siRNA delivery and Pgp knockdown.

We have recently demonstrated that MSN are capable of loading and releasing water insoluble drugs (paclitaxel and camptothecin) by a phase transfer mechanism that can be reversed by ethanol washing of the particles to demonstrate the role of hydrophobicity in MSN drug entrapment.[7, 11] A key question was whether similar effective packaging of water-soluble Dox, is possible at physiological pH, where the drug (p*K*a = 8.2) carries a positive charge. One conceivable approach is electrostatic attachment to the negatively charged MSN surface. To test this possibility, Dox was loaded in MSN decorated with OH, COOH, or phosphonate groups. These particles were also compared to positively charged particles decorated with amine groups. After washing of the drugbound particles and quantification of Dox release by HCl, the loading capacities of OH-, COOH-, and phosphonate-MSN were 1.2%, 4.2%, and 8.4% (w/w), respectively. By contrast, amine-decorated particles showed low (<0.1%, w/w) Dox binding capacity. The principle of electrostatic binding to a negatively charged particle surface was also demonstrated through the use of a cationic dye, Hoechst 33342, which bound to a negative but not a positive MSN surface. Importantly, electrostatic binding of Dox to the phosphonate surface was not negated when the particles were also coated with 10 or 25 kD PEI polymers; these particles demonstrated an equivalent loading capacity to the uncoated phosphonate particles.

Importantly, Dox could be released in a time dependent manner from the phosphonate-MSN or PEI-phosphonate-MSN surface by lowering of the solution pH. The Dox release profile was not affected by the siRNA binding to PEI on the exterior surface of the particle. This establishes the possibility that intracellular drug release

should be possible if the particles are capable of gaining entrance to acidifying cellular compartments. To determine whether this is possible in KB-V1 cells, we studied the intracellular localization of FITC-labeled MSN in relation to lysosomal costaining by fluorescent labeled anti-LAMP-1 antibody. Indeed, confocal microscopy confirmed >55% colocalization of the green-labeled particles with the red-labeled lysosomes. Moreover, in a subsequent confocal study we demonstrated that released Dox from PEI coated particles after entrance into the lysosome could reach the nucleus, which was brightly stained by the fluorescent drug. Please notice that some of the drug was retained in particles localized in the peri-nuclear region. This visual image changed completely when cells were treated with $NH_4Cl$; most Dox remained confined to the lysosomal compartment with little or no nuclear staining. This suggests that the interference in lysosomal acidification by $NH_4Cl$ prevents effective Dox release to KB-V1 nuclei.

We have already discussed the relative inefficiency of free Dox to induce KB-V1 cytotoxicity as a result of the rapid rate by which the drug was being exported by the overexpressed Pgp. Intracellular Dox concentration can be determined by measuring cellular Dox fluorescence intensity in a microplate reader (Figure 6.5A). The comparatively low drug uptake after treatment with free Dox was slightly improved by delivering the drug *via* the phosphonate-MSN. While the total amount of intracellular drug increased when being delivered by particles coated with the 10 kD PEI polymer (Figure 6.5A), little of the drug reached the nucleus as determined by confocal imaging (Figure 6.5B). Interestingly, the intracellular Dox concentration increased significantly in the presence of siRNA (Figure 6.5A) so that there was also a significant increase in

nuclear Dox staining by 72 h (Figure 6.5B). This contrasts with most of the Dox being confined to the endosomal compartment in cells not receiving siRNA, suggesting that although PEI-MSN may take more Dox into to cells, any released drug is rapidly extruded from the cell before reaching the nucleus (Figure 6.5B). This suggests that knocking down Pgp expression allows a sufficient quantity of the drug being slowly released from the particle to enter the nucleus where it induces cytotoxicity. A quantitative measurement of Dox release to the nucleus through the use of Image J software confirmed a statistically significant increase of the drug in KB-V1 nuclei after delivery by siRNA-PEI-Dox-MSN as compared to free Dox or Dox loaded into the particles without siRNA (Figure 6.5C). Dox delivered by PEI-MSN in the presence of siRNA significantly enhances intranuclear Dox concentration when compared to free Dox or Dox delivered by MSN or PEI-MSN without siRNA.

To reconcile these findings with improved cell killing, we used the MTS assay to compare KB-V1 cytotoxicity under incremental Dox concentration. On the basis of the calculated $IC_{50}$ values of the various formulations, it was possible to rank the killing efficiency as follows: siRNA-PEI-Dox-MSN > PEI-Dox-MSN ≈ Dox-MSN > free Dox. Moreover, the $IC_{50}$ value of the siRNA-delivering MSN was approximately 2.5 times lower than the $IC_{50}$ of free Dox or other Dox-loaded particles. This suggests an additive effect between the drug and the siRNA that are being delivered by MSN. Although it was not possible to restore drug sensitivity to the level seen in KB-31 cells, we could clearly observe a much higher percentage of apoptotic KB-V1 cells after treatment with Dox-loaded MSN that codeliver siRNA as compared to free Dox or Dox delivered by non-

siRNA delivering particles. We confirmed the flow cytometry data through the use of another apoptosis assay using TUNEL staining, which showed an identical trend. Failure to fully restore drug sensitivity could be due to extremely high levels of Pgp expression and/or additional drug resistant pathways in KB-V1 that were not targeted in the current research. Because of the duration of time it takes for the siRNA to exert its effect, we also analyzed cell viability after longer treatment periods (*e.g*., 96 h) but did not observe any improvement in cytotoxicity. In addition, we also treated the KB-V1 cells by coadministration of Dox and Tariquidar, which is a potent and effective Pgp inhibitor in human clinical trial, to see if we can restore KB-V1 sensitivity to that seen in KB-31 cells. While this combination significantly improves cell killing capability in KB-V1 cells, it is incapable of completely restoring Dox sensitivity to the level seen in KB-31 cells.

## 6.4. Conclusions

We have successfully shown nanocomplex assembly between PEI-MSNs and siRNA. Introduction of PEI to MSNs significantly improved the encapsulation of siRNA and its release, compared to siRNA/PEI complex, while at the same time conferring protection from enzymatic degradation. The latter finding is of notable significance because it supports the possibility of utilizing PEI-MSNs in *in vivo* silencing applications. Our technique offers a unique opportunity to fabricate well-defined and homogenously distributed nanocarriers for siRNA delivery.

Intracellular siRNA release is the proposed mechanism of gene silencing observed with PEI-MSNs. The exact mechanism and timing surrounding the release of nucleic acids from MSNs remains to be determined; however, gene silencing has been detected,

indicating that a dissociation event has occurred. Previous work in our laboratory has shown that MSNs localize to the lysosome of mammalian cells upon cellular uptake before releasing their contents.[7, 19] This parallels the suggested theory that PEI confers increased gene delivery to nanoparticles due to its "proton sponge effect", allowing endosomal escape.[3, 5, 6] This provides the possibility of using PEI-coated MSNs for *in vivo* siRNA delivery for biomedical applications.

MSNs can also be functionalized to act as a dual delivery vehicle for Dox and Pgp siRNA in a drug resistant cancer cell line. To improve the drug sensitivity of KB-V1 cells, we used phosphonate attachment to deliver the drug as well as the siRNA *via* a lysosomal processing pathway. This dual delivery system increased the intracellular Dox levels to the extent that it improves cytotoxic killing in this KB-V1MDR cell line. This strategy could be an effective new approach for the treatment of cancers that develop multiple drug resistance.

## 6.5. Experimental

Synthesis of nanoparticles and loading of siRNA: All chemicals for the synthesis of the nanoparticles were purchased from Sigma–Aldrich. The PEI-MSNs were synthesized by first dissolving 100 mg cetyltrimethylammonium bromide (CTAB, Aldrich, 95%) in a solution of 48 mL water and 350 mL sodium hydroxide (2 M) and heating to 80 °C. After the temperature had stabilized, 0.5 mL of tetraethylorthosilicate (Aldrich, 98%) was added into the aqueous solution containing CTAB surfactants. After 15 min, 127 mL of 3-(trihydroxysilyl)propyl methylphosphonate (Aldrich, 42%) was added into the mixture, and the solution was stirred for another 2 h. The resulting

particles were centrifuged and washed with methanol. The surfactants were removed from the pores by dispersing the particles in a solution of 20 mL methanol and 1mL hydrochloric acid (12.1 M) and refluxing the mixture for 24 h. The materials were then centrifuged and washed with ethanol. 5mg of particles were then dispersed in a solution of 2.5 mg polyethyleneimine (PEI 1.2, 1.8, 10, 25 kD) and 1 mL absolute ethanol, stirred for 30 min, and then washed with ethanol and deionized water.

The synthetic siRNA and negative control sequences targeting the EGFP transgene were purchased from Ambion, CA (Ambion EGFP siRNA, Cat AM4626). The synthetic siRNA sequences for human K-ras (sense, 5-CUAUGGUCCUAGUAGGAAAtt, Antisense, 5-UUUCCUACUAGGACCAUAGgt) were purchased from Ambion Applied biosystems, for human Akt from Cell Signaling (SignalSilence Akt siRNA II, #6510). All siRNA sequences were prepared in DepC-treated water to a final concentration of 50 mM and stored at the appropriate temperature.

To load siRNA onto nanoparticles, PEI-MSNs were rotated with siRNA at a nanoparticle: siRNA ratio of 1:25 by mass in FBS-free media at 4 °C. After 24 h, the mixture was centrifuged and the supernatant was removed. By using a spectrophotometer, the absorption measurements of the original solution and the supernatant were compared to determine the amount of siRNA that was loaded onto the PEI-MSNs. The siRNA-loaded PEI-MSNs were then resuspended in the original volume and vortexed to disperse the loaded nanoparticles.

Because Dox is positively charged under physiological pH, it was necessary to demonstrate that phosphonate or other anionic surface groups are effective for drug

binding, including binding in particles that have been coated with PEI. To demonstrate this principle, we decorated particle surfaces with carboxylate (COOH) and amine groups in addition to phosphonate and silanol (OH groups). The surface functionalization was achieved by mixing organoalkoxysilanes (made up in ethanol) with TEOS before adding the mixture into the CTAB solution.23 For carboxylate modification, 50 μL of cyanoethyltriethoxysilane was mixed with 500 μL of ethanol and 500 μL of TEOS, then added into the surfactant solution. After the surfactant removal process, the particles were further heated in a solution of 50% sulfuric acid to hydrolyze the cyanide groups into carboxylic groups. For amine modification, 50 μL of aminopropyltriethoxysilane was first mixed with 500 μL ethanol and 500 μL TEOS, and then this mixture was added to the surfactant solution. After 2 h, the solution was cooled to room temperature and the materials were washed with methanol before the surfactant removal process was performed.

Cell culture: The human cancer-cell line PANC-1 was maintained in Dulbecco's modified Eagle's medium (DMEM; GIBCO) supplemented with 10% FBS (Sigma), 2% L-glutamine, 1% penicillin, and 1% streptomycin stock solutions. The medium was changed every three days, and the cells were passaged by trypsinization before confluence.

Gel electrophoresis and RNase protection assays: For protective-effect experiments, siRNA-loaded PEI-MSNs or siRNA alone were incubated with 0.25% RNase (Sigma) for 1 h and then loaded on a 4% agarose gel containing 0.0125% ethidium bromide and run at 100 V for 30 min. To release the bound siRNA, PEI-MSNs

loaded with siRNA were treated with 16.6 U $\mu L^{-1}$ heparin in DEPCtreated water immediately before gel electrophoresis.[16]

Fluorescence microscopy: PANC-1 cells were seeded in 8-well plates at a seeding density of 5×104 cells/well 24 h prior to the experiment. Following attachment, the medium was changed and the cells were transiently transfected with the EGFP transgene (1.3 mg/mL/well) using Lipofectamine 2000 (Invitrogen) to constitutively express high levels of the protein. Following incubation for 4–6 h at 37 °C, the medium was changed to serum-rich medium to allow the cells to recover. After 24 h, the cells were then treated with nanoparticles loaded with EGFP-targeted siRNA (0.1 mg nanoparticles/mL/well), siRNA (dose equivalent to that in the nanoparticle treatment) along with the transfecting agent Lipofectamine 2000, nanoparticles containing scrambled siRNA, or empty nanoparticles. All the treatments were carried out in the respective growth medium without serum. After 24 h incubation with the treatments, cells were washed with PBS and incubated in serum-rich media for 48 h. The fluorescence of the nanoparticles at an excitation wavelength of 395 nm was used to confirm the occurrence of GFP expression. PANC-1 cells that were transiently transfected with the EGFP transgene were incubated with PEI-MSNs for 48 h and then washed with DMEM medium and PBS to wash off the nanoparticles that did not enter the cells. The cells were then monitored by fluorescence microscopy with an excitation wavelength of 395 nm, and emission wavelength of 509 nm. The green emission was passed through a 530-nm bandpass filter. The emissions were collected by using two photomultiplier tubes. GFP exhibits intense green fluorescence under UV light. This property allows the use of fluorescence to study the

distribution of GFP in PANC-1 cells. PANC-1 cells were incubated with siRNA-loaded PEI-MSNs or siRNA suspended in PBS (160 nm) for 48 h, washed three times with PBS, and then examined by fluorescence microscopy under UV light.

Western-blot analysis: PANC-1 cells were seeded in 12-well plates at a seeding density of 1.5105 cells/well 24 h prior to the experiment. Following attachment, the medium was changed and cells were then treated with nanoparticles containing Akt- or K-rastargeted siRNA (175 mg nanoparticles/mL/well), siRNA (dose equivalent to that in the nanoparticle treatment) along with the transfecting agent Lipofectamine 2000 (Invitrogen), nanoparticles containing scrambled siRNA, or empty nanoparticles. All the treatments were prepared in serum-free DMEM. After 24 h incubation with the treatments, cells were washed with PBS and incubated in serum-rich DMEM to allow for recovery.

Proteins were separated by gel electrophoresis on a polyacrylamide gel containing SDS and then transferred to nitrocellulose membranes. The membranes were blocked with tris-buffered saline (TBS) containing 5% (w/v) skimmed milk. After being washed with TBS containing 0.1% Tween 20 (Sigma), the membranes were incubated overnight at room temperature with the first antibody (antibody for Akt, K-ras or p-Erk, Cell Signaling) diluted in TBS. After washing, the membranes were incubated for 2 h at room temperature with the second antibody (Santa Cruz Biotechnology, CA). Bands were detected with an ECL system (Amersham Pharmacia Biotech K.K., UK).

siRNA-PEI-MSN Exposure and Assessment of PGP Expression**:** Pgp siRNA-PEI-MSN complexes were freshly prepared as described above. The siRNA duplex consists

of 5’-r(CGGAAGGCCUAAUGCCGAA) dTdT (sense) and 5’-r(UUCGGCAUUAGGCCUUCCG) dTdG (antisense) strands. First, 5 μL of 250 ng/μL Pgp siRNA or scrambled siRNA was added to 100 μg of PEI 1.8 kD-MSN (N/P ratio = 80), 100 μg of PEI 10 kD-MSN (N/P ratio = 80), or 12.5 μg of PEI 25 kD-MSN (N/P ratio =10), in 5 μL of aqueous solution. After incubation at room temperature for 30 min, the complexes were stabilized by 1 mg/mL BSA and then transferred into 1 mL of complete DMEM. KB-V1 cells were plated at $2 \times 10^5$ cells per well, then exposed to the complexes for 16 h. After exposure, the medium was replaced with fresh DMEM containing 10% FCS and cultured for a further 56 h. Cells then were harvested for immunoblotting as outlined in the Supporting Information, section S1. A commercially available cationic liposomal transfection agent (Lipofectamine 2000) was used as a positive control. Protein abundance was quantified by densitometric scanning using a laser Personal Densitometer SI and Image Quant software (Amersham Biosciences).

Determination of Intracellular Dox Concentration: Dox uptake in KB-V1 cells was quantitatively evaluated in a microplate reader at 72 h; 5 × 104 cells were placed into a 96-wells plate and treated with 2 μg/mL free Dox or the equivalent amount of drug loaded into MSN before or after PEI coating, with or without attachment of Pgp siRNA. Following the washing of the cells in cold PBS, the intracellular Dox fluorescence was detected at excitation and emission wavelength of 485/550 nm in a microplate reader (SpectraMax M5Microplate Reader, Molecular Device, USA). Moreover, we also captured confocal images at the end of experiment. Image J software (version 1.37c, NIH) was used to analyze the nuclear fluorescence.

Assessment of Cytotoxicity and Apoptosis in KB-V1 Cells Treated with Dox-Loaded Particles in the Absence and Presence of Pgp siRNA: To measure cytotoxicity of the different Dox formulations, KB-V1 cells were treated with free Dox, Dox-MSN, PEI-Dox-MSN, and siRNA-PEI-Dox-MSN, respectively. For the latter two particle types, incubation time was for 16 h before replenishment of the old medium with fresh complete DMEM and performance of a MTS assay at 72 h. On the basis of the absorption readout at 490 nm, the IC50 of free and Dox-loaded MSN were calculated. We also assessed the induction of apoptosis at 72 h through the use of Annexin V-SYTOX Blue. Briefly, $5 \times 10^5$ cells were harvested and stained by FITC-Annexin V- SYTOX Blue working solution (Annexin V, Trevigen; SYTOX Blue, Invitrogen) at room temperature for 15 min. The cells were washed in binding buffer before performance of flow cytometry (Becton Dickinson, Mountain View, CA). Data analysis was performed by BD CellQuest. To confirm the flow data in which there may be a minor overlap of Dox with FITC-Annexin V, a TUNEL detection kit was used according to the manufacturer's instructions to confirm the induction of apoptosis. Briefly, 72 h following treatment with free Dox or Dox-loaded particles, cells were washed, fixed, and permeabilized before TUNEL staining. The number of TUNEL-positive cells was assessed under a fluorescent microscope (200×). At least 3 fields were counted by the same investigator to calculate thepercentage of TUNEL positive cells.

Statistical Analysis: Data represent the mean standard deviation for duplicate or triplicate measurements in each experiment, which was repeated at least three times.

Differences between the mean values were analyzed by two-sided Student's *t* test or one way ANVOA, and results were considered statistically significant at $p < 0.05$.

## 6.6. Figures and Tables

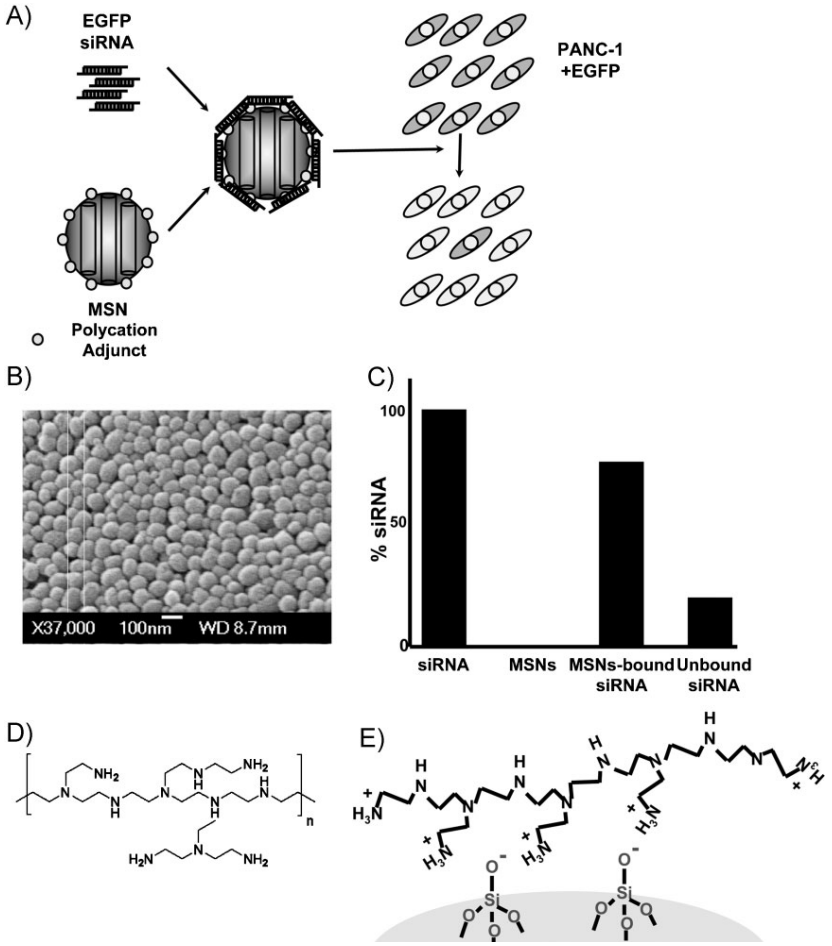


**Figure 6.1.** A) Conceptual diagram of siRNA-mediated EGFP gene silencing utilizing mesoporous silica nanoparticles as delivery vehicles. Polycation adjuncts (i.e., PEI) allow binding between nucleic acids and MSNs. B) Scanning electron microscopy images of the MSNs. C) Quantitative binding assay between PEI-surface-modified MSNs and EGFP siRNA. siRNA and PEI-MSNs were mixed and rotated overnight at 4 8C, and then spun down at 5000 rpm for 1 min to pellet the MSNs. The supernatant containing unbound siRNA is quantified and subtracted from the startingamountofsiRNA to determinethe percentage of siRNAboundto PEI-MSNs.The majority of siRNA remains attached to PEI-MSNs. D) Binding between nanoparticles and siRNA is mediated by an electrostatic interaction between positively charged PEI on the surface of the MSNs and negatively charged siRNA reagents. E) Schematic image of part of the surface of PEI-MSNs.

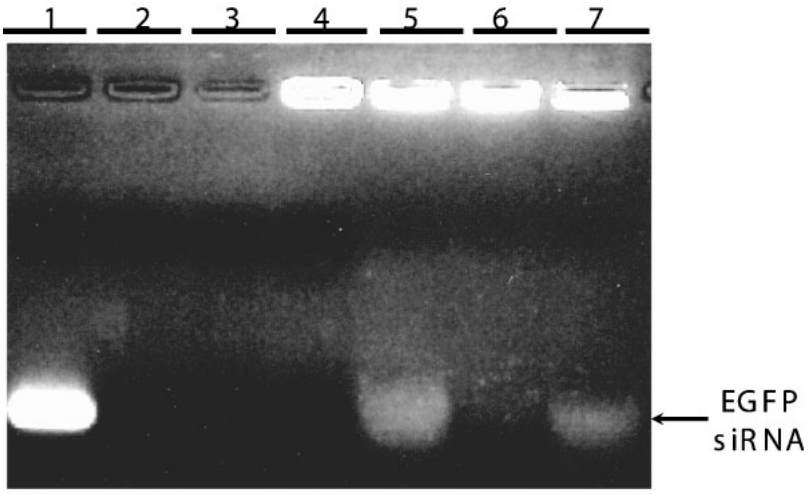


| | |
|---|---|
| Lane 1 | siRNA |
| Lane 2 | siRNA+RNase |
| Lane 3 | MSN+RNase |
| Lane 4 | MSN(siRNA)+RNase |
| Lane 5 | MSN(siRNA)+Hep |
| Lane 6 | MSN(siRNA)+Hep+RNase |
| Lane 7 | MSN(siRNA)+RNase+Hep |

**Figure 6.2.** PEI-MSNs can bind and protect siRNA from cleavage by RNaseA. PEI-MSNs loaded with siRNA are treated with RNase A (Lane 4), or with heparin (Lane 5), or with RNaseA followed by heparin (Lane 7), or heparin followed by RNase A (Lane 6), as described in the Experimental Section. The samples were run on a gel and visualized. Lane 1 shows gel migration of siRNA. In Lane 2, siRNA after RNase A treatment was analyzed by gel electrophoresis. siRNA bound to PEI-MSNs was retained in the gel wells and showed no sign of degradation (Lane 4). PEI-MSNs-bound siRNA was intact following incubation with RNase A and subsequent dissociation by heparin (Lane 7). siRNAdissociated fromPEI-MSNsby heparin isshownin lane 5. On the other hand, siRNA that dissociated from PEI-MSNs by heparin was degraded when exposed to RNase A again (Lane 6).

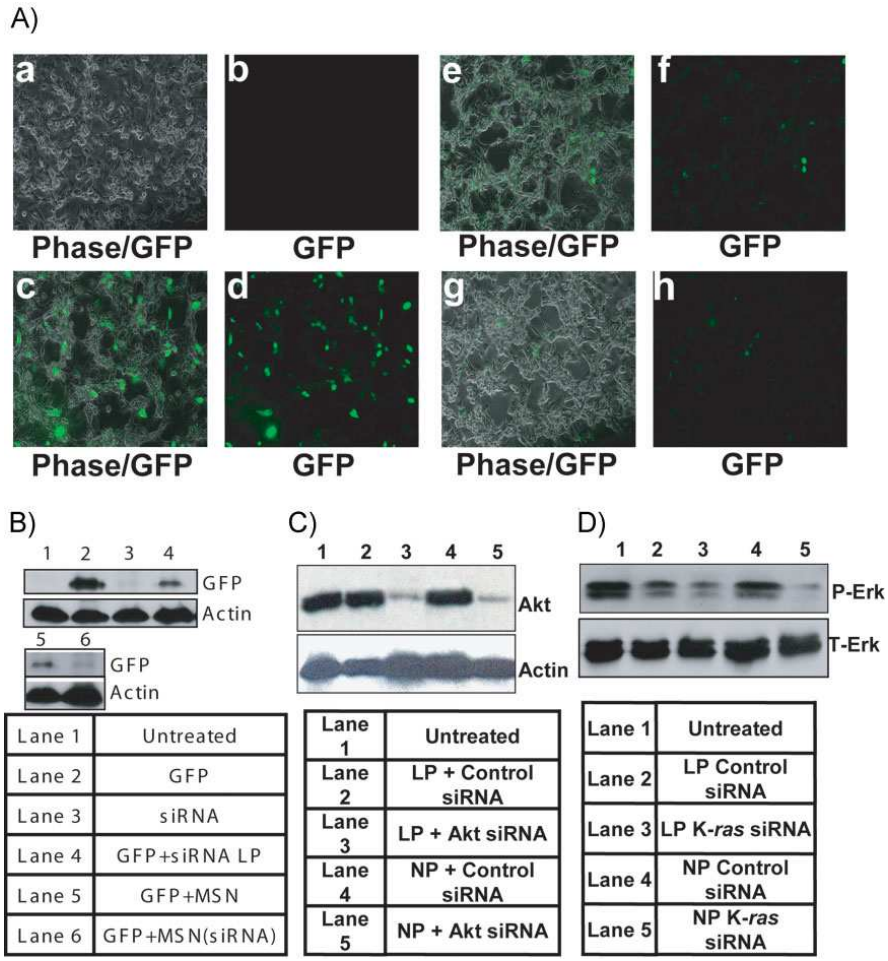


**Figure 6.3.** A) Visualization of PEI-MSN-mediated EGFP silencing with fluorescence microscopy. a,b) Untreated PANC-1 cells as a negative control. c,d) EGFP-expressing PANC-1 Cells. e,f) EGFPexpressing PANC-1 cells transfected with EGFP siRNA by lipofectamine as a positive control. g,h) EGFP-expressing PANC-1 cells treated with EGFP siRNA-loaded PEI-MSNs. Left: phase images;right:fluorescent images. B) Western-blot analysis ofPANC-1cells transfected with GFP and subsequently knocked down with eGFP-specific siRNA delivered by the Lipofectamine 2000 or PEI-MSNs loaded with eGFPsiRNA. C) Western-blot analysis of PANC-1 cells treated with siRNA against Akt delivered by the chemical transfection reagent, Lipofectamine 2000 (Lane 3) or siRNA-loaded PEI-MSNs (Lane 5). Lane 1 shows Akt in untreated cells. Lane 2 shows Akt in cells treated with scrambled siRNA delivered by Lipofectamine. Lane4 shows Akt in cells treated with PEI-MSNs loaded with scrambled siRNA. D) Western-blot analysis of p-Erk in cells treated with siRNA against K-ras delivered by Lipofectamine (Lane 3) or with PEI-MSNs loaded with siRNA against K-ras (Lane 5). Lanes2 and 4 show p-Erk in cells treated with scrambled siRNA delivered by Lipofectamine and PEI-MSNs, respectively.

(A)

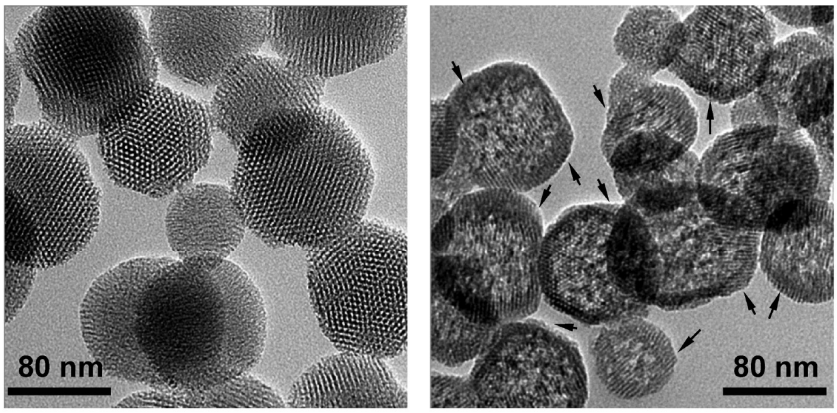


Phos-MSNP PEI-Phos-MSNP

(B)

| MSNP Exterior | Size in $H_2O$ (nm) | Size in BSA (nm) | Size in CDMEM (nm) | Zeta Potential in $H_2O$ / CDMEM (mV) |
|---|---|---|---|---|
| PEI 1.8 kD-MSNP | 1201 | 360 | 294 | +29.5/-4.6 |
| PEI 10 kD-MSNP | 758 | 241 | 261 | +34.1/-3.8 |
| PEI 25 kD-MSNP | 1152 | 247 | 252 | +31.7/-3.7 |

**Figure 6.4.** Physiocochemical characterization of PEI-coated MSN. (A) TEM image of phosphonate-MSN before and after coating with the 10 kD PEI polymer. The arrows indicate that the polymer decorates the MSN surface but leaves the porous interior accessible to drug loading. (B) Particle size and zeta potential in pure water, after stabilization with 1 mg/mL BSA in water, or in DMEM cell culture medium, were measured. None of the size and zeta potential data are not significantly changed when the MSN were loaded with Dox and siRNA.

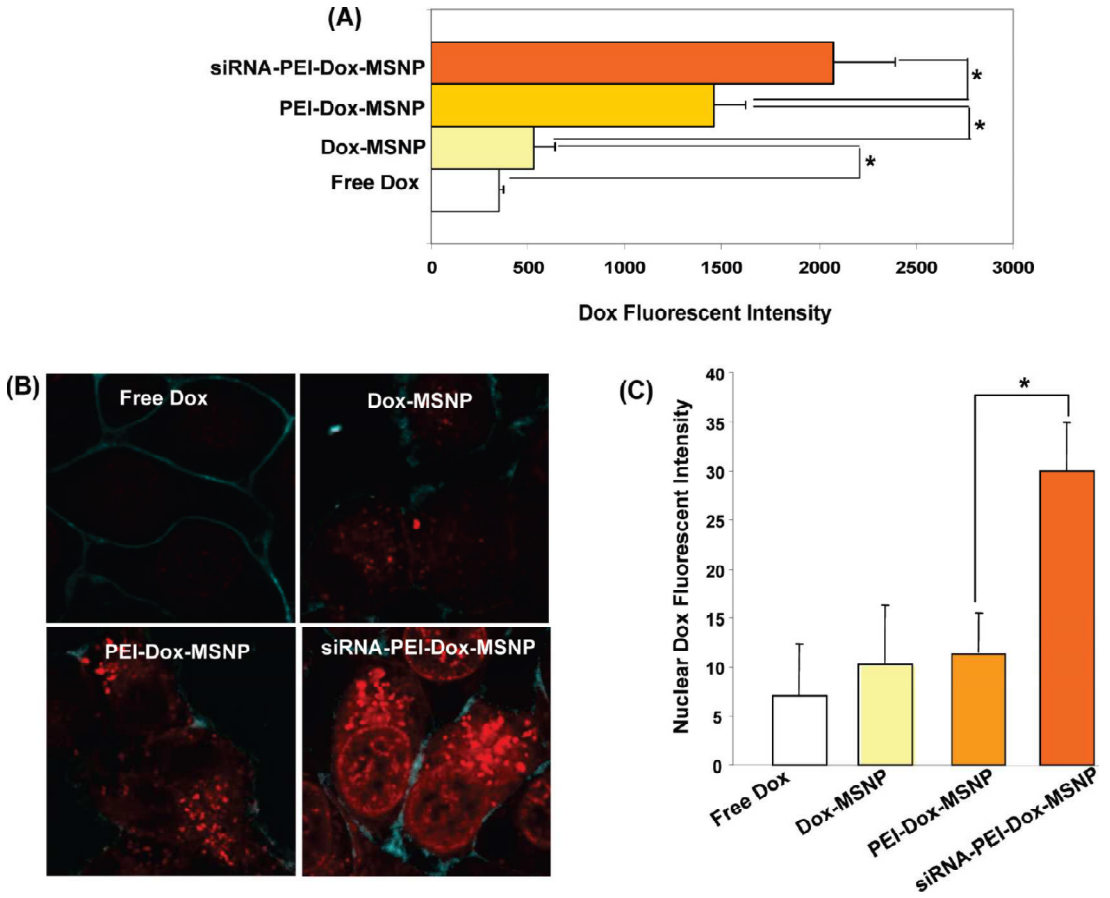


**Figure 6.5.** Simultaneous delivery of Dox and Pgp siRNA to the nucleus leads to a synergistic increase in cellular and nuclear Dox levels in KB-V1 cells. (A) Quantitative comparison of Dox levels using a fluorescent readout of cellular drug levels 72 h after introduction of treatment, using 2 _g/mL free Dox or the equivalent amount of drug loaded into MSN before or after PEI coating or PEI coating followed by the attachment of Pgp siRNA. (B) Confocal images showing drug uptake in KB-V1 cells that treated with 5g/mL free Dox or the equivalent amount of drug loaded into various MSNs for 72 h. Please note that while free Dox could not be maintained intracellularly, Dox delivered by MSN (Dox-MSN) were retained in the particles that localized in the peri-nuclear region. PEI-Dox-MSN significantly enhanced particle uptake compared to the unmodified MSN. However, while much of the drug remained confined to the particles, nuclear staining could be observed when Pgp siRNA was added to this platform. Thus, Pgp knockdown is likely effective at maintaining the Dox that is released from the particles long enough to allow the drug to find its way to the nucleus. The cell membrane was stained by Alexa 633-conjugated WGA (cyan color). Dox staining is in red. (C) Quantitative analysis of the nuclear fluorescence signal in KB-V1 nuclei was performed by the use of Image J software.

## 6.7. References


1. D. Castanotto, J. J. Rossi, *Nature* **2009**, *457*, 426–433.
2. M. Bivas–Benita, S. Romeijn, H. E. Junginger, G. Borchard, Eur. *J. Pharm. Biopharm*. **2004**, *58*, 1–6.
3. O. Boussif, F. Lezoualc'h, M. A. Zanta, M. D. Mergny, D. Scherman, B. Demeneix, J. P. Behr, *Proc. Natl. Acad. Sci. USA* **1995**, *92*, 7297–7301.
4. W. T. Godbey, K. K. Wu, G. J. Hirasaki, A. G. Mikos, *Gene Ther*. **1999**, *6*, 1380–1388.
5. Y. Yamazaki, M. Nango, M. Matsuura, Y. Hasegawa, M. Hasegawa, N. Oku, *Gene Ther*. **2000**, *7*, 1148–1155.
6. R. Kircheis, L. Wightman, E. Wagner, *Adv. Drug Deliv. Rev*. **2001**, *53*, 341–358.
7. J. Lu, M. Liong, J. I. Zink, F. Tamanoi, *Small* **2007**, *3*, 1341–1346.
8. G. Jiang, K. Park, J. Kim, K. S. Kim, S. K. Hahn, *Mol. Pharma*. **2009**, *6*, 727–737.
9. I. Slowing, J. L. Vivero-Escoto, C. W. Wu, V. S. Lin, *Adv. Drug Deliv. Rev*. **2008**, *60*, 1278–1288.
10. F. Torney, B. G. Trewyn, V. S.-Y. Lin, K. Wang, *Nat. Nanotechnol*.**2007**, *2*, 295–300.
11. T. Xia, M. Kovochich, M. Liong, H. Meng, S. Kabehie, S. George, J. I. Zink, A. E. Nel, *ACS Nano* **2009**, *3*, 3273–3286.
12. M. M. Gottesman, Mechanisms of Cancer Drug Resistance. *Annu. Rev. Med.* **2002**, *53*, 615–627.

13. G. Szakacs, J. K. Paterson, J. A. Ludwig, C. Booth-Genthe, M. M. Gottesman, Targeting Multidrug Resistance in Cancer. *Nat. Rev. Drug Discovery* **2006**, *5*, 219–234.
14. L. S. Jabr-Milane, L. E. van Vlerken, S. Yadav, M. M. Amiji, Multifunctional Nanocarriers to Overcome Tumor Drug Resistance. *Cancer Treat. Rev.* **2008**, *34*, 592–602.
15. D. V. Svintradze, G. M. Mrevlishvili, Int. *J. Biol. Macromol*. **2005**, *37*, 283–286.
16. N. Weber, P. Ortega, M. I. Clemente, D. Shcharbin, M. Bryszewska, F. J. de la Mata, R. Gomez, M. A. Munoz-Fernandez, *J. Controlled Release* **2008**, *132*, 55–64.
17. J. A. Engelman, Nat. Rev. *Cancer* **2009**, *9*, 550–562.
18. A. R. He, A. P. Lindenberg, J. L. Marshall, Exp. Rev. Anticanc. Ther. 2008, 8, 1331–1338.
19. J. Lu, M. Liong, S. Sherman, T. Xia, M. Kovochich, A. Nel, J. Zink, F. Tamanoi, *NanoBioTechnology* **2007**, *3*, 89–95.

# Chapter 7

## *In Vivo* Tumor Suppression Efficacy of Mesoporous Silica Nanoparticle-Based Drug Delivery System

## 7.1. Abstract

Mesoporous silica nanoparticles (MSNs) are a promising material for drug delivery. In this chapter, the drug delivery capability of MSNs is demonstrated by following tumor growth in mice treated with camptothecin-loaded MSNs. These results indicate that MSNs are biocompatible, preferential accumulate in tumors, and effectively deliver drugs to the tumors and suppress tumor growth. Dramatic improvement of the potency of tumor suppression was obtained by surface modifying MSNs with folic acid. Dose dependent tumor suppression was observed establishing 0.5 mg of CPT-loaded MSNs per mouse as a minimum dose sufficient for achieving complete tumor growth inhibition. Renal excretion of MSNs was also confirmed with TEM imaging. These findings highlight attractive features: biocompatibility, renal clearance and tumor-suppressing ability of MSNs as a drug delivery system. The biological experiments described in this chapter were performed by Dr. Jie Lu at UCLA.

## 7.2. Introduction

We and other groups have shown that MSNs could be used as drug-delivery vehicles, gene-transfection agents, cell markers, and carriers of molecules.[1-12] Conjugation with specific ligands or antibodies, such as folic acid, allows the targeting of nanoparticles to special cell types, such as cancer cells. In our previous studies, we have successfully incorporated a representative hydrophobic anticancer drug, camptothecin (CPT), into the pores of MSNs and delivered the drug to a variety of human cancer cells to induce cell death. These results suggest that the mesoporous silica nanoparticles can be used as a vehicle to overcome the insolubility problem of many anticancer drugs.[1, 13, 14]

Many studies also showed the biocompatibility of MSNs *in vitro* with culture cells as well as *in vivo* with animals.[14-18]

The most important question regarding the use of mesoporous silica nanoparticles as a drug delivery vehicle for cancer therapy is examining its success for delivering anticancer drugs to tumors and suppressing their growth in animal study. Although there are many cell studies demonstrating that MSNs are very promising materials for drug delivery in tissue culture cells, there are few studies that extended the success of *in vitro* studies to animal settings. The versatility of MSNs promises a new drug delivery vehicle with better blood circulation times, biocompatibility and clearance from the animal body,[14, 19] which envisions promising nanomaterials for future clinical application. We were the first to demonstrate, in our previous study, that MSNs are very effective for antitumor drug delivery and that the tumor suppression was significant with a subcutaneous human breast cancer xenograft in mice.[14] In that study, the subcutaneous tumors in mice were virtually eliminated by treating with CPT-loaded MSNs or CPT-loaded folate-modified MSNs (FMSNs), proving that the high drug-loading ability, low toxicity, and tumor-accumulating effect of MSNs provide a promising drug-delivery vehicle for cancer therapy. However, much more work is needed. It is important to examine whether MSNs are capable of suppressing tumor types other than breast cancer. It is also important to employ different administration conditions as well as to optimize the dosages of MSN administration in animal. We also wanted to further examine the effects of targeting MSNs.

In this chapter, animal tumor studies of MSNs on breast cancer and pancreatic cancer xenografts will be presented. It will be shown that CPT-loaded MSNs and folic acid-conjugated MSNs (FMSN) (folate receptor-targeting) (Figure 7.1) exhibit significant tumor suppression effects. Different dosages were also examined to obtain dose dependent inhibition of tumor growth. In the present study, we also addressed our previous preliminary observation that MSNs are excreted. We show that MSNs excreted in the urine have similar features to those injected including their size.

## 7.3. Results and Discussion

### 7.3.1. *In vivo* tumor suppressing effect of drug-loaded FMSNs

Thirty nude mice with established xenografts of human breast cancer cell MCF-7 were randomly divided to 5 groups, and the intraperitoneal injections were started when the average tumor diameter reached 3 mm (14th day after inoculation). Animals in the first group received saline solution as control. Group 2 was treated with camptothecin dissolved in DMSO and diluted in saline. Group 3 was treated with plain FMSNs without loading. Group 4 was treated with FMSNs loaded with CPT (the final concentration of CPT is the same as group 2). Group 5 was treated with F-FMSNs loaded with CPT. All injections were done twice per week until the end of the experiment (the $68^{th}$ day). Each mouse was injected 18 times in total. The average body weights are shown in Figure 7.2A. Only one mouse in group 2 exhibited severe toxicity at the 45th day, manifested by shivering, inactivity, severe necrosis of the tail, ataxic gait and sudden drop of body weight (approximate 16.3 g). 50 mg/ml Amoxicillin (amoxil drop, Pfizer Inc) was

administered in the drinking water, but no improvement was observed after 3 days. This mouse was therefore euthanized on the 51st day.

As shown in Figure 7.2B, the tumors in the control group (group 1) and FMSNs-treated group (group 3) kept growing, showing a fast growing period after the inoculation of 17β-estradiol pellet on the 31st day. No significant difference of average tumor volumes was observed between these two groups, suggesting FMSNs themselves did not affect the tumor growth in mice. Inhibition of tumor growth was significant in the CPT-treated group (group 2). At the end of this experiment (the 68th day), administration of CPT suppressed the tumors to approximately 14% of control, suggesting that it is effective tumor-suppressing agent when dissolved in DMSO. However, from day 48, the average tumor volumes in groups treated with CPT-loaded FMSN or CPT-loaded F-FMSN (group 4 and 5) continuously declined, showing faster tumor-shrinking effects. On the 62nd day, no obvious subcutaneous tumors were visible (Figure 7.2B, C).

The results of the histopathological examination of mice's organs and the hematology and serology examinations are summarized in Supporting Information Table 3. Mild subacute splenomegaly, hepatomegaly, bilateral renomegaly and cardiomegaly, based on percentage of body weight, were observed in all surviving mice, which are common and non-specific findings in nude mice. Mild to moderate lymphoid hyperplasia and moderate chronic bilateral adrenal capsular fibrosis were also detected in all mice except the control mice. In addition, mildly elevated hematocrite was also seen in all mice. The blood test from mice of group 2 (CPT treated mice) showed moderately to severely elevated liver enzymes (ALT, AST), moderate to severe hypoalbuminemia and

hypoproteinemia, mildly elevated creatinine kinase as well as mildly to moderately decreased levels of calcium and phosphorus. Group 3 (treated with FMSN alone) only showed mildly elevated ALT and AST. In the groups 4 and 5 (treated with FMSN-loaded CPT and F-FMSN-loaded CPT, respectively), severely or mildly to moderately elevated liver enzymes (ALT, AST) were detected.

### 7.3.2. Biocompatibility and excretion of MSNs in the urine

We have shown previously that MSNs prepared above are biocompatible and that they are excreted efficiently after administration into mice.[14] In that study using nude mice, we found that a majority of MSNs injected into the mice bodies was excreted through urine within four days by measuring Si concentration in the urines with inductively coupled plasma optical emission spectrometry (ICP-OES).[14] This feature of MSNs is important in designing tumor suppression experiments in mice, as their excretion can influence the schedule of MSN administration. Therefore, we addressed this excretion issue by examining the concentration of Si in the urine again, but with regular mice this time. A total of 1 mg of MSN or FMSN was injected into three mice for each kind of particle, which corresponds to ≈465 μg of Si. Urine and feces were collected into separate collection tubes before and after the injections at different time points as described in the methods for ICP analysis of Si concentrations. As shown in Figure 7.3B, within the first 24 h after injection, approximately 58 μg of Si was detected in urine of the MSN-injected mice, and 73 μg in the FMSN-injected mice. In the second day, 40 μg and 42 μg of Si was detected in the urine of MSN and FMSN injected mice, respectively. Figure 7.3A shows cumulative amount of Si detected. The renal excretion decreased in

the following days. Within 6 days, approximately 360 μg and 350 μg of Si were detected in the urine and feces from MSN and FMSNinjected mice respectively (Figure 7.3). A part of the urine was examined with electron microscope to confirm that the Si detected represents that of intact silica nanoparticles, not from broken pieces. As shown in Figure 7.3C, MSNs were detected in the urine and the nanoparticles recovered had the same size as that of injected nanoparticles. Pores were clearly recognizable, suggesting the urine excretion of intact nanoparticles. Thus, it appears that MSNs can be excreted within a week after their administration. Taken together with our previous results, it appears that the majority of MSNs administered into mice can be excreted. This led us to conclude that twice per week administration of MSNs should provide effective means of delivering anticancer drugs.

### 7.3.3. Tumor suppressing effect of CPT-loaded MSNs on PANC-1 xenograft in nude mice

To examine the ability of MSNs to deliver anticancer drugs and to suppress tumor growth in mice, we used camptothecin (CPT)-loaded MSN as well as CPT-loaded folate modified MSN (FMSN) on human pancreatic cancer xenografts (PANC-1) established on nude mice. The amount of CPT-loaded MSN was determined based on our previous experiments.[14] In that study, we examined acute and long term toxicity profiling of MSN and FMSN in mice, and determined that 1 mg per mouse per day is the highest dosage that can be injected into mice safely without inducing any toxicity to the animals. And this concentration of both CPT-loaded MSN and FMSN was proved to be able to completely eliminate the subcutaneous breast tumors in that study. In addition, in our

previous *in vitro* studies, we observed similar cell-killing effects of CPT-loaded MSN and FMSN on human breast cancer and pancreatic cancer cell lines. Therefore, we decided to test the tumor suppressing effect of CPT-loaded MSN and FMSN with the concentration of 1 mg per mouse.

25 nude mice with established xenografts (described in Methods) of human pancreatic cancer cells PANC-1 were randomly divided into 5 groups (n = 5) and intraperitoneal injections were started when the average tumor diameter reached 3 mm (14th day after inoculation). Animals in the first group received saline solution as a control. Group 2 was treated with camptothecin dissolved in dimethyl sulfoxide (DMSO) and diluted in saline. Group 3 was treated with empty MSNs without loading. Group 4 was treated with MSNs loaded with CPT (the final concentration of CPT is the same as group 2). Group 5 was treated with folate-modified MSNs (FMSNs) loaded with CPT. Injections were performed twice per week until the end of the experiment (the 52nd day). Each mouse was injected 12 times in total. The average body weights are shown in Figure 7.4A. No obvious body weight loss was observed in all the treated mice compared with the control mice group. Untill the end of injections, no mouse showed severe toxicity, defined by shivering, inactivity, severe necrosis of the tail, ataxic gait, or sudden drop of body weight.

As shown in Figure 7.4B, the tumors in the control group (group 1) and in the empty MSN-treated group (group 3) kept growing, showing a fast growing pattern, ending up with big tumors (average tumor volumes are approximately 500-550 $mm^3$ at the 52nd day). No significant difference in average tumor volumes was observed between

these two groups, confirming again that MSNs themselves do not affect the tumor growth in mice. On the other hand, the administration of CPT-loaded MSN (group 4) showed a significantly slower tumor growth, ending up with much smaller tumors (approximately 250 $mm^3$ in average at the 52nd day). Noticeably, the tumors in the group 5 (CPT-loaded FMSN) stop growing from the 24th day, remaining relatively smaller tumors within the whole treatment period, ending up with a very small tumors at the end of experiment (90 $mm^3$ in average). 4 out of 5 tumors in this group are almost completely eliminated at the end (Figure 7.4C). In the group 3 (CPT treated mice), the average tumor volumes are not significantly different from the control group, only showing a slightly smaller average tumor volumes at the end of experiment, as shown in Figure 7.4B. This was due to a variation of tumor volumes in this group; although 4 out of 5 tumors in this group showed smaller volume, there is one unusually big tumor in one mouse.

### 7.3.4. Tumor suppressing effect of CPT-loaded MSNs/FMSNs on MiaPaca-2 xenograft in nude mice

In the next experiment, we used a different pancreatic cancer cell line. The tumors are established with cultured MiaPaca-2 cells on nude mice as described in Methods. 7 days after the inoculation, palpable tumors on all mice reached 2-3 mm in diameter, therefore the treatments were started in a manner similar to that described above for PANC-1 xenografts. The body weight of all mice showed similar increase and no obvious body weight loss was observed as shown in Figure 7.5A, and all mice were active during the entire period.

As shown in Figure 7.5B, the tumors in the control and MSN groups showed a slow but stable growth. CPT treatment inhibited the tumor growth slightly with this xenograft model, reducing the tumor volume to approximately 60% of the control. Dramatically, the CPT-loaded MSNs showed a swift inhibition of the tumor growth. After only one week of the treatment, the tumors in this group were shrunk significantly. By the end of experiment (the 25th day), the tumors were barely palpable, having an average tumor volume of approximately 60 $mm^3$, comparing to 200 $mm^3$ in the control group. Even more significantly, the tumors in CPT-loaded FMSN treated group disappeared after 11 days of injection (4 times of injections). 4 out of 5 mice in this group did not bear visible tumors any longer at the end of experiment, and the 5th mouse showed a very tiny subcutaneous tumor only (approximately 1 mm in diameter). Figure 7.5C shows representative pictures of mice in each group at treatments.

### 7.3.5. Dose-dependent tumor-suppressing effects of CPT-loaded FMSNs with SCID mice

The above experiments showed that MSNs loaded with CPT can suppress growth of xenografts tumors from 3 different human cancer cell lines. Among them, the MiaPaca-2 xenograft showed most drastic tumor shrinking effect. For these three experiments, we applied the highest dosages of MSNs that are possible and safe for the animals. It is therefore logical to determine the optimal dosage that will be similarly effective, hence less stress and burden to the animals. And also to vary the experiment, we tested SCID mice for this experiment instead of nude mice. 25 shaved SCID mice were subcutaneously transplanted with $1\times10^7$ MiaPaca-2 culture cells. 14 days after the

inoculation, palpable tumors on all mice reached 2-3 mm in diameter, and then the mice were divided into 5 groups and the treatments were started. Mice in group 1 (control) received injection of saline solution as described above. Group 2 mice received 1 mg CPT-loaded FMSN per mouse per injection (0.2 mL, 5 mg $mL^{-1}$, the final concentration of CPT was ≈7.8 μM). Group 3 mice were injected with 0.5 mg CPT-loaded FMSN per mouse per injection (0.2 mL, 2.5 mg $mL^{-1}$, the final concentration of CPT was ≈3.9 μM). Group 4 mice were injected with 0.25 mg CPT-loaded FMSN per mouse per injection (0.2 mL, 1.25 mg $mL^{-1}$, the final concentration of CPT was ≈1.9 μM). Group 5 mice were injected with 0.125 mg CPT-loaded FMSN per mouse per injection (0.2 mL, 0.6 mg $mL^{-1}$, the final concentration of CPT was ≈0.9 μM). All injections were through intraperitoneal and twice per week. As shown in Figure 7.6A, the dosages used did not alter the body weight gain of all mice.

The MiaPaca-2 xenografts in SCID grew much slower than those in nude mice and also responded to CPT-loaded MSNs slower (Figure 7.6B). The tumor-suppressing effects appeared only after the 39th day (treated for 25 days, 8 injections). As expected, 1 mg of CPT-FMSNs completely inhibited the tumor growth at the end of the experiment (the 57th day). The same suppression effect was achieved in the group treated with 0.5 mg/mouse. Further reducing dosage to 0.125 mg resulted in weaker suppression of tumor growth, final average tumor volume in this group being the middle of the control and 0.5 mg group, suggesting a dose-dependent response. A large deviation of tumor volumes in the group treated with 0.25 mg was observed; 2 out of 5 mice in this group bearing

unusual large tumors. Overall, these results show that FMSNs loaded with CPT are effective in blocking growth of pancreatic tumor in SCID mice.

## 7.4. Conclusions

In the present study, we have shown that CPT-loaded MSNs are effective in suppressing tumor growth of a human breast cancer xenograft, MCF-7 and two different human pancreatic cancer xenografts, PANC-1 and MiaPaCa-2. In addition, we used two different animal species, nude mice and SCID mice. The growth of PANC-1 tumors in the nude mice treated with CPT-loaded MSNs was significantly suppressed, ending up with very small tumors or almost complete elimination at the end of the treatment. With MiaPaCa-2 xenografts in nude mice, we observed regression of the tumor only one week after the treatment and the tumor was completely eliminated by the end of the treatment.

Our work also confirmed and extended our intriguing observation that MSNs are excreted. This phenomenon is confirmed in the present study. The clear TEM images of MSNs in the urine solidify this excretion. The MSNs are excreted through urine without breakdown or degradation. He *et al.* reported that MSNs with sizes of ≈ 45 nm were safely excreted through the renal route.[19] Further work is needed to understand the mechanism of excretion through kidney. However, it can be pointed out that our observations suggesting that the MSNs can be cleared from the animal body reinforces the idea that MSNs can be used safely to suppress tumor growth.

Our findings provide compelling evidence of FMSNs' superior biocompatibility at concentrations adequate for pharmacological applications, capability of reducing adverse side effect of anticancer drugs, quick renal clearance, and excellent

tumor-suppressing effect with anticancer loading. And lower concentration even showed similar encouraging results. These point to the features of MSNs as a promising drug delivery system for cancer therapy.

## 7.5. Experimental

Synthesis of mesoporous silica nanoparticles MSNs were synthesized by first dissolving FITC (5.5 mg) in absolute ethanol (3 mL) before adding aminopropyltriethoxysilane (APTS; 12 μL). In another container, cetyltrimethylammonium bromide (CTAB; 0.5 g) was dissolved in a solution of distilled water (240 mL) and sodium hydroxide (2 M, 1.75 mL) that was heated to 80 °C and stirred vigorously. The FITC/APTS solution was stirred under an inert atmosphere for 2 h before adding tetraethylorthosilicate (TEOS; 2.5 mL). Once the temperature of the CTAB solution had stabilized, the ethanol solution containing TEOS and FITC/APTS was added. After 15 min, 0.63 mL 3-trihydroxysilylpropyl methylphosphonate was slowly added to the mixture. After 2 h, the solution was cooled to room temperature and the particles were filtered and washed with methanol using a fritted funnel. The particles were allowed to dry at room temperature overnight. To remove the surfactants from the pores of the particles, particles (850 mg) were dissolved in a solution of methanol (90 mL) and hydrochloric acid (12.1 M, 5 mL) and refluxed for 24 h. The particles were then filtered and washed thoroughly to remove the surfactants and unbound FITC.

*Synthesis of folic-acid-conjugated FMSNs and drug loading:* To attach folic acid to MSNs, 20 mg of particles were washed with and resuspended in DMSO. In a flask, folic

acid (0.1 mg, Sigma, 98%) and APTS (0.05 μL) were mixed in DMSO (1 mL). N-hydroxysuccinimide (0.03 mg, Aldrich, 98%) and 1-(3-dimethylaminopropyl)-3-ethylcarbodiimide hydrochloride (0.05 mg, Alfa Aesar, 98%) was then added into the mixture and stirred for 2 h. In a separate flask containing toluene (4 mL) and the MSNs–DMSO suspension, the folate/APTS solution was added and the mixture was stirred for 20 h at room temperature. The materials were recovered by centrifugation, washed twice with toluene, and dried under vacuum. To load camptothecin (CPT; Sigma, 95%), 10 mg of the particles were suspended in a solution of drugs (1 mg) and DMSO (0.25 mL) for 4 h. After centrifuging the drug-loaded FMSNs from the suspension and removing the supernatant completely, the materials were dried under vacuum. The drug-loaded FMSNs were then washed and sonicated with water before being resuspended in aqueous solution. In order to determine the amount of drugs inside the FMSNs, the aqueous drug-loaded FMSN suspension was incubated at 4 °C for 6 h before centrifugation to show that the drugs were not being slowly released from the mesopores. The resulting supernatant was mixed with the previous supernatant solution from the washing process and measured by UV/Vis absorption spectroscopy. The pellet of drug-loaded FMSNs was resuspended and sonicated in DMSO and collected by centrifugation. The process was repeated two more times (≈15 min, total time) to ensure that the drugs were completely removed from the pores. The DMSO (or methanol) supernatants were then measured using UV/Vis absorption.

*Cells and culture:* The human pancreatic cancer cell lines, PANC-1 and MiaPaca-2, obtained from American Type Culture Collection, were maintained in DMEM supplemented with fetal calf serum (10%, Sigma, MO), Lglutamine (2%), penicillin (1%), and streptomycin (1%). The medium was routinely changed every 3d and the cells were separated by trypsinization before reaching confluency.

*Animals:* All animal experiments were performed following the protocols approved by the UCLA Animal Research Committee. Six-week-old female BALB/c regular or BALB/cAnNCrj-nu nude, or NOD/nCrCrl-Prkdc SCID (Severe combined immunodeficiency) mice (purchased from Charles River Laboratories) were maintained in disposable plastic cages with hardwood chips bedding in an air-conditioned room with a 12-h-light–12-h-dark cycle and given food (oriental CRF-1) irradiated with 30 Gy rays and filtered tap water ad libitum.

*Human cancer xenograph establishment:* For xenografts established from cultured cells, 1 × 107 human pancreatic cancer cells, MiaPaca-2, collected in ice cold DMEM (0.2 mL) containing 50% Matrigel (BioScience), were s.c. injected into the right lateral abdominal wall of the nude mice. Mice were then randomly divided into treatment or vehicle groups after tumors of ≈3 mm in diameter were palpable. For PANC-1 xenograft establishing, the culture cell transplantation in nude mice did not produce reliable subcutaneous tumor in our first trial, therefore, 3 mice were firstly inoculated with 1 × 107 PANC-1 cells subcutaneously. 1 month later, all tumors were removed, washed with PBS, cut into small

tumor chunks from the margins of tumors with similar size, randomly transplanted subcutaneously into the right side of back of other immunity compromised mice. Mice were then randomly divided into treatment or vehicle groups after tumors of ≈3 mm in diameter were palpable. For each experiment, thirty mice with the above-mentioned established xenografts were randomly divided into 5 groups. Animals in group 1 received injection of saline solution (0.2 mL, 0.9%) through intraperitoneal. Animals in group 2 received i.p. injection of CPT (0.2 mL, 7.8 μM, dissolved in DMSO, and then diluted in saline to achieve the final concentration; the final concentration of DMSO was <1.5%). Animals in group 3 received i.p. injection of MSNs (0.2 mL, mg mL−1). Animals in group 4 received i.p. injection of MSNs loaded with CPT (0.2 mL, 5 mg mL−1, the final concentration of CPT was ≈7.8 μM). Animals in group 5 received i.p. injection of folic-acidconjugated MSNs (FMSNs) loaded with CPT (0.2 mL, 5 mg mL−1). All injections were done twice per week from the right lower corner of the abdomen until the end of the experiment. The tumor volume and body weight were monitored every other day and the tumor volume was calculated using the following formula: tumor volume=4π/3·LW2/8 where L is the length and W is the width of the tumor. On the final day, all mice were sacrificed and subjected to autopsy.

*Measurement of MSN excretion in urine:* To examine the excretion of MSN from urine and feces, special single-mouse metabolic cages (Tecniplast) were used. Six regular mice were housed in the metabolic cages. 0.5 mg of MSNs or FMSNs were i.p. injected into the mice. Urine and feces were collected into separate collection tubes before and after

the injections at different time points. The collected urine were sent to the molecular instrumentation center at UCLA for ICP analysis of Si, and also subjected to TEM imaging examination.

## 7.6. Figures and Tables

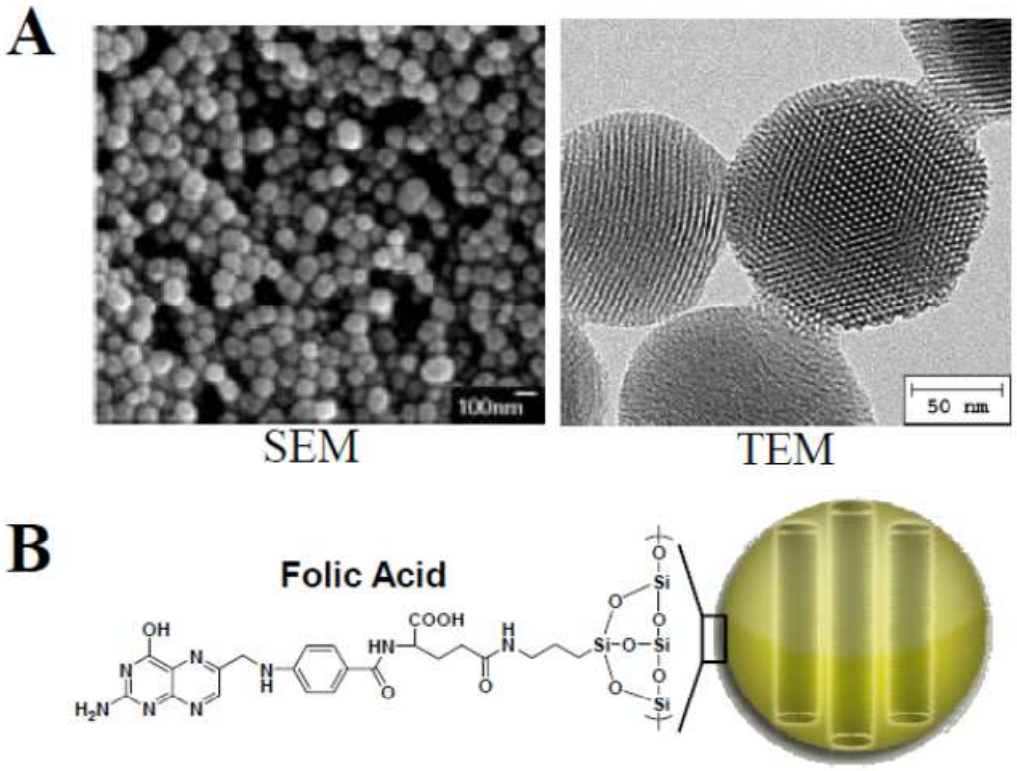


**Figure 7.1.** Characterization of MSN. A) Scanning electron microscope (left) and transmission electron microscope (right) images of FMSN. B) Schematic illustration of MSNs modified with folic acid targeting ligands on the surface.

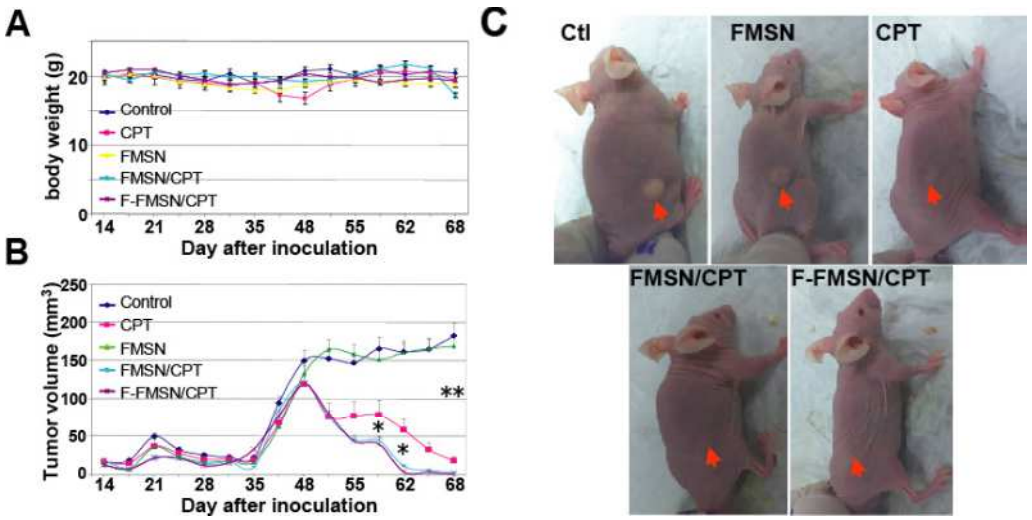


**Figure 7.2.** Antitumor effects of mesoporous silica nanoparticles loaded with Camptothecin in mice. Thirty nude mice with xenografts of human breast cancer cell MCF-7 were divided to 5 groups (n=6), and the intraperitoneal injections were started from the 14th day after inoculation. Animals were injected with either saline solution as control, or camptothecin (CPT), or FMSNs without loading (FMSN), or FMSNs loaded with CPT (FMSN/CPT), or FFMSNs loaded with CPT (F-FMSN/CPT), respectively, twice per week until the end of the Submitted to experiment (the 68th day). **A.** The average body weights are shown as means ± the standard deviation (SD). One mouse in the CPT-treated group was euthanized on the 51st day due to manifestation of severe toxicity. **B.** The average tumor volumes are shown as means ± the standard deviation (SD). *, p value < 0.05; **, P value < 0.01. **C.** Representative images of mice from different groups. Red arrows indicate the location of subcutaneous tumors.

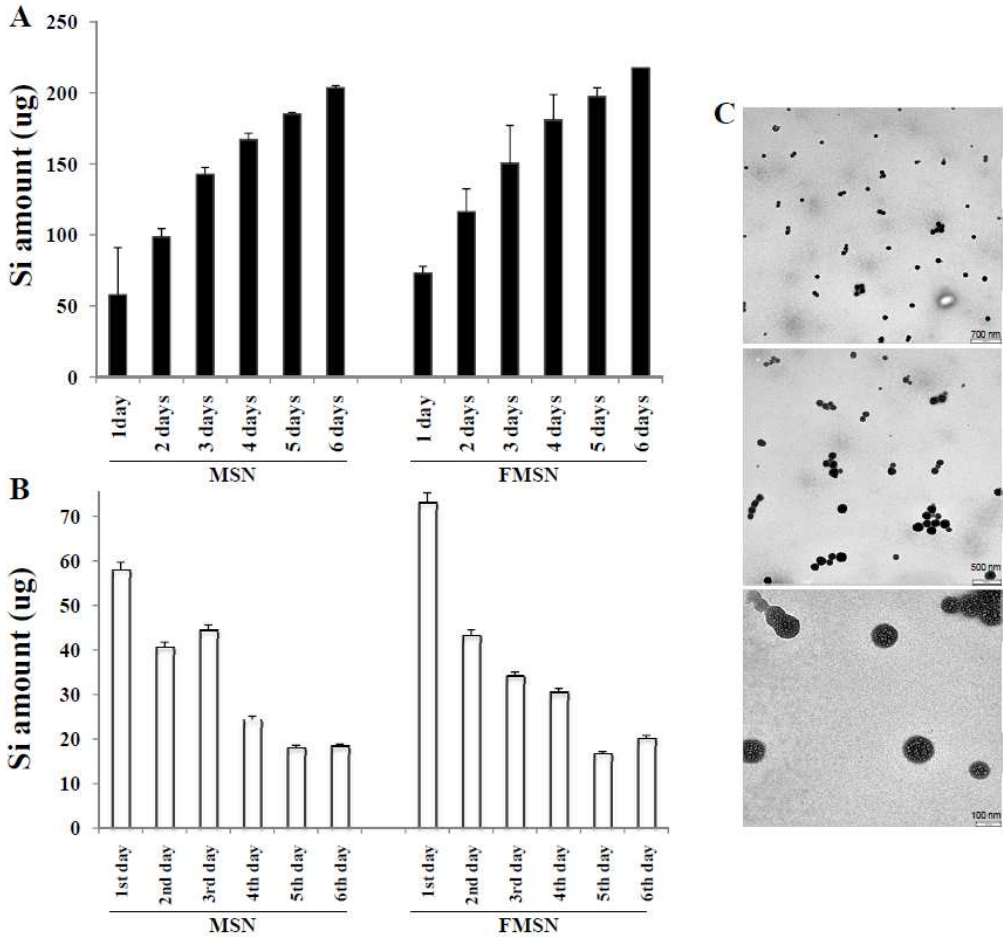


**Figure 7.3.** ICP-OES analysis of the Si concentration in urine of mice collected after injection of MSNs. A total of 1 mg of MSNs or FMSNs was injected into three mice for each kind of particle, which corresponds to ≈465 μg of Si. Urines were collected before and after the injections at different time points for ICP analysis of Si concentrations. The amount of Si in urines in each single day is shown in (B) and the total cumulative amount is shown in (A). TEM examination of the nanoparticles in urine smear confirmed the shape and size of MSNs or FMSNs (C).

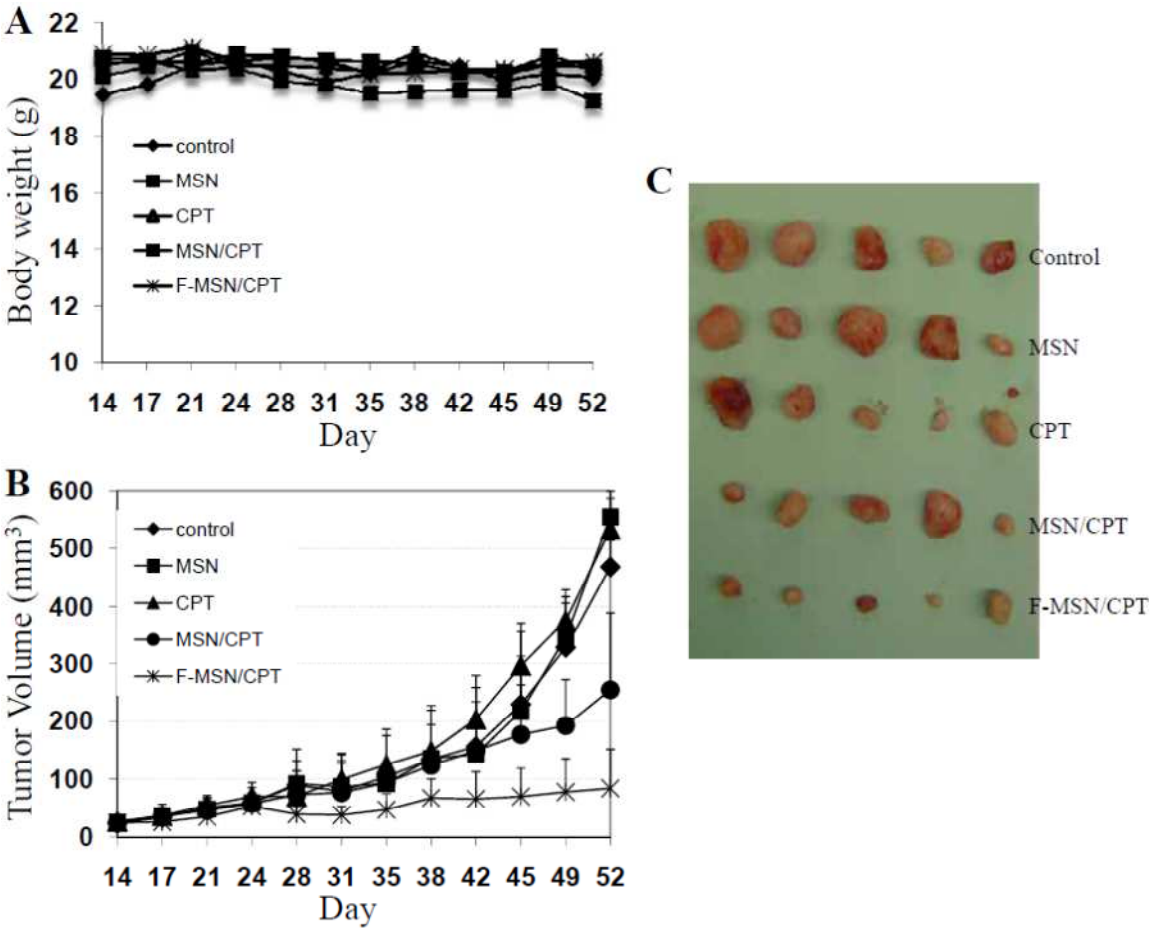


**Figure 7.4.** Antitumor effects of CPT-loaded MSNs and FMSNs on human pancreatic cancer PANC-1 xenograft on nude mice. 25 nude mice with established xenografts of human pancreatic cancer cells PANC-1 were randomly divided into 5 groups (n = 5) and intraperitoneal injections were started when the average tumor diameter reached 3 mm (14th day after inoculation). Animals in the first group received saline solution as a control (control). Group 2 was treated with camptothecin dissolved in dimethyl sulfoxide (DMSO) and diluted in saline (CPT). Group 3 was treated with empty MSNs without loading (MSN). Group 4 was treated with MSNs loaded with CPT (the final concentration of CPT is the same as group 2) (MSN/CPT). Group 5 was treated with folate-modified MSNs (FMSNs) loaded with CPT (F-MSN/CPT). Injections were performed twice per week until the end of the experiment (the 52nd day). Each mouse was injected 12 times in total. A) Average body weights are shown. B) The average tumor volumes are shown as means ± SD. C) Images of subcutaneous tumors collected at the end of experiment.

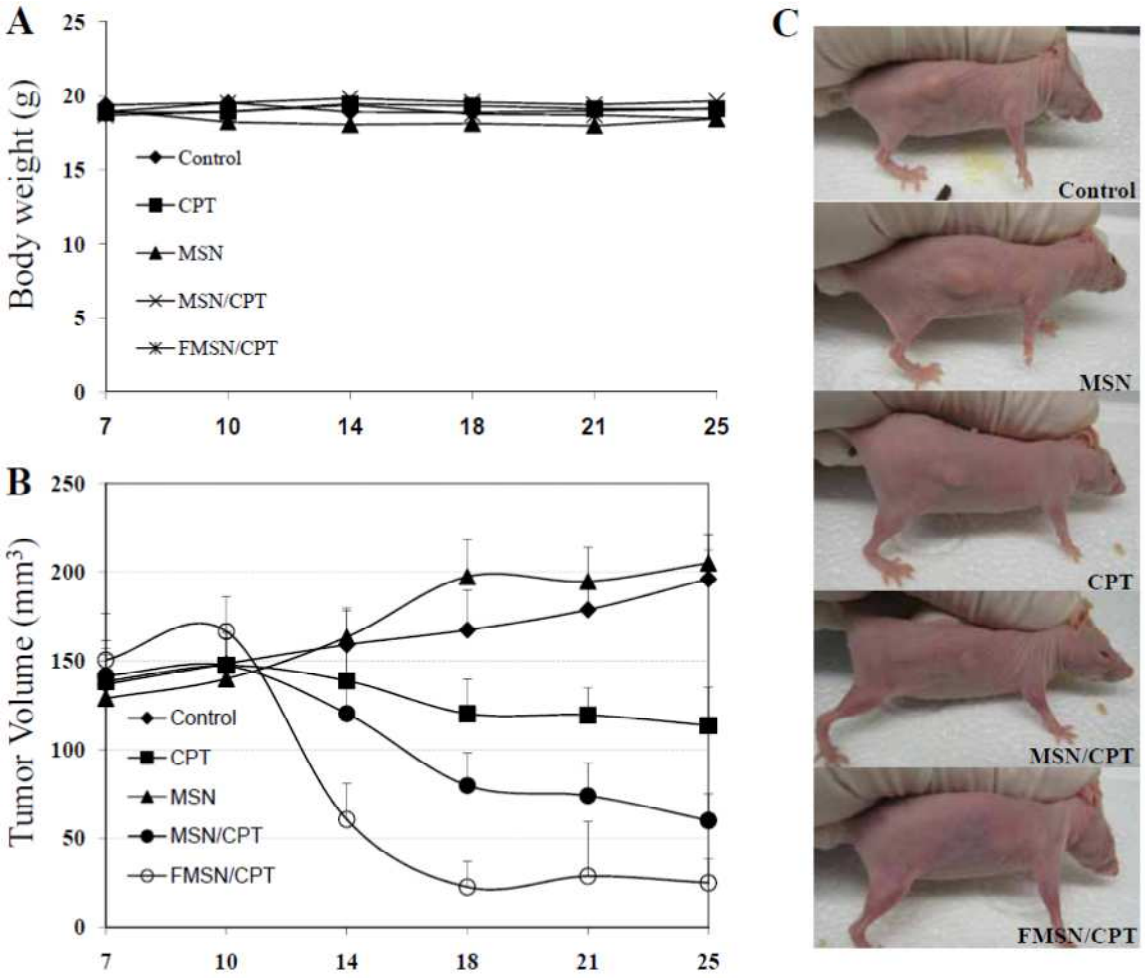


**Figure 7.5.** A human pancreatic cancer cell line, MiaPaca-2, was used for xenograft establishment on nude mice. 7 days after the inoculation when palpable tumors on all mice reached 2-3 mm in diameter, the treatments were started in a similar manner to that with PANC-1 xenografts. A) Average body weights are shown. B) The average tumor volumes are shown as means ± SD. C) Images of representative nude mice with subcutaneous tumors at the last day of experiment are shown.

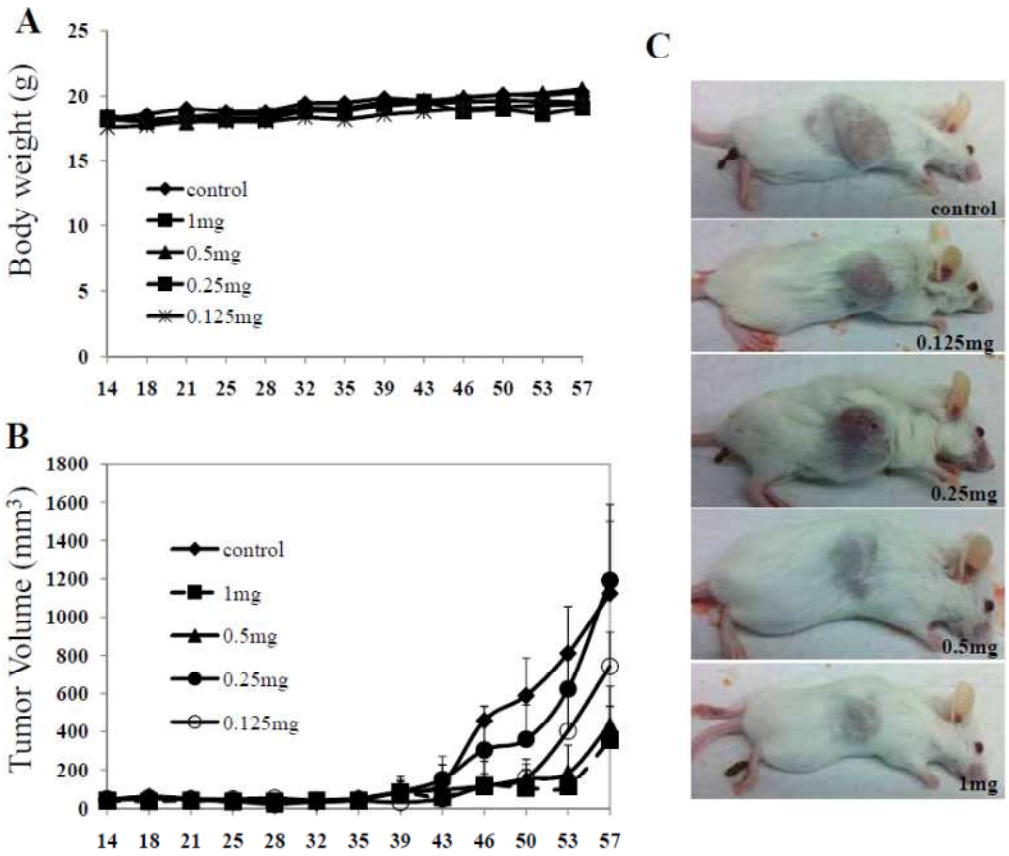


**Figure 7.6.** Dose-dependent tumor-suppressing effects of CPT-loaded FMSNs. 25 shaved SCID mice were subcutaneously transplanted with 1X107 MiaPaca-2 culture cells. 14 days after the inoculation when palpable tumors on all mice reached 2-3 mm in diameter, the mice were divided into 5 groups and the treatments were started. Mice in group 1 (control) received injection of saline solution. Group 2 mice received 1 mg CPT-loaded FMSN per mouse per injection (0.2 mL, 5 mg mL−1, the final concentration of CPT was ≈7.8 μM) (1 mg as shown in figure). Group 3 mice were injected with 0.5 mg CPT-loaded FMSN per mouse per injection (0.2 mL, 2.5 mg mL−1, the final concentration of CPT was ≈3.9 μM) (0.5 mg as shown in figure). Group 4 mice were injected with 0.25 mg CPT-loaded FMSN per mouse per injection (0.2 mL, 1.25 mg mL−1, the final concentration of CPT was ≈1.9 μM) (0.25 mg shown in figure). Group 5 mice were injected with 0.125 mg CPT-loaded FMSN per mouse per injection (0.2 mL, 0.6 mg mL−1, the final concentration of CPT was ≈0.9 μM) (0.125 mg shown in figure). All injections were through intraperitoneal and twice per week. A) Average body weights are shown. B) The average tumor volumes are shown as means ± SD. C) Images of representative SCID mice with subcutaneous tumors at the last day of experiment are shown.

## 7.7. References


1. Liong M, Lu J, Kovochich M, Xia T, Ruehm SG, Nel AE, et al. Multifunctional inorganic nanoparticles for imaging, targeting, and drug delivery. *ACS Nano* **2008**, *2*, 889-896.
2. Hom C, Lu J, Liong M, Luo H, Li Z, Zink JI, et al. Mesoporous silica nanoparticles facilitate delivery of siRNA to shutdown signaling pathways in mammalian cells. *Small* **2010**, *6*, 1185-1190.
3. Zhao Y, Trewyn BG, Slowing, II, Lin VS. Mesoporous silica nanoparticle-based double drug delivery system for glucose-responsive controlled release of insulin and cyclic AMP. *J. Am. Chem. Soc.* **2009**, *131*, 8398-8400.
4. Zhang R, Wu C, Tong L, Tang B, Xu QH. Multifunctional core-shell nanoparticles as highly efficient imaging and photosensitizing agents. *Langmuir* **2009**, *25*, 10153-10158.
5. Vivero-Escoto JL, Slowing, II, Wu CW, Lin VS. Photoinduced intracellular controlled release drug delivery in human cells by gold-capped mesoporous silica nanosphere. *J. Am. Chem. Soc.* **2009**, *131*, 3462-3463.
6. Stromme M, Brohede U, Atluri R, Garcia-Bennett AE. Mesoporous silica-based nanomaterials for drug delivery: evaluation of structural properties associated with release rate. *Wiley Interdiscip. Rev. Nanomed. Nanobiotechnol.* **2009**, *1*, 140-148.

7. Qin F, Zhou Y, Shi J, Zhang Y. A DNA transporter based on mesoporous silica nanospheres mediated with polycation poly(allylamine hydrochloride) coating on mesopore surface. *J. Biomed. Mater. Res. A* **2009**, *90*, 333-338.
8. Hom C, Lu J, Tamanoi F. Silica nanoparticles as a delivery system for nucleic acid-based reagents. *J. Mater. Chem.* **2009**, *19*, 6308-6316.
9. Chen AM, Zhang M, Wei D, Stueber D, Taratula O, Minko T, et al. Co-delivery of doxorubicin and Bcl-2 siRNA by mesoporous silica nanoparticles enhances the efficacy of chemotherapy in multidrug-resistant cancer cells. *Small* **2009**, *5*, 2673-2677.
10. Slowing II, Trewyn BG, Lin VS. Mesoporous silica nanoparticles for intracellular delivery of membrane-impermeable proteins. *J. Am. Chem. Soc.* **2007**, *129*, 8845-8849.
11. Slowing II, Vivero-Escoto JL, Wu CW, Lin VS. Mesoporous silica nanoparticles as controlled release drug delivery and gene transfection carriers. *Adv. Drug. Deliv. Rev.* **2008**, *60*, 1278-1288.
12. Torney F, Trewyn BG, Lin VS, Wang K. Mesoporous silica nanoparticles deliver DNA and chemicals into plants. *Nat. Nanotechnol.* **2007**, *2*, 295-300.
13. Lu J, Liong M, Zink JI, Tamanoi F. Mesoporous silica nanoparticles as a delivery system for hydrophobic anticancer drugs. *Small* **2007**, *3*, 1341-1346.

14. Lu J, Liong M, Li Z, Zink JI, Tamanoi F. Biocompatibility, biodistribution, and drug-delivery efficiency of mesoporous silica nanoparticles for cancer therapy in animals. *Small* **2010**, *6*, 1794-1805.
15. Liu HM, Wu SH, Lu CW, Yao M, Hsiao JK, Hung Y, et al. Mesoporous silica nanoparticles improve magnetic labeling efficiency in human stem cells. *Small* **2008**, *4*, 619-626.
16. Hsiao JK, Tsai CP, Chung TH, Hung Y, Yao M, Liu HM, et al. Mesoporous silica nanoparticles as a delivery system of gadolinium for effective human stem cell tracking. *Small* **2008**, *4*, 1445-1452.
17. Kim J, Kim HS, Lee N, Kim T, Kim H, Yu T, et al. Multifunctional uniform nanoparticles composed of a magnetite nanocrystal core and a mesoporous silica shell for magnetic resonance and fluorescence imaging and for drug delivery. *Angew. Chem. Int. Ed. Engl*. **2008**, *47*, 8438-8441.
18. Taylor KM, Kim JS, Rieter WJ, An H, Lin W. Mesoporous silica nanospheres as highly efficient MRI contrast agents. *J. Am. Chem. Soc*. **2008**, *130*, 2154-2155.
19. He X, Nie H, Wang K, Tan W, Wu X, Zhang P. *In Vivo* Study of Biodistribution and Urinary Excretion of Surface-Modified Silica Nanoparticles. *Anal. Chem.* **2008,** *80,* 9597-9603.

# Chapter 8

## Cell Protection towards Anthrax Lethal Toxins by EGA-Loaded Mesoporous Silica Nanoparticles

## 8.1. Abstract

High-throughput screening allows thousands of compounds to be screened for a specific activity in a relatively short period of time. In the case of phenotypic screens, however, the bulk of the work must be expended on determining exactly how these small molecules alter the phenotype. In the case of the LT-mediated macrophage lysis screen, possible targets include all steps of toxin entry into the cell and cytosolic sensing of the toxin with eventual death. This chapter describes the characterization of the compound called EGA, which was the most protective compound identified in the screen, using biochemical and cell-based experiments. We find that EGA is an inhibitor of LT-mediated toxicity both *in vitro* and in a Fisher rat model of intoxication. The cell experiments described in this chapter were performed by our collaborator, Dr. Eugene Gillespie in the Bradley group at UCLA, and the animal experiments were performed by Diane Thomas from UCSD.

## 8.2. Introduction

Anthrax is a potentially fatal disease of humans and animals caused by infection with the bacterium *Bacillus anthracis*. The disease is still endemic in many parts of the world and has garnered significant attention due to the bioterror attacks of 2001.[1] The lethal toxin (LT) produced by *Bacillus anthracis* appears to contribute to anthrax disease in two distinct phases: 1) an early phase where local toxin production limits the immune response, aiding in the bacterium's establishment of infection & multiplication and, 2) a late phase where high systemic concentrations cause multi-organ damage, vascular leakage and death of the host. Animal models indicate that purified LT can recapitulate

many symptoms of the disease without the need for the organism.[2-7] As such, a central goal of the field has been to determine how LT damages the host on molecular, cellular and systemic levels, and what, if any, defenses the host has to detect LT and limit infection.

EGA is a novel inhibitor of LT-mediated cytotoxicity discovered in a screen of the Chembridge library, a collection of largely uncharacterized "drug-like" compounds. Biochemical evidence of blocks to toxin pore formation and cleavage of toxin target proteins, led to the conclusion that EGA is a novel inhibitor of toxin trafficking. Preliminary experiments indicate that EGA is protective when co-administered with LT in a rat intoxication model.

Observations using light and electron microscopy led to the conclusion that EGA forms crystals in aqueous solution at concentrations above 30 μM. Additionally, the structure of the compound and its predicted logP value suggested it would be very non-polar and hydrophobic. In fact, when we first attempted to administer the drug to rats, we could not achieve the intended therapeutic dose in an aqueous solution. The specific delivery of drugs is a significant pharmaceutical challenge, and several different vehicles for drug transport are being studied. We decided to take advantage of mesoporous silica nanoparticles, which are being studied for delivery of siRNAs, DNAs, and small-molecules (Figure 8.1).[8-13]

In order to further assess the therapeutic feasibility of EGA, we sought to determine its efficacy in a rat model of LT-induced death. Animals ranging from zebrafish to non-human primates have been utilized as models to study the effects of LT.

The Fisher rat intoxication model is unique because LT causes death in these animals in as little as 37 minutes, whereas mice and other animals typically take several days to die.[14] As in human disease, rats display pleural edema and rapid shock, though pulmonary damage may be secondary to onset of shock.[2] In a Sprague Dawley rat infusion model, LT caused blood pressure and heart rate changes, but did not induce cytokines, nitric oxide, histopathological changes, or rapid death.[14] The cause of vascular collapse in rodents is not known, but it appears that standard shock therapies such as 'fluid support' or norepinephrine treatment either exacerbate LT-mediated shock or have no effect, respectively.[14-16] Though the rapid time to death in rats is Nlrp1b dependent, this is a good model to assess *in vivo* efficacy of toxin entry inhibitors since entry processes are likely conserved in all relevant target cells of LT.

## 8.3. Results and Discussion

Phosphonate-treated mesoporous silica nanoparticles (MSN) were incubated in a solution of EGA and then the EGA solution was removed and particles were washed. The amount of drug bound to the particles was determined to be approximately 2.5% weight/weight (Figure 8.2). The efficacy of the EGA-loaded nanoparticles was assessed using the macrophage cytotoxicity assay (Figure 8.3). We observed that EGA-loaded nanoparticles suspended in PBS fully retained LT-inhibitory activity *in vitro* even after being stored on the bench for two months (Figure 8.4). The LT challenge experiment in the Fisher rat was then performed by collaborators, Drs. Diane Thomas and Marianne Manchester. Twenty milligrams of EGA-loaded nanoparticles and LT (40 μg PA + 12 μg LF) in PBS vehicle were co-injected into Fisher rats through the tail vein and animals

were monitored for the next 14 days. The five control animals injected with LT alone died between 57-79 minutes, while the three animals co-injected with LT and EGA-loaded nanoparticles survived for the entire length of the experiment (Figure 8.5).

## 8.4. Conclusions

These preliminary experiments indicate that EGA-loaded nanoparticles may hold therapeutic potential as inhibitors of LT. The next step will be to test EGA in infection models and/or intoxication models in animal models more reminiscent of human anthrax. Another area of future study will be to determine the particles efficacy if they are administered before or after LT, rather than co-injected with LT. Ultimately, it would be informative to see if EGA alone is capable of protecting animals in a B. anthracis spore infection model. EGA may also have therapeutic relevance beyond anthrax toxin inhibition. We have shown that it is an effective inhibitor of several pH-dependent bacterial toxins. Future studies could focus on these and other bacterial toxins, as well as considering a role for EGA in pH-dependent viral entry.

## 8.5. Experimental

*Materials:* All analytical and reagent grade materials were used as purchased: cetyltrimethylammonium bromide (CTAB) [≥98%, Sigma], tetraethyl orthosilicate (TEOS) [98%, Aldrich], 3-(trihydroxysilyl)propyl methylphosphnate, mono sodium salt [42 wt%, solution in water, Aldrich], sodium hydroxide (NaOH) [certified ACS, Fisher], hydrochloric acid (HCl) [certified ACS plus, Fisher], methanol [certified ACS, Fisher].

*General Methods:* The transmission electron microscope (TEM) images of the silica nanoparticles were collected on a CM 120 (Philips Electron Optics, Eindhoven, The Netherlands) instrument in the California NanoSystem Institute (CNSI). Microfilms for TEM imaging were made by placing a drop of the particle suspension in methanol onto a 200-mesh copper TEM grid (Ted Pella, Inc., Redding, CA) and dried at room temperature. Powder X-ray diffraction (XRD) patterns were collected using an X'Pert Pro diffractometer (Philips) equipped with Cu Kα radiation. UV-vis spectra were collected on a Cary 5000 UV-vis-NIP spectrophotometer.

*Synthesis of Phosphonate modified MCM-41 mesoporous silica nanoparticles:* To prepare the 2D-hexagonal MCM-41 mesoporous silica nanoparticles (MCM-41s), CTAB (250 mg, 0.67 mmol) was dissolved in deionized $H_2O$ (120 mL) with a 2M NaOH water solution (0.875 mL). The mixture was stirred and heated to 80 °C when TEOS (1.25 mL, 6 mmol) was slowly added into the solution. 15 minutes later, 3-(trihydroxysilyl)propyl methylphosphnate (325 μL, 1.35 mmol) was added and the TEOS was allowed to hydrolyze for 2 hours and the reaction was cooled down to room temperature. The products were collected by centrifugation and washed by methanol. To remove the templating surfactant molecules from the mesopores, 250 mg of the as-synthesized MCM-41s were suspended in acidic methanol. The mixture was refluxed under nitrogen for 12 hours. The solvent extracted particles were collected by centrifugation, washed by methanol and dried under vacuum.

*Particle loading with the anti-lethal toxin drug:* Solvent extracted particles (250 mg) were suspended in DMSO (5 mL) with 4-bromobenzaldehyde N-(2,6-dimethylphenyl)semicarbazone (50 mg, 0.144 mmol). The particles were stirred at room temperature for 2 days. The loaded particles were collected by centrifugation and dried under vacuum for 2 days. To measure the loading capacity for the drug loaded particles, the loaded particles (6 mg) were suspended and sonicated in DMSO (1 mL). The suspension was then centrifuged and the supernatant was collected for the measurement of the drug concentration using the UV-vis spectroscopy. The amount of drug released from this sample was converted into loading capacity (expressed in weight percent of the sample).

*Bone-marrow derived macrophage LT viability assay with WST-1:* Femur exudates from C57Bl/6 or C57Bl/6Nlrp1b (129S1) transgenic animals were cultured for seven days in DMEM supplemented with 10% fetal bovine serum, 1% penicillin/streptomycin/glutamine (Gibco), 2% 14-22 conditioned media and incubated in a 5% $CO_2$ humidified incubator at 37ºC.

Cells were seeded at $2.0\times10^4$ cells/well in each well of a 96-well plate in DMEM (Cellgro, 10-017CV) the night before the experiment. The next day, media was shaken out and replaced with 30 μL of DMEM supplemented with HEPES (Cellgro, 15-018CV) for intoxication. Compounds were added at 2× concentration in a 50 μL volume of media and cells were incubated for one hour. Then, LF and PA were added to a final concentration of 400 ng/mL for three hours. Media was shaken from plate and a 1:10

dilution of WST-1 viability reagent was added. Cells were incubated for another hour and absorbance at 450 nm was measured using Victor 3V plate reader (Perkin Elmer).

*Fisher Rat LT intoxication:* Fisher Rats were injected with 500 ul i.v. in the tail vein containing 20 mg of the EGA loaded nanoparticles, 40 ug PA, and 12 ug LF in PBS vehicle. Animal survival was monitored overnight and mean time to death was also recorded.

## 8.6. Figures and Tables

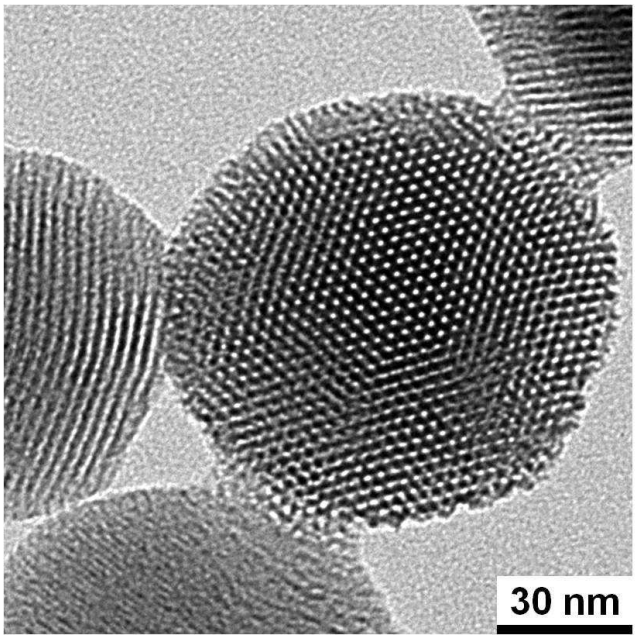


**Figure 8.1.** TEM image of the phosphonate modified MCM-41 particles.

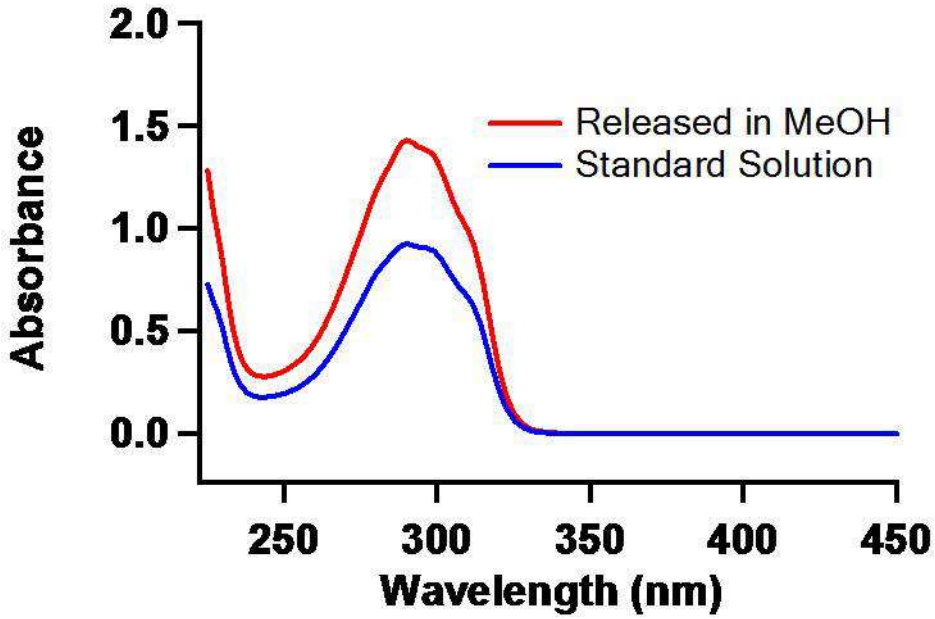


**Figure 8.2.** Loading capacity test of the EGA-loaded particles. The amount of EGA released was measured using UV-vis spectroscopy.

A

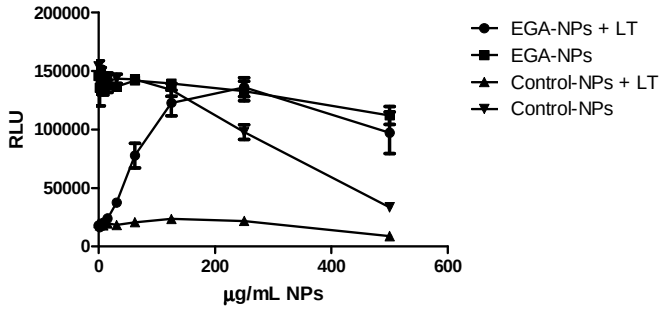


B

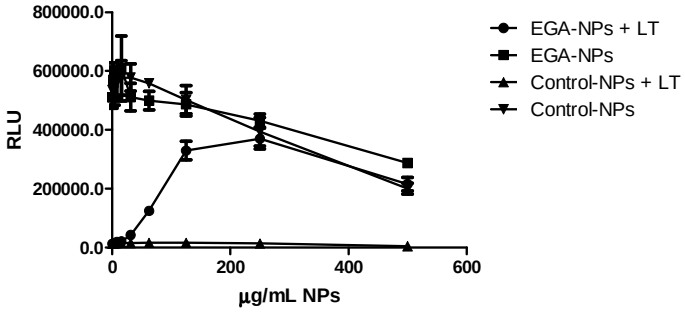


**Figure 8.3.** EGA loaded nanoparticles protect from LT-induced cytotoxicity in 4 (A) or 24 (B) hour assays. (A) RAW264.7 cells were seeded in media at 2.0 x $10^3$ cells/well on each well of a 384-well plate in a 40 µL volume the sixteen hours before the experiment. Mesoporous silica nanoparticles loaded with EGA (EGA-NPs) or unloaded silica nanoparticles (Control-NPs) at 6x concentration were added to wells in a volume of ten µL and cells were incubated for 80 minutes. LT at 6x concentration was added to wells in a volume of ten µL, resulting in a final concentration of 500 ng/mL PA and LF. Cells were then incubated for 4 hrs. The addition of toxin dilutes the NPs to the final concentration indicated on the graph. After 4 hrs, ATPlite was added to assess cell viability (B) RAW264.7 cells were seeded in media at 2.0 x $10^3$ cells/well on each well of a 384-well plate in a 40 µL volume 40 hours before the experiment. Mesoporous silica nanoparticles loaded with EGA (EGA-NPs) or unloaded silica nanoparticles (Control-NPs) at 6x concentration were added to wells in a volume of ten µL and cells were incubated for 90 minutes. LT was added to a final concentration of 500 ng/mL PA and LF and cells were incubated for 24 hrs. The addition of toxin dilutes the NPs to the final concentration indicated on the graph. After 24 hrs, ATPlite was added to assess cell viability.

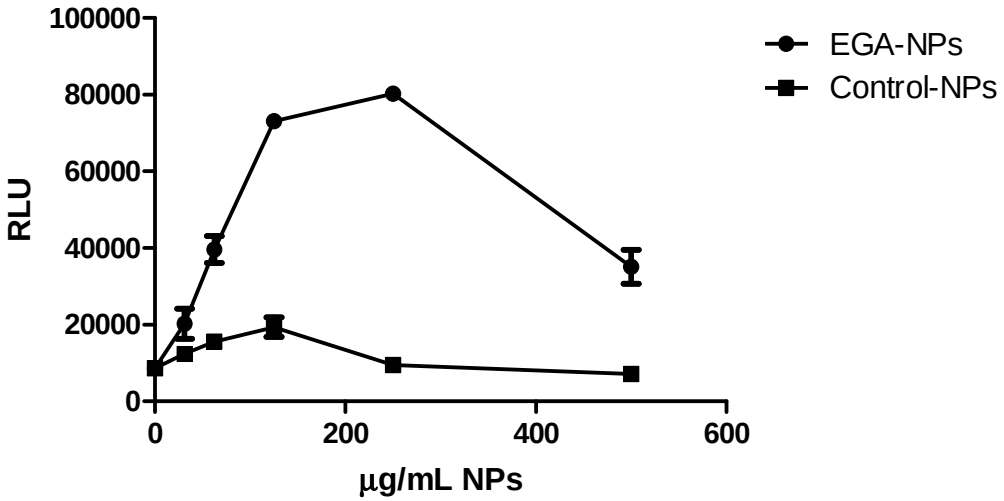


**Figure 8.4.** EGA-NPs protect from LT even after 2 months in solution. RAW264.7 cells were seeded at 2.0 x $10^3$ cells/well on each well of a 384-well plate the night before the experiment. EGA-NPs or Control-NPs were added for 20 minutes followed by addition of LT to a final concentration of 500 ng/mL LF + PA. Cells were incubated for 3 hrs before addition of ATPlite to assess viability.

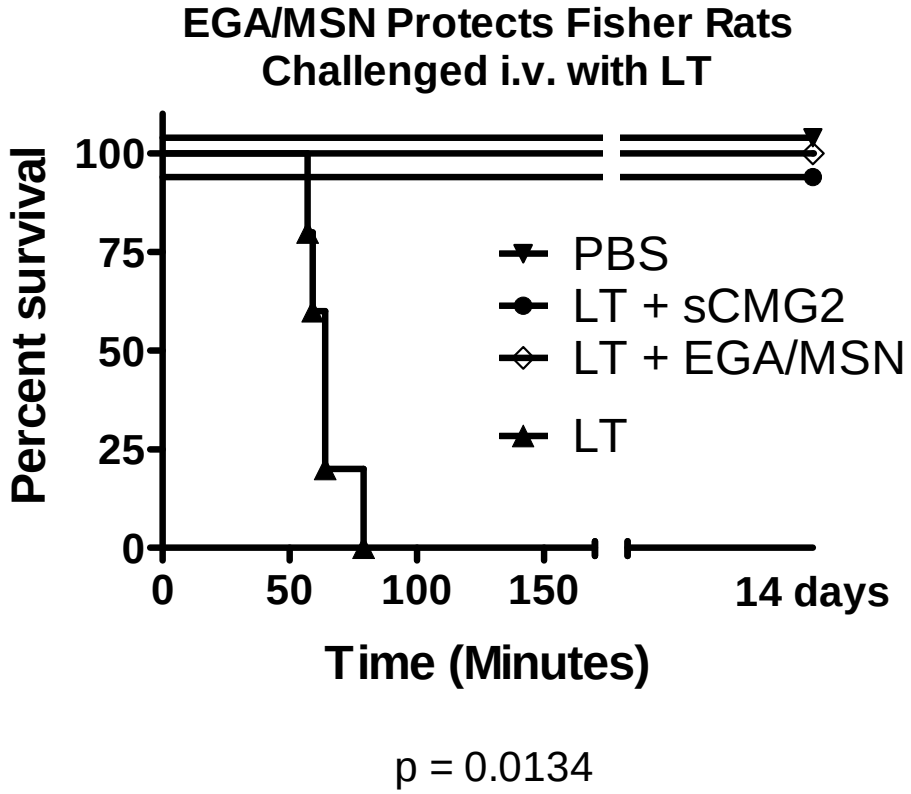


**Figure 8.5.** EGA protects rats from LT-mediated death. Fischer rats were injected with EGA-loaded nanoparticles + LT, soluble anthrax toxin receptor anti-toxin (sCMG2) + LT, LT alone, or PBS vehicle only and mean time to death was measured. The tail vein was injected with 500 ul PBS containing 20 mg of the EGA loaded nanoparticles, 40 ug PA, and 12 ug LF. A 2:1 molar ratio of sCMG: PA was used as a positive control for protection, with the total amount of sCMG2 being $9.64 \times 10^{-10}$ moles. Animal survival was monitored for 14 days and mean time to death was also recorded. Five rats were injected with LT only, five with PBS only, five with LT + sCMG2, and three with LT + EGA/MSN.

## 8.7. References


1. World Health Organization., International Office of Epizootics., and Food and Agriculture Organization of the United Nations. Anthrax in humans and animals, 4th edn (Geneva, Switzerland, World Health Organization), **2008**.
2. Cui, X., Moayeri, M., Li, Y., Li, X., Haley, M., Fitz, Y., Correa-Araujo, R., Banks, S.M., Leppla, S.H., and Eichacker, P.Q. *Am. J. Physiol. Regul. Integr. Comp. Physiol.* **2004**, *286*, R699-709.
3. Culley, N.C., Pinson, D.M., Chakrabarty, A., Mayo, M.S., and Levine, S.M. *Infect. Immun.* **2005**, *73*, 7006-7010.
4. Gozes, Y., Moayeri, M., Wiggins, J.F., and Leppla, S.H. *Infect. Immun*. **2006**, *74*, 1266-1272.
5. Moayeri, M., Haines, D., Young, H.A., and Leppla, S.H. *J. Clin. Invest.* **2003**, *112*, 670-682.
6. Sherer, K., Li, Y., Cui, X., and Eichacker, P.Q. *Am. J. Respir. Crit. Care Med*. **2007**, *175*, 211-221.
7. Proft, T., Microbial toxins: current research and future trends (Norfolk, Caister Academic Press), **2009**.
8. Li, Z., Barnes, J.C., Bosoy, A., Stoddart, J.F. Zink. J.I. *Chem. Soc. Rev*. **2012**, *41*, 2590-2605.
9. Clemens, D.L., Lee, B.Y., Xue, M., Thomas, C.R., Meng, H., Ferris, D.P., Nel, A.E., Zink, J.I., Horwitz, M.A. *Antimicrob. Agents. Chemother*. **2012**, 56(5):2535-2545.

10. Lu, J., Liong, M., Li, Z., Zink, J.I., and Tamanoi, F. *Small* **2010**, *6*, 1794-1805. 138

11. Lu, J., Liong, M., Zink, J.I., and Tamanoi, F. *Small* **2007**, *3*, 1341-1346.

12. Hom, C., Lu, J., Liong, M., Luo, H., Li, Z., Zink, J.I., Tamanoi, F. *Small* **2010**, *6*, 1185-1190.

13. Xia, T., Kovochich, M., Liong, M., Meng, H., Kabehie, S. George, S. Zink, J.I. Nel, A.E. *ACS Nano* **2009**, *3*, 3273-3286.

14. Moayeri, M., and Leppla, S.H. *Mol. Aspects Med*. **2009**, *30*, 439-455.

15. Li, Y., Cui, X., Su, J., Haley, M., Macarthur, H., Sherer, K., Moayeri, M., Leppla, S.H., Fitz, Y., and Eichacker, P.Q. *Crit. Care Med*. **2009**, *37*, 1348-1354.

16. Sherer, K., Li, Y., Cui, X., Li, X., Subramanian, M., Laird, M.W., Moayeri, M., Leppla, S.H., Fitz, Y., Su, J., Eichacker, P.Q., *Crit. Care Med*. **2007**, *35*, 1560-1567.

# Chapter 9

# Conclusions and Future Directions

In this dissertation, the advancements on the mesoporous silica nanoparticles based drug delivery sustems have been demonstrated, including the results of physical chemical studies, the organic functionalizations and biomedical applications of these materials.

In the physical chemical studies, it is demonstrated that mesoporous silica nanoparticles have high surface area and pore capacity, and can hold large amounts of payload within their pore channels. By attaching the acid-responsive nanogate on the particle surface, particles can hold water-soluble cargo molecules without leakage and only release them upon pH activation. The uptake and release capacities have a direct relationship with the specific surface area among different types of particle morphology. Time-resolved and steady-state fluorescence depolarization experiments were used to quantitatively measure the mobility of the dye molecules encapsulated in mesoporous silica nanoparticles, and the results were compared between different solvent and loading conditions. The rigidochromism experiments on fluorescent dye loaded hollow and non-hollow particles demonstrated their different internal environment and different physical states of the encapsulated cargo molecules.

The organic functionalizations of the particles allow the introduction of various designs of nanomachines to the particle surface and the realization of stimuli-responsive release mechanisms. By attaching a cyclodextrin-based nanopiston machine, two different acid-responsive release pathways have been demonstrated. Cargo with sizes smaller than the cyclodextrin cavity can be released at pH 5 following the removal of the

piston molecules. Cargo with sizes larger than the cyclodextrin cavity, on the other hand, can be released at pH 6 following the cleavage of the cyclodextrin cap. These systems have been improved so that the two release mechanisms are combined on one particle, which is loaded with two cargoes of different sizes. This dual-loaded system releases the smaller cargo under acidic pH, and the larger cargo under reducing conditions, therefore demonstrating size selectivity during cargo release. However, this work is only one example of many multifunctional designs enabled by this highly modular system Current efforts in our research group include varying the designs of each building block to obtain targeted drug delivery systems, as well as systems that are responsive to light, enzymes and other internal or external stimuli.

In the biomedical applications of the mesoporous silica nanoparticle based drug delivery systems, it has been demonstrated that theses particles are well tolerated by cells and living animals at their effective dosage. Polyethyleneimne coated particles have been used to deliver small interfering RNA into living cells, and demonstrated good gene silencing effect. The co-delivery of anti-cancer drug and the siRNA that shuts down proteins involved in multiple drug resistance leads to significantly higher therapeutic effecacy. Mesoporous silica nanoparticles loaded with hydrophobic anti-cancer drug have been shown to have strong tumor shrinking effects on animal models. The particles modified with folate targeting groups have significant higher tumor suppressing efficiency on certain cancer types. Particles loaded with anti-microbial agents have also successfully protected animals from anthrax lethal toxin induced death. These are all exciting advancements towards the utilization of mesoporous silica nanoparticle based

drug delivery systems in living organisms. However, further investigations on the biodistribution of these materials are still needed. Designs in nanomachiens, targeting agents and polymer coatings will be improved and integrated to abtain highly selective and on-command delviery systems.